WOOD AND FIBER SCIENCE

The Sustainable Natural Materials Journal

Volume 55, Number 2_2023 *(ISSN 0735-6161)*

EDITORIAL AND PUBLICATION POLICY

Wood and Fiber Science as the official publication of the Society of Wood Science and Technology publishes papers with both professional and technical content. Original papers of professional concern, or based on research of international interest dealing with the science, processing, and manufacture of wood and composite products of wood or wood fiber origin will be considered.

All manuscripts are to be written in US English, the text should be proofread by a native speaker of English prior to submission. Any manuscript submitted must be unpublished work not being offered for publication elsewhere.

Papers will be reviewed by referees selected by the editor and will be published in approximately the order in which the final version is received. Research papers will be judged on the basis of their contribution of original data, rigor of analysis, and interpretations of results; in the case of reviews, on their relevancy and completeness.

As of January 1, 2022, Wood and Fiber Science will be an online only, Open Access journal. There will be no print copies. Color photos/graphics will be offered at no additional cost to authors. The Open Access fee will be $1800/article for SWST members and $2000/article for nonmembers. The previous five years of articles are still copyright protected (accept those that are identified as Open Access) and can be accessed through member subscriptions. Once a previous article has reached its 5th anniversary date since publication, it becomes Open Access.

Technical Notes

Authors are invited to submit Technical Notes to the Journal. A Technical Note is a concise description of a new research finding, development, procedure, or device. The length should be **no more than two printed pages** in WFS, which would be five pages or less of double-spaced text (TNR12) with normal margins on 8.5 x 11 paper, including space for figures and tables. In order to meet the limitation on space, figures and tables should be minimized, as should be the introduction, literature review and references. The Journal will attempt to expedite the review and publication process. As with research papers, Technical Notes must be original and go through a similar double-blind, peer review process.

On-line Access to *Wood and Fiber Science* Back Issues

SWST is providing readers with a means of searching all articles in *Wood and Fiber Science* from 1968 to present Articles from 1968 to 2017 are available to anyone, but in order to see 2017 to 2021 articles you must have an SWST membership or subscription. SWST members and subscribers have full search capability and can download PDF versions of the papers If you do not have a membership or subscription, you will not be able to view the full-text pdf.

Visit the SWST website at http://www.swst.org and go to Wood & Fiber Science Online. Click on either SWST Member Publication access (SWST members) or Subscriber Publication access (Institution Access). All must login with their email and password on the HYPERLINK "http://www.swst.org" www.swst.org site, or use their ip authentication if they have a site license.

As an added benefit to our current subscribers, you can now access the electronic version of every printed article along with exciting enhancements that include:

- IP authentication for institutions (only with site license)
- Enhanced search capabilities
- Email alerting of new issues
- Custom links to your favorite titles

WOOD AND FIBER SCIENCE

There are three classes of membership (electronic only) in the Society: Members – dues $150; Retired Members – dues $75; Student Members – dues $25. We also have membership category for individuals from Emerging Countries where individual members pay $30, individual students pay $10; Emerging Group of 10 pay $290, and Student Groups of 10 pay $90. Institutions and individuals who are not members pay $300 per volume (electronic only). Applications for membership and information about the Society may be obtained from the Executive Director, Society of Wood Science and Technology, P.O. Box 6155, Monona, WI 53716-6155 or found at the website http://www.swst.org.

Site licenses are also available with a charge of:
- $300/yr for single online membership, access by password and email
- $500/yr for institutional subscribers with 2–10 IP addresses
- $750/yr for institutional subscribers with 11–50 IP addresses
- $1000/yr for institutional subscribers with 51–100 IP addresses
- $1500/yr for institution subscribers with 101–200 IP addresses
- $2000/yr for institutions subscribers with over 200 IP addresses.

New subscriptions begin with the first issue of a new volume. All subscriptions are to be ordered through the Executive Director, Society of Wood Science and Technology.

The Executive Director, at the Business Office shown below, should be notified 30 days in advance of a change of email address.

Business Office: Society of Wood Science and Technology, P.O. Box 6155, Monona, WI 53716-6155.
Editorial Office: Jeff Morrell, jmorrell@usc.edu.au

WOOD AND FIBER SCIENCE

JOURNAL OF THE SOCIETY OF WOOD SCIENCE AND TECHNOLOGY

VOLUME 55   NOVEMBER 2023   NUMBER 2

CONTENTS

FIELD EVALUATION OF PHYSICAL BARRIERS AGAINST SUBTERRANEAN TERMITES AND AMBROSIA BEETLES IN A CLT WALL ENVELOPE SYSTEM

K. Neupane*

Graduate Research Assistant
Mississippi State University
Department of Sustainable Bioproducts
Starkville, MS 39759
E-mail: neupane.kamal49@gmail.com

J. D. Tang

Research Forest Products Technologist
USDA Forest Products Laboratory
Starkville, MS 39759
E-mail: juliet.d.tang@usda.gov

H. Lim†

Senior Lecturer
University of Canterbury
School of Forestry
Christchurch, New Zealand
E-mail: thomas.lim@canterbury.ac.nz

J. T. Street

Associate Professor
E-mail: jts118@msstate.edu

Y. Kim

Assistant Professor
Mississippi State University
Department of Sustainable Bioproducts
Starkville, MS 39759
E-mail: ysk13@msstate.edu

E. Gasparri

Senior Lecturer
University of Sydney
School of Architecture, Design and Planning
New South Wales 2006, Australia
E-mail: eugenia.gasparri@sydney.edu.au

(Received July 2023)

Abstract. The effectiveness of physical barriers against subterranean termites was evaluated in a 34-wk field test in coastal Mississippi by installing Obex11, a commercial polyethylene flashing, and Termimesh, a stainless-steel mesh in 3-ply 280 mm (width) × 450 mm (length) cross laminated timber (CLT) walls. Damage showed that both barriers performed significantly better than the no barrier control with respect to termite damage as evaluated by visual rating and mud tube length. Obex11, however, like the no barrier

* Corresponding author
† SWST member

control, was more vulnerable to attack by *Ambrosiodmus minor* (Stebbing), an invasive ambrosia beetle, with both treatments exhibiting significantly longer bore trails than those found in Termimesh.

Keywords: Cross laminated timber, building envelope, termite barrier, invasive beetle, timber durability.

INTRODUCTION

Cross laminated timber (CLT) is an engineered wood product consisting of layers of lumber products perpendicular to each other that are glued using structural adhesives and pressed to form a solid panel. The introduction of the CLT product standard, ANSI/APA PRG 320 (ANSI/APA 2018) in 2011 and its incorporation in the International Building Code (IBC) (International Code Council 2021) and National Design Specification for Wood Construction (American Wood Council 2018) in 2015 has focused people's interest in CLT as an alternative and hybrid material for steel and concrete. As a biodegradable product, CLT is susceptible to subterranean termite attack, especially in warmer regions that have high humidity and dampness. These termites depend on moisture to attack wood and thus, maintain contact with the soil or locate near areas where water collects. Improper detailing and poor building construction design make conditions favorable for termite infestations and should be prevented at any cost (Peterson et al 2006). This problem also currently limits the use of CLT walls to above-ground conditions.

Hybrid construction system using steel and concrete for ground contact and timber for remaining stories have been a common practice in mass timber construction to overcome biodeterioration and moisture problems. CLT manufactured from lumber boards treated with preservatives can be a potential method to be used in ground contact or close to the foundation to protect the buildings from decay and termites. For wood preservation, chromated copper arsenic (CCA) was a commonly used biocide until 2003, when residential sales of CCA-treated wood were discontinued due to the adverse effects of arsenic and chromium on human health and the environment. This led to the introduction of water-based preservatives like micronized copper azole (MCA), which

has low corrosion and leaching rates (Lebow 2004). Research has shown that the mechanical properties of CLT and the bonding performance of adhesives can be degraded due to preservative treatment (Lim et al 2019; Lim et al 2020).

Water-shedding materials like simple paint films, water repellents, urethane coatings, and others can be used to prevent fungal and insect attacks. However, they must be chosen and utilized cautiously as their performance depends on the application and their durability (Wang et al 2018). Such materials can fail over time when the wood gets exposed to leaks and/or external weather conditions and thus, render the wooden members more susceptible to termites and fungal decay. A study to investigate the effectiveness of using polyurea coatings against termites was conducted in Hawaii. Results showed that such coatings provided limited protection against termites, as the coatings degraded over time due to weathering (Konkler et al 2019).

Physical barriers like Termimesh, a commercial product made from stainless steel with fine openings, have been tested in the past and proven to be effective against termites. Grace et al (1996) conducted a 1-yr field test in Hawaii in 1995 using susceptible 250 mm × 85 mm × 18 mm wood specimens in closed bags made out of Termimesh and found that the steel mesh had protected the wood from attack by *Coptotermes formosanus* Shiraki, an introduced species of aggressive subterranean termite. Various stainless-steel mesh tests were conducted in Arizona, FL, Mississippi, and South Carolina in 1993 (Kard 1998). After running the test for 4-5 yr, no termite damage was seen on the 50 mm × 100 mm × 450 mm southern yellow pine (SYP) wood specimens that were fully wrapped with stainless-steel mesh up to 375 mm height and inserted 225 mm deep into termite-infested soil while exposing 75 mm wood at the top. Similarly, in another setup

designed to simulate access created by pipes passing vertically through a concrete slab foundation, no termite attack was seen after 5 yr of exposure (Kard 1998). In this setting, each pine sapwood block was placed inside a PVC pipe (100 mm diameter) that passed through the center of a small concrete slab (50 mm × 500 mm × 500 mm). Thus, the only layers separating the pine sapwood block from the soil was the standard vapor barrier (600 mm × 600 mm) directly under the slab and the stainless-steel mesh (600 mm × 600 mm) placed between the vapor barrier and the soil (Kard 1998).

Plastic physical barriers can prevent termite attacks and have been researched for a long time, but this method seems to work until the membranes start to wear and tear by weathering. Various forms of plastics were studied against termites in the laboratory in Australia (Gay and Wetherly 1969). The research showed that polyvinyl chloride in their rigid or semirigid forms and high-density polyethylene membranes were very resistant to termites but vulnerable when plasticized to use as tape or insulant. Research conducted in Japan using a new laboratory method of testing the termite resistance of plastics showed that nylon polyamides were resistant to termites (Tsunoda et al 2010). While plastic membranes have been seen to be effective against termites in these tests, they can cause moisture to accumulate, which promotes decay and other moisture-related problems. Recently, various forms of self-adhering and nonadhering plastic membranes such as TERM, Pango wrap, and so on are being manufactured to protect wood against moisture and termite attack. However, limited independent field studies have been conducted to investigate their utility and feasibility for mass timber building construction.

A few other studies have been conducted to assess termite damage on CLT, but the prevalent data are limited to small-scale specimens. For example, a laboratory study (Franca et al 2018) using *C. formosanus* collected from Mississippi was conducted on 100 mm × 100 mm × 25 mm (4″ × 4″ × 1″) CLT specimens following modifications from the American Wood Protection Association (AWPA) E-1 standard (AWPA 2020). The modifications related to the size of samples, containers, termite numbers, and duration of the test, all of which were necessary to incorporate the heterogeneous design elements of the CLT into the test sample compared with plain sawn lumber. This 8-wk laboratory study showed that CLT made from spruce-pine-fir exhibited slightly less percent mass loss (6.0%) than untreated SYP sapwood (7.0%) but both products had greater mass loss than that recorded for CCA-treated pine (3.9%) (Franca et al 2018). AWPA E-21 (2015) provides guidelines to conduct a full-size commodity field test that evaluates performance of wood products set on the open ends of concrete blocks against termites for interior applications. Stokes et al (2019) used the E-21 test to expose 3-ply CLT specimens (16″ × 4″) at a coastal Mississippi field site with inspections at 12 and 24 mo. Visual ratings of the CLT showed increasing levels of attack over time by subterranean termites (primarily native *Reticulitermes* species). By 24 mo, termite mud tubes covered the base of the CLT, and attack was severe enough that a putty knife could be manually pushed through the wood. These laboratory and field tests show that CLT is highly susceptible to damage by subterranean termites.

The standard building envelope described in the North American CLT handbook consists of rain screen cladding/siding, insulation, weather-resistant barrier (WRB), and self-adhering flashing from the exterior to the wall's interior (FPInnovations 2010). IBC Section 2304 (International Code Council 2021) and International Residential Code (IRC) Sections R317 and R318 (International Code Council 2021) and recommend, but do not require, the use of multiple protection systems against termites, such as preservative treatment and/or physical barriers. Untreated CLT walls are suited for interior above-ground use but building codes do not have enough field data to incorporate such physical barriers in the wall envelope to ensure protection against termites. Therefore, the goal of this experiment was to conduct a field performance evaluation of two types of physical barriers (plastic membrane and stainless-steel mesh)

against insect attack in a simplified CLT wall envelope system. Only physical barriers, spacers, and sidings were used to represent the CLT building envelope. To accelerate the experiment, the concrete blocks required in the AWPA E-21 were not used, and sill plates used to anchor the CLT walls to the ground were taken off the CLT panels after 18 wk of installation. Because of the large size of the specimens and the short field exposure (34 wk), the length of termite tubes, beetle trails, and number of beetle holes were reported in addition to visual rating scores. The results suggest that the selection of physical barrier and proper installation method can be a solution against insect attack in mass timber construction that places CLT on a foundation near the soil line instead of using insecticide and preservative treatment. In addition, the installation methods developed here, could provide insights on producing CLT panels with built-in physical barriers during the manufacturing process.

<div align="center">

MATERIALS AND METHODS

</div>

Materials

Two lumber stacks, each consisting of 128 pieces of 2430 mm long visually graded No. 2-2 × 6 (38 mm × 140 mm) SYP sapwood lumber, were supplied by Shuqualak Lumber Co. located in Mississippi. A commercial primer solution diluted with 10% water by volume and Loctite PUR-BOND polyurethane adhesive were used to glue the CLT laminate (Loctite 2020). Hardie cement board 1200 mm × 2400 mm × 8 mm (48″ × 96″ × 0.312″) was cut to the final size to fit the CLT panels, ie 280 mm × 450 mm (11″ × 18″), and were used as siding for the envelope. Aluminum C-section spacers of 19 mm × 19 mm × 450 mm (3/4″ web × 3/4″ flange × 18″ length) were used to hold the sidings to the CLT panels using 32 mm screws. A 300 mm wide × 16,750 mm long roll of Obex11 was used as the plastic physical barrier. It is a 0.15 mm thick polyethylene membrane that contains a chemical blend called Termirepel to repel termites and consists of a yellow and black surface. According to the manufacturer's installation guide, the membrane's

yellow surface was exposed to the exterior. A 914 mm wide × 9140 mm long Termimesh roll was used as steel mesh physical barrier in the second treatment group, which consisted of 0.18 mm thick TMA 725 stainless-steel wire mesh. The apertures on this mesh are 0.45 mm × 0.66 mm wide, through which foraging worker termites cannot penetrate. The specimens installed with Obex11 and Termimesh were labeled with the letters P (for plastic) and S (for steel), respectively, followed by the specimen number (eg P1, P2 and S1, S2). The control specimens with no physical barrier were indicated with the letter C, followed by the specimen number.

Cross Laminated Timber Manufacture

The lumber boards were planed twice by 1.6 mm on each flat surface to a final dimension of 31.75 mm × 140 mm (1.25″ × 5.5″) and subjected to the application of primer within 6 h of planing. Primer was applied at a rate of 21.53 g/m^2 (2 gm/ft^2) to the gluing faces of the laminates. After 10 min of primer application, glue was spread to the primed laminates at a rate of 129.17 g/m^2 (12 g/ft^2). The assembled CLT laminates were pressed under 0.75 MPa (110 psi) for 150 min following the adhesive product specifications (Loctite 2020). Three CLT panels (1 per treatment) were made per batch by dividing lumber boards as shown in Fig 1. Laminates with same color indicate that they were obtained from same board resulting in identical CLT specimens across the treatment groups. The surface laminates were assembled such that the sapwood (as opposed to the pith) was exposed on both sides of the panel as shown in Fig 2.

Cubes (25.4 mm × 25.4 mm × 25.4 mm) were cut from each board to calculate the MC and oven-dry specific gravity (SG$_{oven-dry}$) in accordance with ASTM (2016, 2017) standards, respectively. The average MC and SG$_{oven-dry}$ of the lumber were 10.2% and 0.45, respectively. The average MC of the boards used in CLT manufacturing was within the optimum MC range of 12 ± 3% recommended in the CLT handbook (FPInnovations 2010). A total of 30 CLT panels of final size 96 mm × 280 mm × 450 mm were
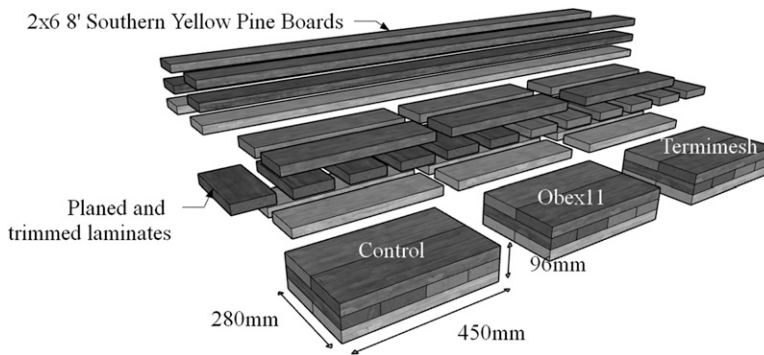
Figure 1.   Lumber layout to manufacture one batch of cross laminated timber (CLT) specimens.

manufactured and stored for a week under indoor ambient conditions before the envelope layers were installed.

Envelope Construction

For the purpose of this study, the only envelope layer added to the CLT panels was a cement board siding, installed via aluminum spacers to create a 19 mm air cavity. Instead of treating the two faces of the CLT panels as exterior and interior side of a building, the siding was installed on both sides. This setup gave an advantage of adding extra surface area to test the termite resistance of physical barriers. Also, this configuration simplified the construction process and negated the extra work of building a different interior wall envelope layer on the inner face of the CLT panel. The other standard building envelope layers were omitted from the experiment as they would provide little or no resistance against termites compared with the chosen physical barriers that are manufactured specifically for termite protection. The 30 CLT panels were divided into three
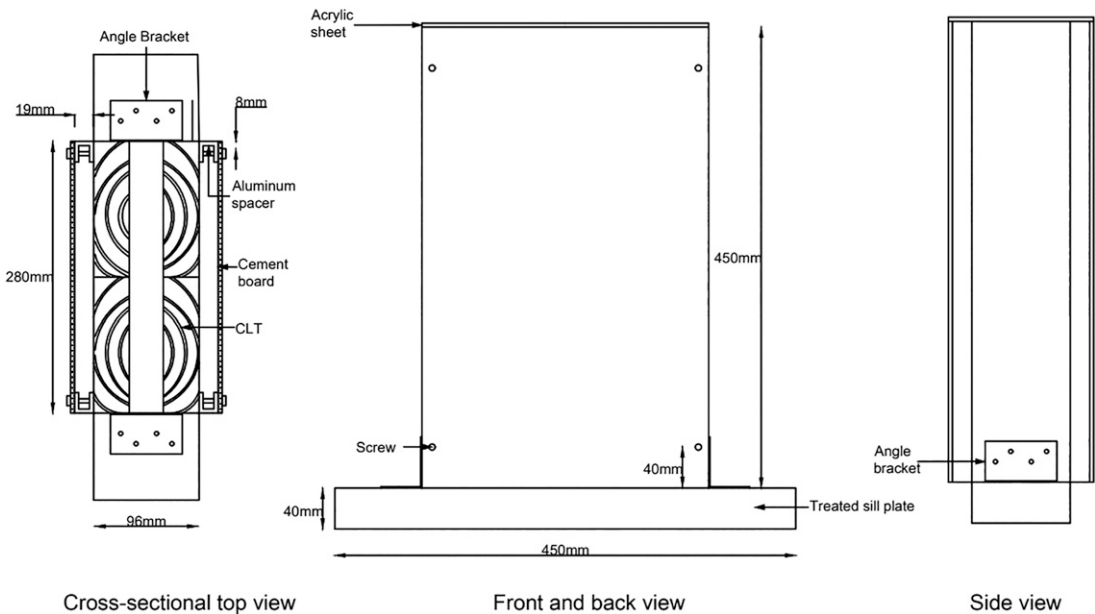
Figure 2.   2D drawing of a CLT envelope specimen.

treatment groups: Obex11, Termimesh, and control (no barrier). The physical barriers were cut to two final sizes: 150 mm × 580 mm (6″ × 23″) and 300 mm × 400 mm (12″ × 16″) for easier wrapping. The 150 mm × 580 mm wide piece was wrapped along the narrow edge of the panel and the 300 mm × 400 mm piece was wrapped along the wider faces of the panel to a height of 150 mm and stapled. The two pieces of barrier overlapped the 95 mm thickness of the CLT at the bottom and 25 mm at the corners where spacers were screwed afterward. This height was chosen based on the Obex11 manufacturer specification of 152-178 mm vertical fold after laying the membrane underneath the sill plates/brick ledger of the wall (Obex11 2023). A self-adhering aluminum tape was used to seal the edges of the CLT, which limited termite exposure only to the faces of the panels. Spacers and sidings were screwed to the CLT panels using two screws per spacer: one on the top and one on the bottom. All the joints between spacers and CLT and spacers and siding were sealed with silicone. The top of the specimen was covered with an acrylic sheet, which was also glued to the panel with silicone for easier inspection from the top without moving the panels. The CLT envelope installation procedure is demonstrated through Fig 3(a)-(d). The control specimens were prepared similarly to the treatment groups except that they did not have any physical barrier. To keep the CLT specimens upright, sill plates made from MCA-treated SYP lumber were entirely wrapped with the self-adhering aluminum tape and fixed to the CLT specimens using angle brackets and screws.

Field Installation and Damage Evaluations

A timeline of field activities is depicted in Table 1. The finished CLT envelope specimens were anchored to the ground using edge metal stakes and deployed at the USDA Forest Service Harrison Experimental Forest, Saucier, MS, near the Gulf Coast, where risk hazard for subterranean termite infestation is typically severe (Peterson et al 2006). The CLT specimens ($n = 10$ per treatment) were laid out in a randomized complete block (RCB) design as shown in Fig 4. Surface investigations were carried out during each inspection to look for damage to physical barriers and the presence of mud tubes. Specimens were also overturned to evaluate termite activities at the soil level. As there was no evidence of termites or mud tubes on specimens at 18 wk, sill plates were removed, and specimens were reinstalled in their original positions. For the final inspection at 34 wk, specimens were taken back to the laboratory, and envelope layers were carefully dismantled. Physical barriers were visually examined for wear and tear, and the CLT was evaluated for attack from subterranean termites and wood-boring beetles.

For termites, final evaluations included number of live termites observed and a wood damage visual
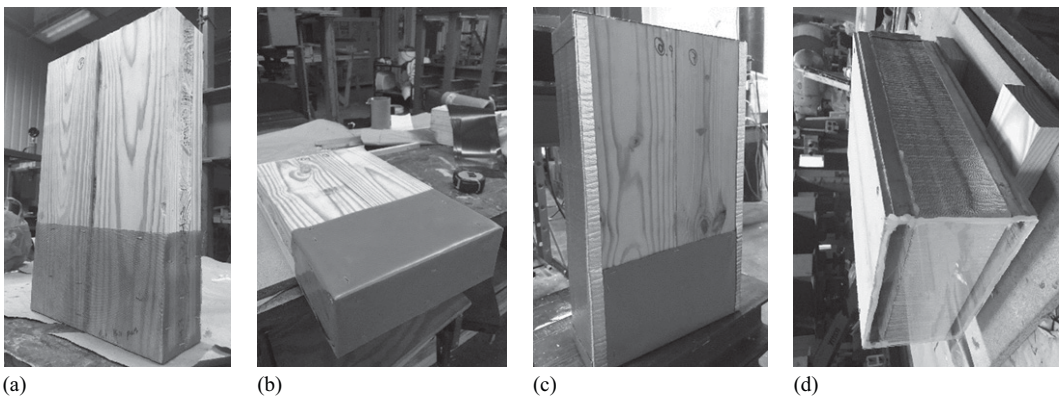
Figure 3.   Envelope installation (a) CLT with Termimesh barrier, (b) CLT with Obex11 barrier, (c) CLT edges sealed with aluminum tape, and (d) a complete CLT envelope specimen with spacers and cement board cladding.

Table 1. Timeline of field activities.

Events	Date	Week	Activities	Observations
Installation	04/01/2021	0	1. Randomized complete block (RCB) design 2. Specimens anchored to the ground using metal stakes	None
First inspection	07/02/2021	12	1. Specimens overturned 2. Surface inspection around the corners and bottom	Termites present underneath the sill plates
Second inspection	08/16/2021	18	1. Inspection 2. Sill plated removed 3. Specimens reinstalled at original position	No termite damage on panels; termites active underneath specimens
Third inspection	10/15/2021	26	1. MC of control specimens measured using pin-type moisture meter 2. The top acrylic cover removed	Termite tubes, patches of termite damage, and moisture damage seen in specimens
Final inspection	12/09/2021	34	1. Samples dismantled for visual rating assessment 2. Live termites and beetles counted and collected for identification	Termite damage on control panels and one steel mesh panel; beetle damage on all groups; Obex11 punctured by beetles

rating ($VR_{termite}$) based on the grading system outlined in the AWPA E21 full-size commodity test for interior use applications given in Table 2 (AWPA 2015). Specifically, each panel was rated on both vertical faces, then averaged to give one visual rating for the replicate. In addition, the length of mud tubes on both vertical faces sides was recorded, then summed to give one mud tube length ($MTH_{termite}$) per panel replicate. For wood-boring beetles, the number of holes observed

Figure 4.   Field installation of CLT specimens in an RCB design (3 × 10 rectangular array with 1200 mm spacing between specimens and rows) at the test site in Saucier, MS.

Table 2. Visual ratings of termite damage according to AWPA E21 (AWPA 2015).

Rating	Description
10	Sound
9.5	Trace, surface nibbles permitted
9	Slight attack, up to 3% of the cross-sectional area affected.
8	Moderate attack, 3-10% of the cross-sectional area affected.
7	Moderate/severe attack and penetration, 10-30% of the cross-sectional area affected.
6	Severe attack, 30-50% of the cross-sectional area affected.
4	Very severe attack, 50-75% of the cross-sectional area affected.
0	Failure

from both vertical faces and the base was recorded then summed to give one value (NH_{beetle}) per panel replicate. BB_{beetle} and AB_{beetle} were the number of holes below and above barrier (or 150 mm for controls), respectively. The length of visible bored trails was also recorded and summed to give one value (BTL_{beetle}) per panel replicate. Termite soldiers and adult beetles were collected and preserved in 70% ethanol for taxonomic identification. Termite soldiers were identified to genus using a key (Scheffrahn and Su 1994), whereas adult beetles were identified to species by Terence Schiefer, Curator of the Mississippi Entomological Museum at Mississippi State University.

Nonparametric Statistical Analysis

The effect of treatment on measured responses ($VR_{termite}$, $MTH_{termite}$, NH_{beetle}, BTL_{beetle}, BB_{beetle}, and AB_{beetle}) were analyzed in SAS 9.4 (SAS Institute 2013) using the Kruskal–Wallis test of Wilcoxon scores (rank sums). Once the Kruskal–Wallis test showed a significant difference in mean ranks among the three groups, a pairwise, two-sided, and multiple comparison test was conducted using Dwass, Steel, Critchlow–Fligner method at a significance level of $p < 0.05$.

RESULTS AND DISCUSSION

A first inspection at 12 wk showed some termite activity on 14 specimens. The termites had not yet attacked the wood even in the case of control panels. The aluminum flashing, which wrapped the sill plate, was preventing moisture movement between soil and wood and appeared to deter termites due to heat build-up from the summer sun. Since this was intended to be a short-term field test, the sill plates were removed at 18 wk. Mud tubes were seen during the third inspection at 26 wk. A few of the top acrylic sheet covers were cracked and came off during the inspection, so all acrylic sheets were removed. Five of the control specimens were attacked by termites, and mud tubes were seen on panel surfaces. Specimens with Obex11 did not show any signs of termite damage, whereas in one of the specimens installed with Termimesh, one mud tube was seen that traveled from the soil level up the full height of the barrier and onto the upper wood face of the CLT specimen. A pin-type moisture meter was used to measure the MC of the control specimen panels, which was 16% and 28% at the top and the bottom, respectively (Table 3). Thus, even though subterranean termites in laboratory studies prefer wood with high MC greater than 79% (Nakayama et al 2005; Gautam and Henderson 2011) and cannot sustain feeding on wood with less than 24% MC, attack and conspicuous damage in the field are possible as long as the wood is close to FSP (about 23% for SYP).

Termite Damage

The two soldiers collected were identified (Scheffrahn and Su 1994) as *Reticulitermes* species and were most likely either *R. flavipes* or *R. virginicus*, both of which occur in abundance at the test site. At test termination (34 wk), only the control specimens had active live termites with up to 10 termites in a specimen and an average of two termites per panel. The average $VR_{termite}$ of the control, Obex11, and Termimesh groups were: 8.9, 10,

Table 3. Percent MC at top and bottom surfaces of control specimens at 26 wk.

Specimen	C1	C2	C3	C4	C5	C6	C7	C8	C9	C10	Average MC (%)
MC at top (%)	14	15	17	19	16	14	17	14	18	16	**16**
MC at bottom (%)	26	25	26	28	29	29	28	27	30	28	**28**

and 9.9, respectively, with Obex11 and Termimesh showing significantly less damage than the control (Fig 5[a]). All control specimens except one showed signs of termite damage indicating greater susceptibility of CLT panels without physical barriers to termite infestation. Summing mud tube length provided another measure of the differences in termite activity among the three treatments. The average $MTH_{termite}$ of the control, Obex11, and Termimesh groups were: 24.5, 0.5, and 5.5 cm, respectively (Fig 5[b]). This suggests that there was little to no termite activity on the Obex11 compared with the Termimesh treatment, and the greatest termite activity on the controls. Statistical analysis, however, only detected significantly lower $MTH_{termite}$ in the control group with no significant difference between Obex11 and Termimesh treatments. Since nonparametric statistics tends to have lower sensitivity, it is possible that differences between the Obex11 and Termimesh may have been resolved with more replication and longer field exposure.

Figure 6(a) shows typical termite damage seen on the CLT from the control treatment. After scraping away the mud tubes (traces of the mud tube outline remain in the photo), the wood damage was revealed and began at the bottom of the CLT near the soil line and progressed upward with channels eaten through the sapwood. Damage was quite conspicuous in almost all of the control specimens but because of the large size of the panels, the assigned visual rating values were always less than 10% of surface area affected.

Figure 6(b) shows one Termimesh specimen that was found with a mud tube that ran from the soil line all the way to the top of the CLT panel, a distance of 55 cm. This was atypical since no mud tubes were found on any of the other Termimesh specimens. Therefore, even though termites could not penetrate Termimesh, they were capable of finding their way to the wood—in this case, by climbing 150 mm across the barrier upwards to the unprotected wood. The wooden specimens tested in Hawaii showed that the termites were able to make their way to the wood through a gap created by a fold in the corner of a wooden specimen wrapped with Termimesh (Grace et al 1996). However, the termite attack was due to an
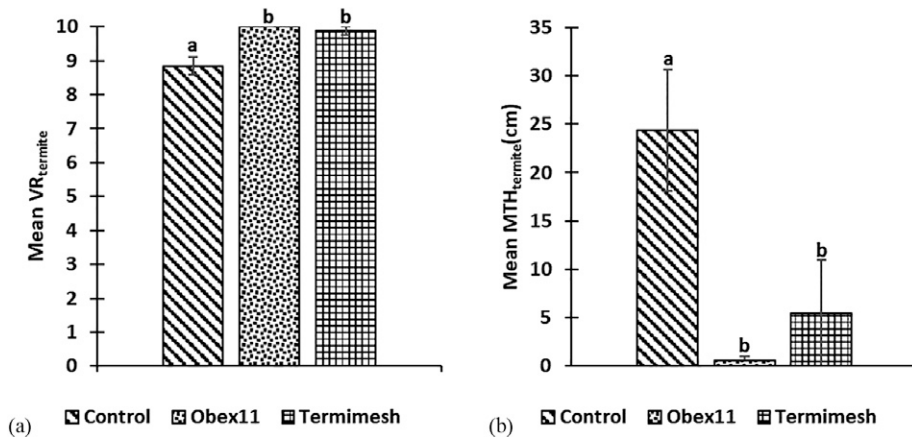

Figure 5.   Mean termite (a) VR and (b) MTH. Different lowercase letters within a plot indicate significant differences among treatments. Bars denote ± SE.
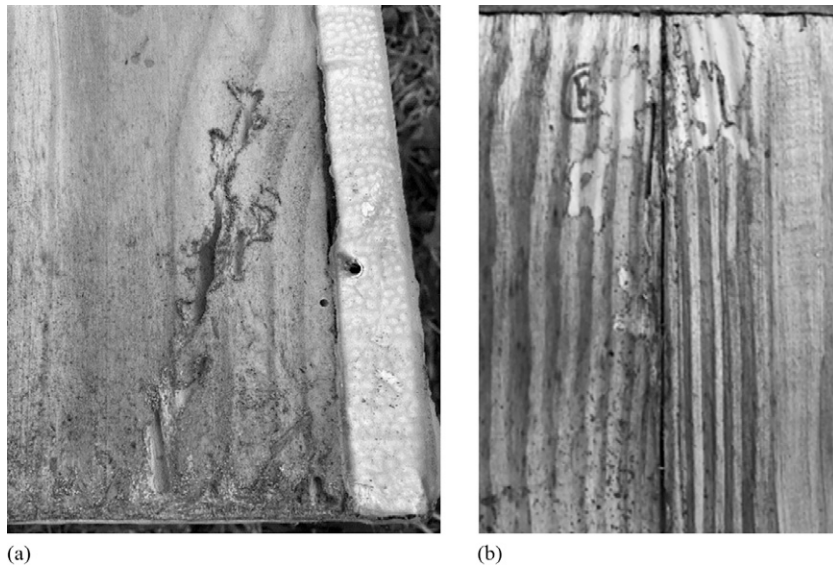
Figure 6.   Damage (a) from a typical control specimen and (b) in one Termimesh specimen, where termites had constructed a mud tube from the soil line up to the top of the panel and attacked the wood at the top of the CLT.

installation error and not related to the barrier's height. A better comparison in terms of barrier height is a 5-yr field test deployed in Arizona, FL, Mississippi, and South Carolina within the United States by Kard (1998). Kard (1998) used 450 mm long wooden stakes wrapped with stainless-steel barrier to a height of 150 mm above ground and found no termite damage, as assessed by percentage attack on wooden blocks, at any of their field sites. One possible explanation for the difference between our Termimesh results with that of Kard's (1998) could be the presence of the outer wall envelope in our study. The wall envelope created a closed dark space (air cavity) with increased dampness, thereby protecting the termites from the sun and desiccation while they constructed their mud tubes and consumed the underlying wood. Regardless of test method, proper installation of the stainless-steel mesh barrier is essential when designing building envelope layers. In addition, the barrier height needs to be further researched as 150 mm did not guarantee termite resistance in all Termimesh specimens when the CLT was in contact with the soil.

As mentioned in Cross Laminated Timber Manufacture section, the bottom edge of both Obex11

and Termimesh panels were wrapped with the barriers and then sealed with aluminum flashing. Even though termites were present under the panels, no termite damage or mud tubes were seen on any of the specimens in the Obex11 group. It appeared that the blend of essential oils and plastic sheeting of the Obex11 prevented the termites from climbing across or puncturing the barrier. In previous lab studies, it was seen that termites were not able to chew through amorphous polyamide plastic material, such as pipes and bars, but were able to deteriorate the low-density polyethylene plastic sheets. However, it should be noted that these tubes and bars were thicker and harder (1 and 6 mm) (Tsunoda et al 2010) compared with Obex11, which resisted termites despite its small thickness (0.16 mm).

Furthermore, the use of insecticides in plastic membranes was found to be effective against termites in previous research (Gay and Wetherly 1969). Recently, weather resistive barriers like Pango wrap that offers termite protection through the integration of copper compounds are also available commercially in the United States. But there remain uncertainties about their in-use serviceability as not enough field studies are

reported. The same holds true for Obex11 even though the presence of essential oils were able to keep the termites away from the CLT despite their exposure to the weather of coastal Mississippi. Termite repelling membranes similar to Obex11, can be a more ecofriendly solution against termites compared with soil insecticides and membranes that use toxic chemicals. The essential oils present in Obex11 are plant-based, which further lowers the use and manufacture of toxic chemicals, contributing to sustainable construction. Since this field test was only 34-wk long, the durability and serviceability of Obex11 for more prolonged exposure times still needs further research. Nevertheless, the use of physical barriers blended with essential oils/nonpoisonous chemicals seems to be a promising solution against termites compared with the use of paints, water-repellants, films, or coatings of polyurea, which can deteriorate over time (Konkler et al 2019).

Beetle Damage

An unanticipated phenomenon in this field test was the presence of ambrosia beetles in the CLT specimens and their ability to chew through the Obex11 membrane. Even though the chemicals and plastic membrane of the Obex11 successfully repelled termites and kept them off the exposed faces of CLT, the Obex11 failed to deter these wood-boring beetles. The three collected adult beetles were identified as *Ambrosiodmus minor* (Stebbing). These beetles have heavily sclerotized mouthparts that chewed through both the membrane and wood to create round-shaped entry holes that led to bored trails within the wood (Fig 7[a]) or sandwiched between the wood and the panel base, which was wrapped first with the membrane and an outer band of aluminum flashing (Fig 6[b]). Sawdust from bored trails was also often observed accumulating between the membrane and the wood near the soil line (Fig 7[a]). In addition, a few CLT specimens in the Obex11 group showed delamination (Fig 7[b]) due to swelling from moisture trapped by the membrane. This moisture accumulated due to rainfall and higher humidity inside the air cavity.

Averages of NH_{beetle} were 1.9, 1.7, and 0.8 for control, Obex11, and Termimesh with no significant difference among totals for treatment groups (Fig 8[a]), although a difference was apparent when hole position was taken into account.

(a)   (b)
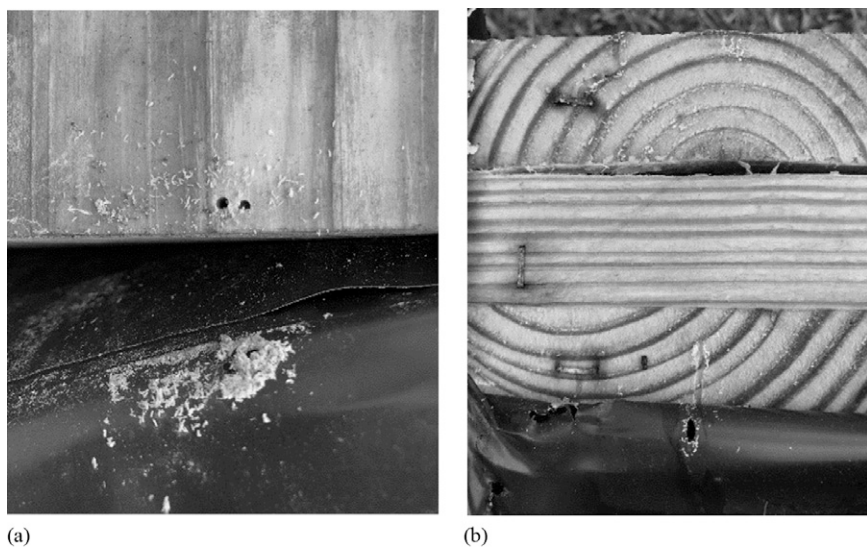
Figure 7.   Damage seen in a typical Obex11 specimen showing (a) two beetle puncture holes through the membrane (accumulating sawdust below) and into the face of the CLT near the soil line, and (b) one beetle puncture through the membrane, a bored trail along the CLT base, and laminate separation caused by swelling from trapped moisture.
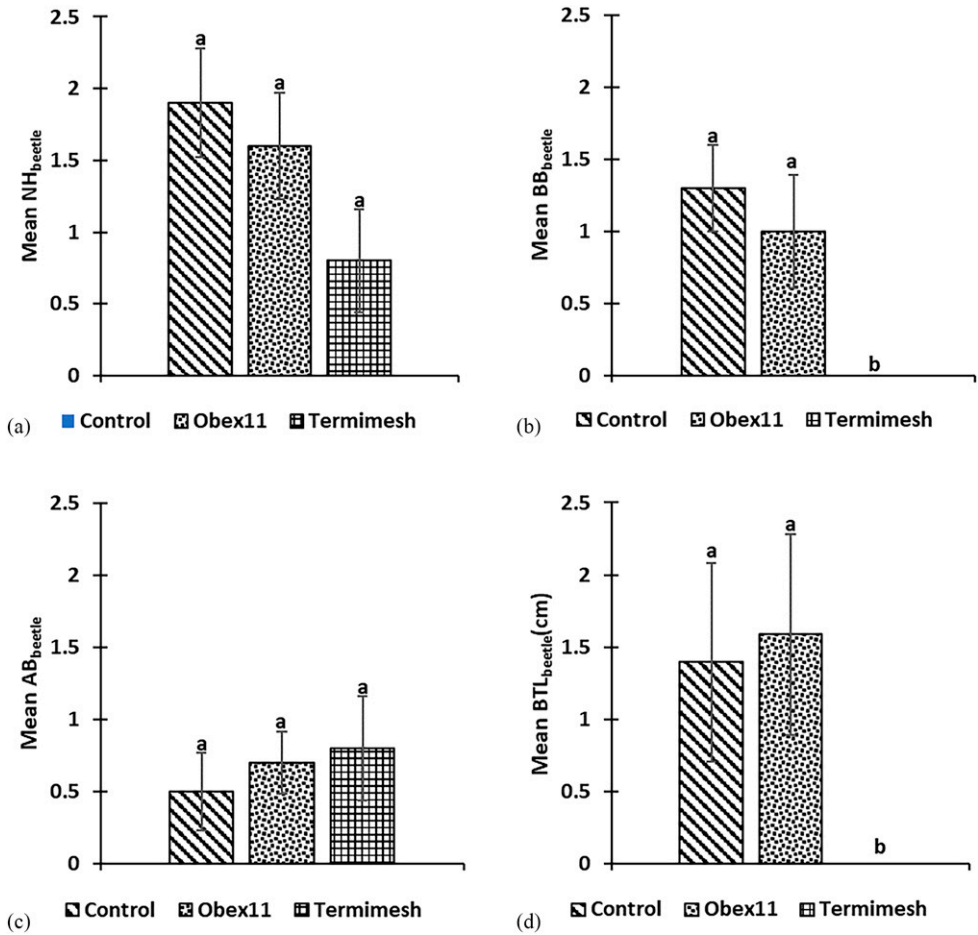
Figure 8. Mean beetle (a) NH (b) BB (c) AB and (d) BTL. Different lowercase letters within a plot indicate significant differences among treatments. Bars represent ± SE.

Control and Obex11 groups had significantly higher BB_{beetle} averages (1.3 and 1.0 holes, respectively) near the bottom edge or below the barrier height compared with 0 holes for Termimesh (Fig 8[b]). Number of holes above the barrier height (AB_{beetle}), however, was not significantly different among the three treatments (0.5, 0.7, and 0.8 for control, Obex11, and Termimesh, respectively) (Fig 8[c]). Thus, these wood-boring beetles could not chew through or otherwise penetrate the Termimesh wherever it covered the wood, but neither Termimesh nor Obex11 protected the wood above the barrier. Nearly all beetle holes were no more than 75 mm above the barrier, suggesting that there is a requisite

minimum wood MC for attack by *A. minor,* as there is for subterranean termites and decay fungi (Nakayama et al 2005; Wang et al 2018). The significant difference in beetle hole positions below the barrier also explains the differences in bore trail length, which were only visible at the base of the CLT panels. The averages of BTL_{beetle} were 1.4, 1.6, and 0 cm for control, Obex 11, and Termimesh, respectively, with Termimesh significantly less than either control or Obex11 (Fig 8[d]).

Research has shown that certain species of beetles (eg Japanese beetles) are attracted by essential oils, such as citronella oil, camphor oil, coffee,

and grapefruit oil (Youssef et al 2009). Manuka, phoebe, and cubeb oil lures have been used to attract redbay ambrosia beetles (Kendra et al 2018). We speculate that one or more of the nine essential oils (cedar oil, cinnamon oil, citronella oil, eugenol, geraniol, lemon grass oil, geranium oil, mint oil, and peppermint oil, each at 0.01%) present in the Obex11 acted as a beetle attractant. Field tests with baited sticky traps containing the essential oils present in Obex11 could be an interesting future research project to identify specific beetle attractant(s). The bright yellow color of the Obex11 may have also served as a visual cue, but since it was covered by the wall envelope, it seems unlikely that color was involved. Further research will need to be done to ascertain the correlation between Obex11 and beetle activity.

Ambrosia beetles are an invasive species that were first detected in 2011 in Florida and have been slowly expanding their range from the Atlantic coast of northeastern Florida to the Gulf coast of Mississippi (Schiefer 2018). In this study, beetles were detected using Lindgren funnel traps hung on bald cypress that used 50/50 mixture of 70% ethanol and ethylene glycol as attractant (Schiefer 2018). Our experiment, on the other hand, demonstrates that the beetles have become established enough in the area to appreciably infest closed CLT walls made up of SYP lumber that was in contact with the soil and had increased MC. Another serious concern, aside from the bore hole and trail damage to the wood, is that *A. minor* carries a white-rot fungus, *Flavodon subulatus,* which it introduces into the wood it infests. This beetle-associated, white-rot fungus is aggressive and has been shown to cause significant weight loss of wood at rates faster than that of other naturally occurring wood decay fungi (Kasson et al 2016). This was further complicated by the fact that Obex11, being a plastic membrane, was holding moisture and causing swelling-induced delamination of the CLT laminates. Both factors would favor invasion and growth of decay fungi capable of compromising the mechanical strength of the CLT panels (Neupane 2021). In addition, the beetle-chewed holes in the plastic membrane barrier are large

enough to compromise membrane integrity by providing entry points for termites to access to the underlying wood. Thus, the conditions that can prevent a multifront attack by beetle, fungi, and termite on CLT certainly warrants future investigation, especially in coastal regions of southeastern United States, where *A. minor* and *Reticulitermes* species overlap range and where fungal decay hazards are high.

CONCLUSIONS

The effectiveness of using Obex11 and Termimesh as barriers for subterranean termites (*Reticulitermes* spp.) were evaluated in a short-term (34 wk) field test in coastal Mississippi, where environmental moisture was allowed to penetrate CLT panels faced with a simple wall envelope system. Barriers were wrapped around the base of the CLT and extended 150 mm up the CLT faces. Like most wall envelope systems, a thin air cavity separated the wall envelope from the CLT. In this study, the use of such a cavity seems to promote insect activity by creating a favorable shaded humid space in CLT proximity. Because of the large size of the CLT and proportionately less overall damage, visual ratings along with termite counts and mud tube lengths were measured to compare treatment groups. An unexpected result was damage caused by an invasive wood-boring ambrosia beetle (*A. minor*), which has been expanding its range in southeast USA. Beetle attack was evaluated by number of bored holes, hole position, and trail lengths.

Data showed that Obex 11 protected the CLT against termite damage in all 10 panels but failed to protect the panels against attack by wood-boring beetles (*A. minor*). It is possible that one or more of the essential oils used as termite repellents acted as a beetle attractant. Although termite damage had not yet occurred in the Obex11 treatment, the beetle-chewed holes clearly compromised the integrity of the membrane and were large enough to give termites and other organisms access to the underlying wood. Moreover, other researchers have found that *A. minor* inoculates wood with an aggressive white-rot decay fungus

(*F. subulatus*), which under favorable conditions of temperature and moisture, would cause more structural damage to the wood than the beetle itself. The Obex11 treatment also trapped enough moisture to cause CLT delamination. Separation of the laminates reduces mechanical strength properties of engineered mass timber and provides more entry points for wood destroying organisms.

Data for Termimesh showed protection in 9 out of 10 replicates, but in the 10th replicate, termites were able to circumvent the barrier by constructing a long mud tube that crossed above the 150 mm high barrier and continued to the top of the panel (450 mm from the soil line), where damage was found. In addition, beetle damage never occurred where the Termimesh actually covered the wood. Neither termite nor beetle could physically chew or otherwise penetrate the stainless-steel mesh due to its hardness and restrictive mesh size. However, a 150 mm barrier height was not adequate to provide 100% protection above the barrier against either termite or beetle as long as wood moisture was conducive to insect attack.

This field test of physical barriers has shown that it is possible to protect CLT walls from termites if suitable material and installation method are chosen. However, further in situ research is needed to ensure that compound(s) that are successful at repelling one wood attacking species do not in fact attract another. Durability, moisture, and barrier height are some of the areas that can be further researched to investigate the effectiveness of using physical barriers in a CLT wall envelope system. Barriers that are flexible, permeable, self-adhering, and have insect repellency can be an effective solution against wood-degrading pests. These findings can further lead researchers and CLT manufacturers to seek innovations on integrating physical barriers to CLT panels during the manufacturing process, thus reducing the installation complications and cost during mass timber buildings construction.

ACKNOWLEDGMENTS

REFERENCES

American Wood Council (2018) National design specification for wood construction. American National Standards Institute/American Wood Council (ANSI/AWC), Leesburg, VA.

ANSI/APA (2018) Standard for performance-rated cross laminated timber. ANSI/APA PRG 320, Tacoma, Washington, D.C.

ASTM (2016) D 4442-16. Standard test methods for direct moisture content measurement of wood and wood-based materials. American Society for Testing and Materials, West Conshohocken, PA.

ASTM (2017) D 2395-17. Standard test methods for density and specific gravity (Relative Density) of wood and wood-based materials. American Society for Testing and Materials, West Conshohocken, PA.

AWPA (2015) E-21. Standard field test for evaluation of wood preservatives to be used for interior applications (UC1 and UC2); Full-size commodity termite test. American Wood Protection Association, Birmingham, AL.

AWPA (2020) E-1. Laboratory methods for evaluating the termite resistance of wood-based materials: Choice and no-choice tests. American Wood Protection Association, Birmingham, AL.

FPInnovations (2010) Cross laminated timber handbook. FPInnovations, Canada.

Franca TSFA, Stokes EC, Tang JD (2018) Durability of cross laminated timber against termite damage. *in* 61st International Convention of Society of Wood Science and Technology and Japan Wood Research Society, November 5-9, 2018, Nagoya, Japan.

Gautam BK, Henderson G (2011) Wood consumption by Formosan subterranean termites (Isoptera: Rhinotermitidae) as affected by wood moisture content and temperature. Ecol Popul Biol 104:459-464.

Gay FJ, Wetherly AH (1969) Laboratory studies of termite resistance V. The termite resistance of plastics. Commonwealth Scientific and Industrial Research Organization, Australia.

Grace J, Yates J, Tome C, Oshira R (1996) Termite-resistant construction: Use of a stainless steel mesh to exclude *Coptotermes formosanus* (Isoptera: Rhinotermitidae). Sociobiology 28:365-372.

International Code Council (2021) International building code. International Code Council, Falls Church, VA.

International Code Council (2021) International residential code. International Code Council, Falls Church, VA.

Kard BM (1998) Termite control: Results of testing at the U.S. forest service. Pest management '98, Opryland Hotel Convention Center, Nashville, TN.

Kasson MT, Wickert K, Stauder C, Short D (2016) Mutualism with aggressive wood-degrading *Flavodon ambrosius* (Polyporales) facilitates niche expansion and communal social structure in *Ambrosiophilus ambrosia* beetles. Fungal Ecol 23:86-96.

Kendra PE, Montgomery WS, Niogret J, Tabanca N, Owens D, Epsky ND (2018) Utility of essential oils for development of host-based lures for *Xyleborus glabratus* (Coleoptera: Curculionidae: Scolytinae), vector of laurel wilt: Essential oil lures for *Xyleborus glabratus*. Open Chem 16:393-400.

Konkler MJ, Cappellazzi J, Morrell JJ (2019) Performance of polyurea-coated Douglas-fir timbers exposed in Hilo Hawaii. Int Wood Prod J 10:31-36.

Lebow ST (2004) Alternatives to chromated copper arsenate for residential construction. U.S. Department of Agriculture, Forest Service, Forest Products Laboratory 9, Res. Pap. FPL-RP-618, Madison, WI.

Lim H, Tripathi S, Li M (2020) Rolling shear modulus and strength of cross-laminated timber treated with micronized copper azole type C (MCA-C). Construction and Building Materials 232:117208.

Lim H, Tripathi S, Tang JD. (2019) Bonding performance of adhesive systems for cross-laminated timber treated with micronized copper azole type C (MCA-C). Construction and Building Materials 259:120419.

Loctite (2020) TDS Loctite HB X602 Purbond. Henkel Cooperation, Bridgewater, NJ.

Nakayama T, Yoshimura T, Imamura Y (2005) Feeding activities of *Coptotermes formosanus* Shiraki and *Reticulitermes speratus* (Kolbe) as affected by moisture content of wood. J Wood Sci 51:60-65.

Neupane K (2021) Field durability test of CLT wall envelope using physical barriers against termites and structural performance of nailed hold-down brackets connected to fungus-exposed CLT walls. Thesis and Dissertations, Mississippi State University, Starkville, MS. https://scholarsjunction.msstate.edu/td/5346.

Obex11. (2023) Lightening underlayment, LLC. https://www.obex11.com/collections/standard-6-mill/products/brick-ledge-roll (16 February 2022).

Peterson C, Wagner TL, Mulrooney JE, Shelton TG (2006) Subterranean termites—Their prevention and control in buildings. Page 38 *in* Home and garden bulletin, Vol. 64, U.S. Department of Agriculture, Forest Service, Washington, D.C.

SAS Institute (2013) SAS software, version 9.4. The SAS Institute, Inc., Cary, NC.

Scheffrahn RH, Su NY (1994) Keys to soldier and winged adult termites (Isoptera) of Florida. Fla Entomol 77:460-474.

Schiefer TL (2018) First record of the introduced ambrosia beetle *Ambrosiophilus Nodulosus* (eggers) in Mississippi, with notes on the distribution of *Ambrosiodmus minor* (stebbing) (coleoptera: curculionidae: scolytinae). Coleopt Bull 72:384-385.

Stokes EC, Franca TSFA, Tang JD (2019) Ongoing termite studies on cross laminated timber (CLT) Panels. Pages 173-178 *in* Proceedings, American Wood Protection Association, May 5-7, 2019, Orlando, FL.

Tsunoda K, Gregory R, Koji D (2010) Laboratory evaluation of the resistance of plastics to subterranean termite, *Coptotermes formosanus* (Blattodea: Rhinotermitidae). Int Biodeterior Biodegradation 64:232-237.

Wang JY, Stirling R, Paul IM, Taylor A, Lloyd J, Kirker G, Lebow S, Mankowski ME, Barnes HM, Morrell JJ (2018) Durability of mass timber structures: A review of the biological risks. Wood Fiber Sci 50:110-127.

Youssef NN, Oliver JB, Ranger CM, Reding ME, Moyseenko JJ, Klein MG, Pappas RS (2009) Field evaluation of essential oils for reducing attraction by the Japanese beetle (Coleoptera: Scarabaeidae). J Econ Entomol 102:1551-1558.

DYNAMIC PROPERTIES OF WOOD OBTAINED BY FREQUENCY RESONANCE TECHNIQUE AND DYNAMIC MECHANICAL ANALYSIS

P. Nop*

Researcher
E-mail: patrik.nop@mendelu.cz

V. Cristini**

Researcher
E-mail: valentino.cristini@mendelu.cz

J. Zlámal**

Researcher
E-mail: jan.zlamal@mendelu.cz

M. Hassan Vand

Researcher
E-mail: mojtaba.vand@mendelu.cz

V. Šeda

Researcher
E-mail: vit.seda@mendelu.cz

J. Tippner**

Assistant Professor
Faculty of Forestry and Wood Technology
Department of Wood Science and Technology
Mendel University in Brno
Brno, Czech Republic
E-mail: jan.tippner@mendelu.cz

Abstract. The study of the viscoelastic properties of wood involves the determination of dynamic parameters. Different methods can be used to determine these parameters, which bring the question of whether these parameters can be considered identical depending on the method used. This study compares the frequency resonance technique and dynamic mechanical analysis for determining the bending dynamic modulus of elasticity (MOED) and damping coefficient tan δ of dry and green wood. Groups of specimens of European beech (*Fagus sylvatica* L.), small-leaved linden (*Tilia cordata* Mill.), European oak (*Quercus robur* L.), and Norway spruce (*Picea abies* L.) wood at three levels of MC were tested with both methods. The bending dynamic modulus of elasticity decreased with increasing MC until the FSP. There were no significant changes in dynamic modulus with increasing MC above FSP. A strong linear correlation between MOED obtained through both methods was found ($r = 0.92$, $r^2 = 0.84$). For the damping coefficient tan δ, the relationship was weaker ($r = 0.57$, $r^2 = 0.32$), and each method showed a different influence of MC on the damping coefficient above the FSP, which leads to the conclusion that the damping coefficient is sensitive to the measurement method.

Keywords: Frequency resonance technique, dynamic mechanical analysis, dynamic modulus of elasticity, damping coefficient, wood.

---

* Corresponding author
** SWST member

INTRODUCTION

Among the main parameters describing the response of a material under dynamic loading are dynamic moduli of elasticity and damping coefficients (Bucur 2006). Due to their high correlation with static moduli ($r = 0.82$) (Karlinasary et al 2008), and with the modulus of rupture ($r = 0.90$) (Hassan et al 2013), dynamic moduli of elasticity are used to predict the strength and stiffness of wood (Hein and Brancheriau 2018; Fernández-Serrano and Villasante 2021), wood-based composites (Hamdan et al 2010; Wang et al 2012), and standing trees (Wang et al 2001; Mora et al 2009). Density (ρ) and dynamic moduli of elasticity are used to calculate the acoustic impedance and the sound radiation coefficient (Wegst 2006; Ahmed and Adamopoulos 2018), and (in combination with the damping coefficient tan δ) to determine the acoustic conversion efficiency (Hossen et al 2018; Danihelová et al 2019). All these vibro-acoustic parameters are used for the selection of quality material for musical instruments (Wegst 2006; Bucur 2016; Ahmed and Adamopoulos 2018; Hossen et al 2018; Tronchin et al 2020). The dynamic parameters for the above-mentioned applications are determined using nondestructive tests (NDT) (Wang et al 2012). Among these NDT methods, the frequency resonance technique (FRT) is one of the most used. This method excites, detects, and analyzes the natural frequencies of the mode shapes arising on the oscillating specimen (Bucur 2006; Brémaud 2012; Baar et al 2016; Hamdan et al 2018; Teles et al 2018). The frequency of these oscillations depends on the material properties, the geometry of the tested specimen, and the way it is fixed. The bending dynamic modulus of elasticity (MOED) of longitudinal-tangential and longitudinal-radial bending mode shape, shear modulus, and Young's modulus is calculated from the first modes of certain oscillation shapes (bending, torsion, and longitudinal) (Bucur 2006; ASTM E1875–20 2020). From the amplitude decrease of free oscillations over time, the logarithmic decrement of damping (LDD) is determined, and the damping coefficient tan δ is further derived from it (Baar et al 2016). The FRT can be used on specimens of various dimension ratios, but standard ASTM E1876 states that the ratio of length to minimum cross-sectional dimension with a value of at least five (5) must be maintained, and a ratio of 20:25 is preferred (ASTM E1876–15 2016). Depending on the sensitivity of the measuring device, and the method of oscillation excitation, the FRT can be used on small samples (Cristini et al 2022), through sizes corresponding to standards for static laboratory tests (Yang et al 2003), and up to beams and logs (Papandrea et al 2022). Besides the described FRT, which is used for small to large samples, the dynamic mechanical analysis (DMA) method can serve for the assessment of small to micro specimens (Salmén et al 2016; Pizzo et al 2018). During the DMA, the oscillating force is applied to the clamped sample, and its response in time is analyzed (Menard 2006). From the force and displacement data, the storage modulus (E_S), which represents the elasticity, and the loss modulus (E_L), which represents energy loss by the internal friction, are determined (Pizzo et al 2018). These two components are used to determine the dynamic modulus of elasticity (complex modulus) as the ratio of stress and deformation (Menard 2006). The phase shift between the stress input and the strain response is the damping coefficient tan δ, and it is calculated as the ratio of E_L and E_S (Brémaud et al 2011). The main use of DMA is to observe the effect of environmental changes (temperature and RH) on the measured parameters of tested materials (Menard 2006). The test parameters (span length, deflection, loading force, and loading frequency) are also factors influencing the results (Ashaduzzaman et al 2020). The size of DMA samples is defined by the type of loading and the associated span of clamps, the internal dimension of a heating or climatic chamber, and the type of device used (Peng et al 2008; Chowdhury et al 2010; Kaboorani and Blanchet 2014). The MC is the factor frequently observed affecting the viscoelastic properties of wood. Below the FSP (approximately 30% MC), an increase of MC of wood causes a rapid decrease in dynamic moduli, and a significant increase in the damping coefficient (Bucur 2006; Matsunaga et al 2000; Lu et al 2012). Further increases above the FSP will not

cause significant changes in the dynamic moduli (Bucur 2006, 2016; Barrett and Hong 2010; Nocetti et al 2014). For the FRT, the influence of increments of MC above FSP on the damping coefficient tan δ has not been described yet (Barré et al 2018). For the DMA, an increase of the damping coefficient tan δ was found when the MC increased above the FSP (Goken et al 2018). The main difference between the above-mentioned methods is the frequency at which the sample oscillates. The FRT is focused on individual resonant frequencies and the area of interest starts at the frequency of the first mode shape. The response in the case of impulse excitation is a combination of all the rising mode shapes (depending on the sensing and excitation point, and sample support). During continuous excitation, a frequency sweep is used to find the frequencies of resonance peaks, so the individual modes are separated (ASTM E1876–15 2016; ASTM E1875–20 2020). The frequency range of DMA starts basically in the static area (0.001 Hz) and ends, depending on the device used, at a frequency of approximately 100 Hz. Using a frequency sweep, the goal is generally not to find resonance peaks (on the contrary, resonance peak is undesirable for data collection), but to show the change in material response (Menard 2006). As the loading frequency increases, the material loses time to relax, and its behavior changes from viscous to elastic. Higher frequencies result in an increase in the dynamic modulus, while causing a reduction in the damping coefficient (Menard 2006).

In this paper, MOED and corresponding damping coefficient tan δ, obtained using FRT and DMA, were compared on the same specimens made from different species and with different MC. The chosen sample size was a compromise meeting the maximum sample size for a DMA device and the ratio of the length to minimum cross-sectional dimension stated by the ASTM standard for FRT. In the case of comparable results, it would be possible to combine these methods in the future and predict parameters for a wide scale of wooden products with various dimensions. For an even wider use including green wood, it is also necessary to focus on deepening the knowledge about the influence of MC on dynamic parameters.

MATERIALS AND METHODS

Materials

Special orthotropic specimens with dimensions of $61 \times 8.4 \times 1.7$ mm (with coefficient of variation [cv] of dimensions = $0.9 \times 2.2 \times 9.6\%$), longitudinal × radial × tangential (Fig 1), were cut from European beech (*Fagus sylvatica* L.), Small-leaved linden (*Tilia cordata* Mill.), European oak (*Quercus robur* L.), and Norway spruce (*Picea abies* L.). Specimens were allocated into three groups of twenty pieces, and every group was conditioned to a different MC. One group had a low MC (LMC), and two groups were above FSP—a medium MC group (MMC), and a high MC group (HMC) (Table 1). The MC was determined using the oven-dry method. Basic density (ρ_b) was determined for all 240 specimens from the ratio of oven-dry mass and volume above the FSP (Table 2).

Measurements

Specimens for both measuring methods were loaded at the center span by longitudinal-tangent bending. To preserve the MC, measurements were done right after each other, FRT first, then immediately DMA, and FRT again (to monitor the impact of MC loss after each measurement). Before each stage of measurement, specimens were weighed. The entire measurement time for one sample was 12 min. Measurements were carried out in laboratory conditions at 24°C and 54% of RH.

Frequency resonance technique. Specimens were supported by flexible pads at the nodes of the first bending mode shape (0.224% and 0.776% of length). Specimen oscillations were excited at the specimen's midpoint by the rubber band. This excitation method was used due to the size and weight of specimens. The hit of a rubber band was sufficient to induce the first bending mode shape but also soft enough so that the loose sample did not reflect out or move on the pads. Vibrations were sensed in the middle of the
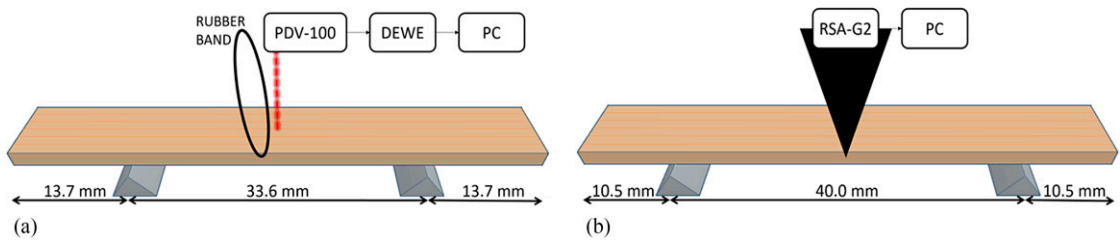
Figure 1.   Setups of frequency resonance technique (a) and dynamic mechanical analysis (b).

specimen using a Doppler laser vibrometer PDV-100 (Polytec, Inc., Baden-Württemberg, DE), and recorded using a dynamic signal acquisition module DEWE-41-T-DSA and DEWESoft (DEWETRON Inc., Grambach, AT), with a sampling frequency of 20 kHz. A minimum of ten hits on the specimen were recorded. The test lasted under a minute.

Dynamic mechanical analysis. For the DMA, three-point bending was carried out using an RSA-G2 device (TA Instruments, New Castle, DE). Specimens were loaded by a spike in the middle and supported by a 40-mm-wide span. The samples were tested using the TRIOS software (TA Instruments), with an initial and minimum axial force value of 0.1 N (the axial force was set 30% higher than the dynamic force), and a displacement of 30 μm. The oscillation frequency was set as a logarithmic sweep from 0.1 to 100 Hz, with 10 points per logarithmic decade. This test was performed for 10 min per sample.

Data Analysis

Frequency resonance technique. For every specimen, the entire length of the signal recorded from FRT was transformed from the time domain into a frequency domain using the fast-Fourier transform processed using MATLAB

(The MathWorks, Inc., Natick, MA). The highest peak with the lowest frequency belongs to the first bending mode. The bending dynamic modulus of elasticity obtained by this method ($MOED_{FRT}$) was calculated from the frequency f using the following equation:

$$MOED_{FRT} = \left(\frac{2f}{2.25\pi}\right)^2 \frac{ml^2}{I} \qquad (1)$$

where m is the mass and l is the length of the specimen. The moment of inertia I was calculated from width (w) and thickness (t) as a:

$$I = \frac{wt^3}{12} \qquad (2)$$

Subsequently, five separate records (each for one of the five selected hits with the highest amplitude) were exported from the signal. For each record with a minimum of 25 periods of oscillation, the LDD was determined. From the LDD, the damping coefficient tan δ was calculated using Eq 3. As a representative damping coefficient of the specimen, a median from five tan δ was determined.

$$\tan \delta = \frac{LDD}{\pi} \qquad (3)$$

Dynamic mechanical analysis. The main results obtained by DMA were storage modulus

Table 1. Medians of MC of each sample group.

	LMC		MMC		HMC	
Group	MC (%)	cv (%)	MC (%)	cv (%)	MC (%)	cv (%)
Beech	11.7	4.6	49.7	6.4	78.8	6.2
Linden	10.2	7.0	47.9	10.0	81.5	7.1
Oak	11.1	3.0	50.5	8.1	82.8	10.6
Spruce	11.1	2.9	47.3	8.3	84.3	15.5

Table 2. Medians of basic density values of species.

Species	ρ_b (kg · m^{-3})	cv (%)
Beech (*Fagus sylvatica* L.)	558.8	3.5
Linden (*Tilia cordata* Mill.)	360.8	4.8
Oak (*Quercus robur* L.)	526.9	5.8
Spruce (*Picea abies* L.)	412.3	11.1

(E_L) and loss modulus (E_S), which are components of the stress (σ - E_L is 90° out of phase with the strain ε, and E_S is in the phase with the strain).

$$E_L = \frac{\sigma \sin \delta}{\varepsilon} \qquad (4)$$

$$E_S = \frac{\sigma \cos \delta}{\varepsilon} \qquad (5)$$

The damping coefficient tan δ represented a phase lag between the stress and the strain and was calculated as the ratio of E_L to E_S.

$$\tan \delta = \frac{E_L}{E_S} \qquad (6)$$

The bending dynamic modulus of elasticity (MOED$_{DMA}$) is a complex combination of E_L and E_S.

$$\text{MOED}_{DMA} = \frac{\sigma}{\varepsilon} = E_S + iE_L = \sqrt{E_S{}^2 + E_L{}^2}$$
$$(7)$$

The MC of specimens decreased during the 10-min-long DMA depending on the moisture group, and (in the case of MC above the FSP) also depending on species (Table 3). Based on the weight method, MC loss was determined from known MC before and MC after the DMA test. For every specimen from groups MMC and HMC, the average of MC before and MC after the DMA test is given for the next data evaluation. DMA results were reported for each testing frequency. From all sample groups, the median for each testing frequency was calculated (Figs 2 and 3). For further statistical evaluation, the median value across frequencies was determined for each sample. The statistical comparison of

Table 3. Medians of MC loss during the DMA of each sample group.

Group	LMC		MMC		HMC	
	MC loss (%)	cv (%)	MC loss (%)	cv (%)	MC loss (%)	cv (%)
Beech	1.08	25.9	10.38	15.4	11.88	20.6
Linden	1.00	179.6	16.50	12.1	18.07	10.3
Oak	0.85	23.1	9.33	19.8	12.19	13.6
Spruce	0.87	24.1	15.81	14.9	20.61	15.3

data obtained by both methods was done using one-way ANOVA, with a significance level of 0.05 and 0.01, in the MATLAB environment. The steepness of the function (stp) was determined according to the first term (*a*) of the linear regression $y = ax + b$.

RESULTS AND DISCUSSION

The MC loss during the DMA test was comparable for species in LMC groups, up to 1%. In groups with MC above the FSP, the differences between the species were observed. Wood species with lower ρ_b had a bigger MC loss during the experiment.

The DMA showed that the change from viscous to elastic behavior when changing frequency (Menard 2006) occurred earlier in dry wood than in wood at a higher MC (Fig 2). Resonance peaks at the same frequencies (39.8 and 63 Hz) were found in the data of E_L for all specimens, which affected the determination of MOED$_{DMA}$ and the damping coefficient at these frequencies. Since it concerns the same frequencies for all specimens (regardless of MC and species), which are far from their resonance frequencies found by FRT (from 1240 to 2708 Hz), a measurement error caused by a device or clamps resonance was considered. According to Bucur (2006), and Nocetti et al (2014), the modulus of elasticity decreases with increasing MC. The results from DMA show that compared with LMC, moduli of MMC and HMC decreased by: 40% and 52% for beech, 28% and 46% for linden, 27% and 43% for oak, and 37% and 52% for spruce respective. So, for species with a higher modulus of elasticity, there is a more significant decrease with increasing MC.

All samples showed a drop or lack of the damping coefficient values at the lowest frequencies, caused by very low or negative values of E_L (Fig 3). From the erroneous resonance peaks, described earlier, all damping coefficients followed an increase and convergence of all samples at the same value. The middle area of the measurement (0.5-10 Hz) showed a trend of a slight decrease with increasing frequency, which agrees with
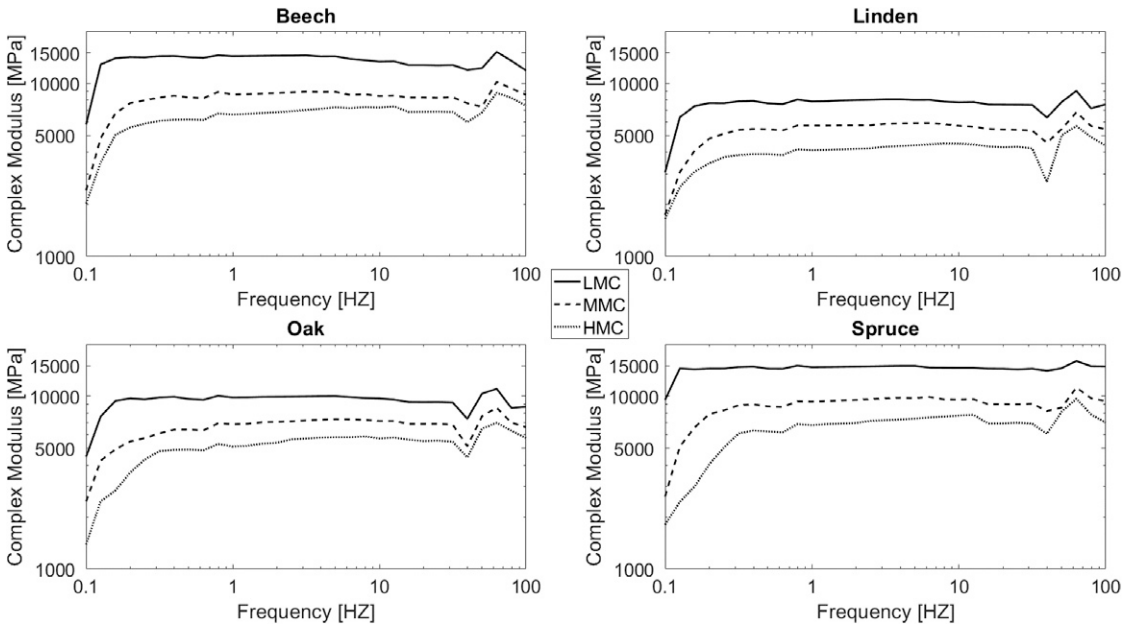
Figure 2.   Medians of complex dynamic moduli of elasticity of species groups with different MC at varying load frequency—determined by dynamic mechanical analysis.
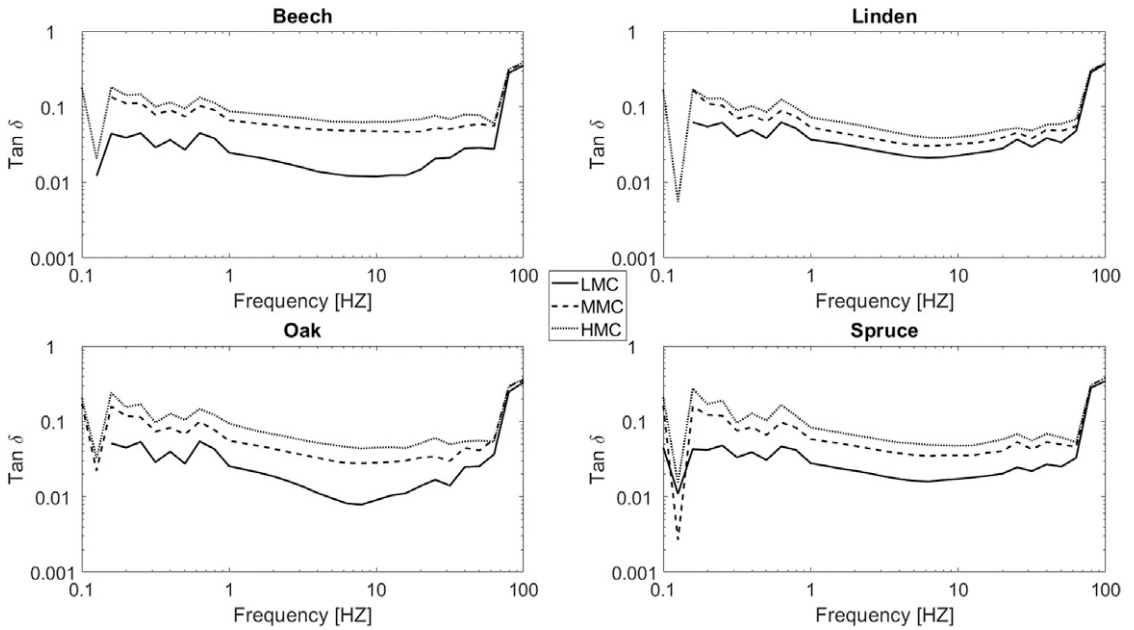

Figure 3.   Medians of damping coefficients determined by dynamic mechanical analysis at varying load frequency.

Menard's (2006) description of the influence of the loading frequency on material behavior determined by DMA.

As expected for DMA above FSP, the damping coefficient increased with rising MC (Goken et al 2018). For individual species, the DMA revealed a rising damping coefficient for MMC and HMC compared with LMC by: 161% and 253% for beech (stp $= 11\,e^{-4}$), 39% and 74% for linden (stp $= 4\,e^{-4}$), 107% and 204% for oak (stp $= 9\,e^{-4}$), and 95% and 167% for spruce (stp $= 6\,e^{-4}$) respective. This could lead to the conclusion that with higher ρ_b, the damping coefficient tan δ increases rapidly with increasing MC. Nevertheless, by focusing on individual species and their MC groups, no significant change was observed when the ρ_b changed. In case, there was any slight change observed, it was a decrease in the damping coefficient with increasing ρ_b (Fig 4), For the DMA, species with a higher ρ_b showed a faster increment of the damping coefficient with increasing MC. Brémaud et al (2009, 2010) stated that extractives content, chemical composition, and properties related to MC have a significant influence on the damping coefficient

tan δ. This confirms that the steepness of the damping coefficient increases with increasing MC and is influenced not only by ρ_b, but also by the properties of the species itself.

Since the results were comparable for FRT in individual MC groups before and after DMA tests, values are stated (Table 4) as the unified medians from the average of LMC, MMC, and HMC before and after performing the DMA.

The bending dynamic modulus of elasticity obtained by DMA was statistically comparable within the individual species for both groups above FSP (MMC and HMC) with ($p = 0.01$), beech even with ($p = 0.05$). No species had statistically comparable MOED$_{DMA}$ of the LMC group with MMC and HMC groups. Similar results were obtained for MOED$_{FRT}$. Individual species had comparable MMC and HMC groups with ($p = 0.01$), beech and oak even with ($p = 0.05$). No species had statistically comparable MOED$_{FRT}$ of the LMC group with groups above FSP. Both methods agreed with the assumption that there is no statistically significant change in MOED above FSP, with increasing
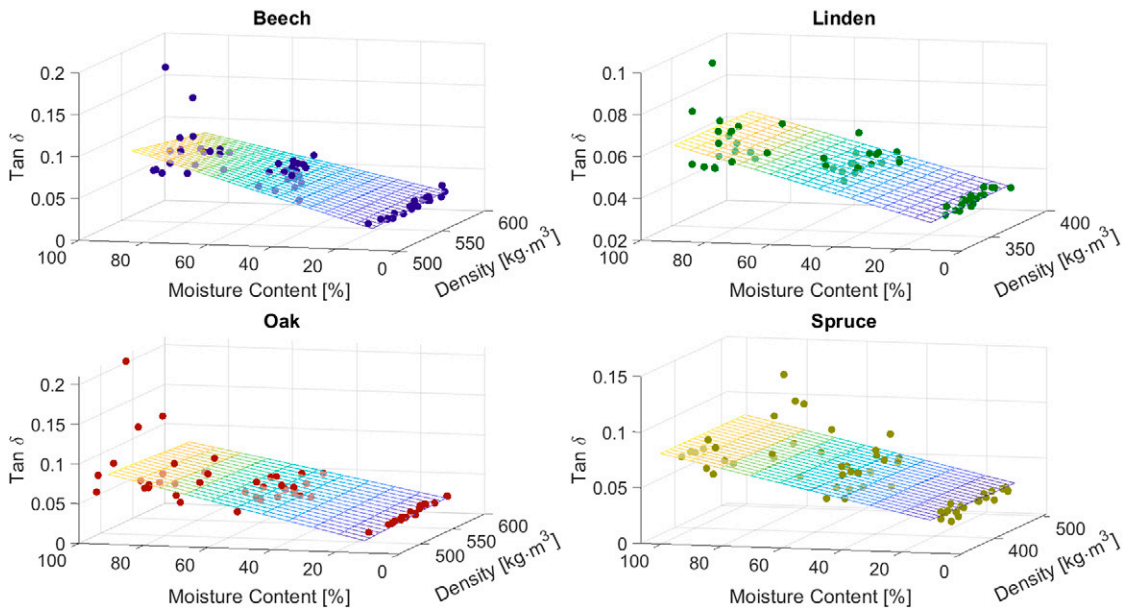

Figure 4.   Increasing damping coefficient with increasing MC for individual species.

Table 4. Medians of MOED and tan δ for species with different MC.

Species	MC	FRT				DMA			
		MOED (MPa)	cv (%)	tan δ (−)	cv (%)	MOED (MPa)	cv (%)	tan δ (−)	cv (%)
Beech	LMC	17 297	8.9	0.0093	15.7	14 117	14.7	0.0227	12.9
	MMC	11 563	8.9	0.0206	30.6	8 448	14.2	0.0592	15.3
	HMC	10 721	12.6	0.0195	27.3	6 768	33.5	0.0800	35.5
Linden	LMC	10 222	9.9	0.0124	7.1	7 758	12.4	0.0339	5.3
	MMC	7 876	12.2	0.0162	16.2	5 616	12.1	0.0473	9.3
	HMC	6 467	17.0	0.0179	16.8	4 192	19.8	0.0589	17.7
Oak	LMC	12 088	19.9	0.0087	14.6	9 697	19.8	0.0222	10.1
	MMC	9 160	16.6	0.0137	24.8	7 048	15.4	0.0459	13.6
	HMC	7 976	17.5	0.0139	23.5	5 524	57.2	0.0676	49.5
Spruce	LMC	17 704	21.0	0.0073	12.5	14 595	24.0	0.0258	15.8
	MMC	11 541	10.9	0.0134	31.4	9 137	11.9	0.0502	16.2
	HMC	10 753	23.6	0.0148	31.2	6 935	42.4	0.0688	32.5

MC (Bucur 2006; Nocetti et al 2014). A comparison of MOED between both methods showed no statistical difference only for the spruce LMC group ($p = 0.01$), otherwise, the methods do not have comparable MOED within the species and their individual MC groups. Medians of MOED$_{DMA}$ were smaller than MOED$_{FRT}$, and were similar for all species, depending on the MC group: LMC of 18.4% for beech, 24.1% for linden, 19.8% for oak, and 17.6% for spruce; MMC of 26.9% for beech, 28.7% for linden, 23.1% for oak, and 20.8% for spruce; HMC of 36.9% for beech, 35.2% for linden, 30.7% for oak, and 35.5% for spruce. The data from both methods show that, as a function of MC, MOED$_{FRT}$, and MOED$_{DMA}$ copy a similar trend (Fig 5).

The damping coefficients obtained by DMA are higher than those obtained by FRT. Similar results were found in one of the few papers comparing DMA and FRT results of the damping coefficient tan δ on the mulberry wood with MC of 1.4% (Se Golpayegani et al 2012). Thus, these results for LMC groups were expected. Above FSP, a further increase was expected for DMA (Goken et al 2018), which again would be similarly steep for both methods (for FRT, it has not been described yet [Barré et al 2018]). This has been confirmed for DMA data only (Fig 6). The FRT results showed that above the FSP, the damping coefficients had similar trends as

dynamic moduli, ie that there were no statistically significant changes with increasing MC. For all species, the damping coefficients tan δ were comparable between their MMC and LMC groups ($p = 0.05$). For the damping coefficient obtained by DMA, MMC and HMC groups were comparable only for spruce ($p = 0.01$).

As the results indicate, the methods are very similar in determining MOED, just with shifted values (Fig 7). Through multiple linear regression from all data (using function "regress"—Matlab) the coefficient $c = 0.7567$ to convert MOED$_{FRT}$ to MOED$_{DMA}$, and $c = 1.2813$ to convert MOED$_{DMA}$ to MOED$_{FRT}$ were calculated. MOED$_{DMA}$ and MOED$_{FRT}$ had strong linear correlations ($r = 0.92$, $r^2 = 0.84$). This correlation is very similar to the correlation between static bending MOE and dynamic bending MOED$_{FRT}$ ($r = 0.98$, $r^2 = 0.96$) (Chauhan and Sethy 2016). The DMA operates at the boundary between statics and dynamics, with loading frequencies ranging from 0.1 to 100 Hz. As the static moduli have lower values than dynamic moduli, DMA corresponds to lower MOED values. A comparison of both methods for determining the damping coefficient tan δ showed a weaker correlation ($r = 0.57$, $r^2 = 0.32$). When comparing only the LMC groups (disregarding the influence of MC) the correlation coefficient remained almost unchanged. The correlation between MOED and the
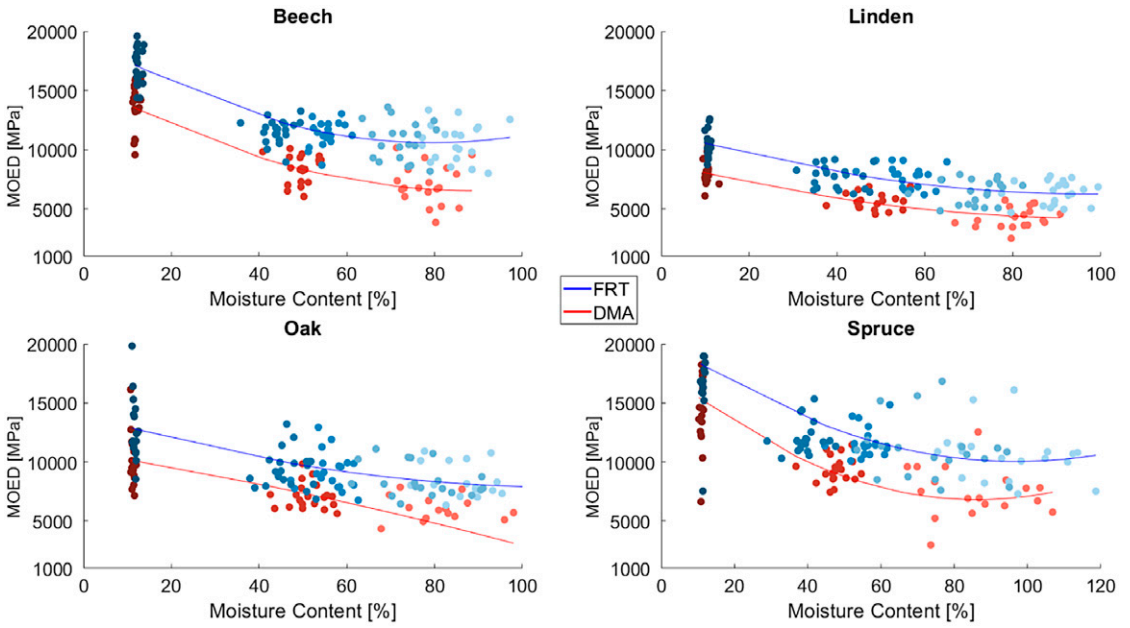
Figure 5.   Comparison of bending dynamic modulus of elasticity (MOED) obtained by frequency resonance technique (FRT) and dynamic mechanical analysis (DMA).
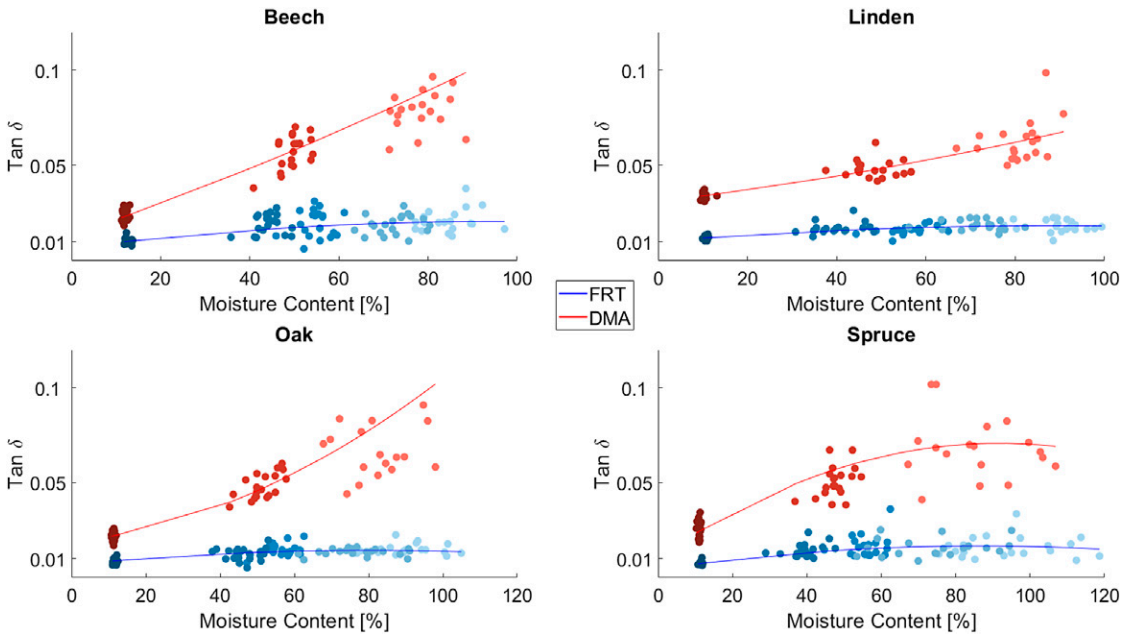

Figure 6.   Comparison of damping coefficient obtained by frequency resonance technique (FRT) and dynamic mechanical analysis (DMA).
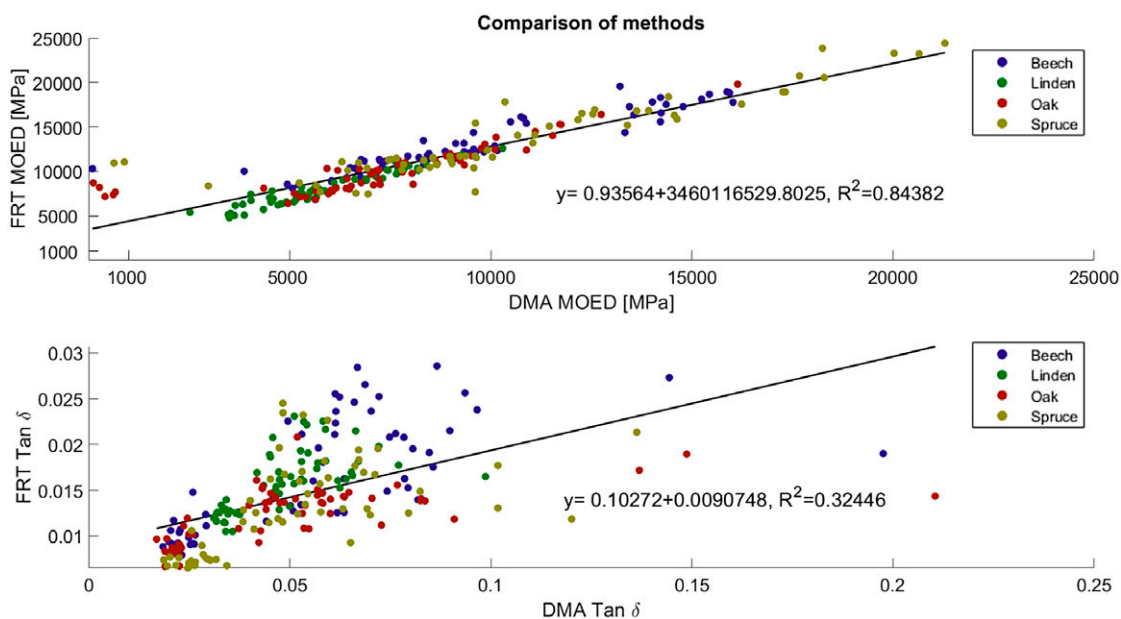
Figure 7.   Comparison of dynamic parameters obtained by frequency resonance technique (FRT) and dynamic mechanical analysis (DMA).

damping coefficient tan δ was moderate for FRT ($r = 0.42$) and stronger for DMA ($r = 0.65$).

CONCLUSIONS

- The DMA showed that the damping coefficient increased with increasing MC, and increased faster with increasing MC for species with a high ρ_b (oak, beech with stp = $9e^{-4}$; $11e^{-4}$) than for species with lower ρ_b (linden, spruce with stp = $4e^{-4}$; $6e^{-4}$).
- The FRT showed that the damping coefficient values do not change significantly above the FSP.
- Same-size specimens showed that MOED determined using FRT was 24-28% more than MOED determined using DMA, with a strong linear correlation ($r = 0.92$, $r^2 = 0.84$). The influence of the scale while maintaining the ratio of dimensions and furthermore, the influence of the change of geometry should be verified.
- For further research, it is necessary to focus in more detail on the damping coefficient tan δ and the factors influencing it. Based on the results of this paper, the damping coefficient tan δ obtained by DMA and the damping coefficient tan δ obtained by FRT should not be confused.

DECLARATION OF COMPETING INTEREST

The authors declare that they have no known competing financial interests or personal relationships that could have appeared to influence the work reported in this paper.

REFERENCES

Ahmed SA, Adamopoulos S (2018) Acoustic properties of modified wood under different humid conditions and their

relevance for musical instruments. Appl Acoust 140:92-99. https://doi.org/10.1016/j.apacoust.2018.05.017

American Society for Testing and Materials, ASTM E1875 – 20 (2020). Standard test method for dynamic Young's modulus, shear modulus, and Poisson's ratio by sonic resonance. Philadelphia. https://doi.org/10.1520/E1875-20

American Society for Testing and Materials, ASTM E1876 - 15 (2016). Standard test method for dynamic Young's modulus, shear modulus, and Poisson's ratio by impulse excitation of vibration. Philadelphia. https://doi.org/10.1520/E1876-08.2

Ashaduzzaman M, Hale MD, Ormondroyd GA, Spear MJ (2020) Dynamic mechanical analysis of Scots pine and three tropical hardwoods. Int Wood Prod J 11(4):189-203. https://doi.org/10.1080/20426445.2020.1799910

Baar J, Tippner J, Gryc V (2016) Wood anatomy and acoustic properties of selected tropical hardwoods. IAWA J 37(1):69-83. https://doi.org/10.1163/22941932-20160121

Barré JB, Bourrier F, Brancheriau L, Bertrand D, Rey F (2018) Effects of fungal decay on elasticity and damping of small-diameter silver fir logs assessed by the transverse vibration resonant method. Wood Sci Technol 52(2):403-420. https://doi.org/10.1007/s00226-017-0961-2

Barrett JD, Hong JP (2010) Moisture content adjustments for dynamic modulus of elasticity of wood members. Wood Sci Technol 44(3):485-495. https://doi.org/10.1007/s00226-009-0292-z

Brémaud I (2012) Acoustical properties of wood in string instruments soundboards and tuned idiophones: Biological and cultural diversity. J Acoust Soc Am 131(1):807-818. https://doi.org/10.1121/1.3651233

Brémaud I, Gril J, Thibaut B (2011) Anisotropy of wood vibrational properties: Dependence on grain angle and review of literature data. Wood Sci Technol 45(4):735-754. https://doi.org/10.1007/s00226-010-0393-8

Brémaud I, Minato K, Langbour P, Thibaut B (2010) Physico-chemical indicators of inter-specific variability in vibration damping of wood. Ann For Sci 67(7):707. https://doi.org/10.1051/forest/2010032

Brémaud I, Minato K, Thibaut B (2009) Mechanical damping of wood as related to species classification: A preliminary survey. Pages 1–7 in Proceedings, 6th Plant Biomechanics Conference Cayenne, November 16–21, Cayenne, French Guiana. papers3://publication/uuid/80AA77A1-F445-4065-A76F-7AEFF49E3F1C

Bucur V (2006) Acoustics of wood. Theory of and Experimental Methods for the Acoustic Characterization of Wood. Pages 39–104 in TE Timell, R Wimmer, eds CRC Press, Boca Raton, FL. https://doi.org/10.1201/9780203710128

Bucur V (2016) Handbook of materials for string musical instruments. Mechanical Characterisation of Materials for String Instrument. Pages 93–126. Springer International Publishing, Switzerland. https://doi.org/10.1007/978-3-319-32080-9

Chauhan S, Sethy A (2016) Differences in dynamic modulus of elasticity determined by three vibration methods and their relationship with static modulus of elasticity. Maderas Cienc Tecnol 18(2):373-382. https://doi.org/10.4067/S0718-221X2016005000034

Chowdhury S, Fabiyi J, Frazier CE (2010) Advancing the dynamic mechanical analysis of biomass: Comparison of tensile-torsion and compressive-torsion wood DMA. Holzforschung 64(6):747-756. https://doi.org/10.1515/HF.2010.123

Cristini V, Tippner J, Nop P, Zlámal J, Hassan Vand M, Šeda V (2022) Degradation of beech wood by Kretzschmaria deusta: Its heterogeneity and influence on dynamic and static bending properties. Holzforschung 76(9):813-824. https://doi.org/10.1515/hf-2022-0039

Danihelová A, Spišiak D, Reinprecht L, Gergel T, Vidholdov Z, Ondrejka V (2019) Acoustic properties of Norway spruce wood modified with staining fungus (*Sydowia polyspora*). BioResources 14(2):3432-3444. https://doi.org/10.15376/biores.14.2.3432-3444

Fernández-Serrano Á, Villasante A (2021) Longitudinal, transverse and ultrasound vibration for the prediction of stiffness using models incorporating features in *Pinus sylvestris* timber. Eur J Wood Wood Prod 79(6):1541-1550. https://doi.org/10.1007/s00107-021-01707-0

Goken J, Fayed S, Schafer H, Enzenauer J (2018) A study on the correlation between wood moisture and the damping behaviour of the tonewood spruce. Acta Phys Pol A 133(5):1241-1260. https://doi.org/10.12693/APhysPolA.133.1241

Hamdan S, Rahman MR, Jusoh I, Wahid HA (2018) Dynamic Young's modulus and moisture content of tropical wood species across Sap, median, and internal wood regions. BioResources 13(2):2907-2915. https://doi.org/10.15376/biores.13.2.2907-2915

Hamdan S, Talib ZA, Rahman MR, Ahmed AS, Islam MS (2010) Dynamic Young's modulus measurement of treated and post-treated tropical wood polymer composites (WPC). BioResources 5(1):324-342.

Hassan KTS, Horáček P, Tippnera J (2013) Evaluation of stiffness and strength of scots pine wood using resonance frequency and ultrasonic techniques. BioResources 8(2):1634-1645. https://doi.org/10.15376/biores.8.2.1634-1645

Hein PRG, Brancheriau L (2018) Comparison between three-point and four-point flexural tests to determine wood strength of Eucalyptus specimens. Maderas Cienc Tecnol 20(3):333-342. https://doi.org/10.4067/S0718-221X2018005003401

Hossen MF, Hamdan S, Rahman MR (2018) Investigation of the acoustic properties of chemically impregnated Kayu Malam wood used for musical instrument. Adv Mater Sci Eng 2018. https://doi.org/10.1155/2018/7829613

Kaboorani A, Blanchet P (2014) Determining the linear viscoelastic region of sugar maple wood by dynamic

mechanical analysis. BioResources 9(3):4392-4409. https://doi.org/10.15376/biores.9.3.4392-4409

Karlinasary L, Wahyuna ME, Nugroho N (2008) Nondestructive ultrasonic testing method for determining bending strength properties of Gmelina wood (*Gmelina arborea*). J Trop For Sci 20(2):1-12.

Lu J, Jiang J, Wu Y, Li X, Cai Z (2012) Effect of moisture sorption state on vibrational properties of wood. Forest Prod Journal 62(3):171-176. https://doi.org/10.13073/0015-7473-62.3.171

Matsunaga M, Obataya E, Minato K, Nakatsubo F (2000) Working mechanism of adsorbed water on the vibrational properties of wood impregnated with extractives of pernambuco (*Guilandina echinata* Spreng.). J Wood Sci 46(2):122-129. https://doi.org/10.1007/BF00777358

Menard KP (2006) Dynamic mechanical analysis, 2nd edition. CRC Press, Boca Raton, FL. https://doi.org/10.1007/978-3-540-29805-2_1224

Mora CR, Schimleck LR, Mahon JM, Isik F, Mahon JM, Clark A, Daniels RF (2009) Relationships between acoustic variables and different measures of stiffness in standing *Pinus taeda* trees. Can J For Res 39(8):1421-1429. https://doi.org/10.1139/X09-062

Nocetti M, Brunetti M, Bacher M (2014) Effect of moisture content on the flexural properties and dynamic modulus of elasticity of dimension chestnut timber. Eur J Wood Wood Prod 73(1):51-60. https://doi.org/10.1007/s00107-014-0861-1

Papandrea SF, Cataldo MF, Bernardi B, Zimbalatti G, Proto AR (2022) The predictive accuracy of modulus of elasticity (MOE) in the wood of standing trees and logs. Forests 13(8):1273. https://doi.org/10.3390/f13081273

Peng Y, Shi SQ, Kim MG (2008) Effect of temperature on the dynamic mechanical properties of resin film and wood. For Prod J 58(12):68-74.

Pizzo B, Pecoraro E, Lazzeri S (2018) Dynamic mechanical analysis (DMA) of waterlogged archaeological wood at room temperature. Holzforschung 72(5):421-431. https://doi.org/10.1515/hf-2017-0114

Salmén L, Stevanic JS, Olsson AM (2016) Contribution of lignin to the strength properties in wood fibres studied by dynamic FTIR spectroscopy and dynamic mechanical analysis (DMA). Holzforschung 70(12):1155-1163. https://doi.org/10.1515/hf-2016-0050

Se Golpayegani A, Brémaud I, Gril J, Thevenon MF, Arnould O, Pourtahmasi K (2012) Effect of extractions on dynamic mechanical properties of white mulberry (Morus alba). J Wood Sci 58(2):153-162. https://doi.org/10.1007/s10086-011-1225-7

Teles RF, De Souza MR, Wimmer P (2018) Acoustical properties of 10 Amazonian hardwoods. Pages 1675–1681 *in* Proceedings 25th International Congress on Sound and Vibration 2018, ICSV 2018: Hiroshima Calling, July 3, 2018, Hiroshima, Japan.

Tronchin L, Manfren M, Vodola V (2020) Sound characterization through intensity of acoustic radiation measurement: A study of Persian musical instruments. Appl Sci 10(2):633. https://doi.org/10.3390/app10020633

Wang X, Ross RJ, McClellan M, Barbour RJ, Erickson JR, Forsman JW, McGinnis GD (2001) Nondestructive evaluation of standing trees with a stress wave method. Wood Fiber Sci 33(4):522-533.

Wang Z, Li L, Gong M (2012) Measurement of dynamic modulus of elasticity and damping ratio of wood-based composites using the cantilever beam vibration technique. Constr Build Mater 28(1):831-834. https://doi.org/10.1016/j.conbuildmat.2011.09.001

Wegst UGK (2006) Wood for sound. Am J Bot 93(10):1439-1448. https://doi.org/10.3732/ajb.93.10.1439

Yang JL, Ilic J, Wardlaw T (2003) Relationships between static and dynamic modulus of elasticity for a mixture of clear and decayed eucalypt wood. Aust For 66(3):193-196. https://doi.org/10.1080/00049158.2003.10674911

DENSIFICATION OF NEW ZEALAND-GROWN EUCALYPTUS SPECIES: EFFECT OF GRAIN ORIENTATION AND DENSIFICATION PROCESS ON WOOD PROPERTIES

R. Sargent*

Senior Technologist
Scion, Titokirangi Drive, Rotorua 3010, New Zealand
Email: rosie.sargent@scionresearch.com

M. Mikuljan

Assistant Researcher
Email: marica.mikuljan@innorenew.eu

A. Kutnar†

Director
InnoRenew CoE, Livade 6a, Izola 6310, Slovenia
and
University of Primorska, Andrej Marušič Institute
Muzejski trg 2, Koper 6000, Slovenia
Email: andreja.kutnar@innorenew.eu

Abstract. *Eucalyptus fastigata* and *Eucalyptus nitens* were densified using a thermo-hydro-mechanical (THM) densification process. The THM treatment was applied either as a surface densification of one wood surface or as a bulk densification of the entire wood thickness. To understand the effect of grain orientation on final wood properties, both quarter-sawn and flat-sawn boards were densified. The *E. nitens* boards were able to be compressed to a greater degree without being damaged compared with the *E. fastigata* boards. This led to substantial increases in surface hardness and surface density in *E. nitens*. Additionally, levels of set-recovery (irreversible swelling from contact with water) for bulk densified *E. nitens* were substantially lower than *E. fastigata* and lower than literature values for other species with a similar density. The reason for this unusually low set-recovery is not known, but it is of potential interest for the commercial application of densified wood, where set-recovery is unacceptable and would need to be eliminated. Density profiles showed that the peak density was generally at, or very close to, the wood surface, giving the maximum increase in surface hardness for a given degree of densification. The properties following densification were not substantially different between the quarter-sawn and flat-sawn boards, suggesting that densification was effective irrespective of grain orientation.

Keywords: Eucalyptus, wood densification, density profile, Brinell hardness, hardwood, grain orientation.

INTRODUCTION

Increased demand worldwide for high-value wood products, plus concerns about deforestation and unsustainable logging, have increased interest in plantation-grown timbers that will perform well in demanding situations. There is also increasing interest in utilizing a wider range of wood species for sawn timber and using wood modification as a method of improving wood properties. *Eucalyptus*

nitens (H.Deane & Maiden) Maiden (*E. nitens*) and *Eucalyptus fastigata* H.Deane & Maiden (*E. fastigata*) are grown in plantations in New Zealand but are not currently well utilized for high-value sawn timber. Both species have an attractive hardwood grain, similar to other species of Australian-grown eucalyptus that are commonly used for interior applications such as hardwood flooring. Neither species is as hard as oak, or Australian-grown hardwoods (Janka hardness of ~5 kN for *E. fastigata*, and *E. nitens*, compared with ~7 kN for American Oak and

———
* Corresponding author
† Society of Wood Science & Technology member

~6 kN for Victorian Ash) and are thus not sufficiently hard for flooring applications. Many mechanical properties of wood, eg, MOE and hardness, are proportional to wood density (Rautkari et al 2011; Navi and Sandberg 2012a), so increasing the wood density via densification offers a potential route to improving the surface hardness of these species. Densification of wood has been studied for a long time, having been initially developed in the early 20th century, but there has been increased scientific interest in the last 30 yr (Kutnar et al 2015).

Wood densification is a process where wood cells are mechanically compressed so they deform, reduce the void spaces, and flatten, preferably without the cell wall fracturing. If the cell deformation can be retained after the compression force is removed, this will increase the wood density and, consequently, the wood hardness. To ensure that the wood retains its densified shape after the compression force is released, it is important that the cells are softened and the stresses that form during compression are released. This is done by ensuring the wood components (mainly lignin) are above the glass transition temperature (T_g) during compression, and the wood is cooled to below the glass transition temperature before the compressive load is released (Navi and Sandberg 2012a). Because the glass transition temperature of lignin and hemicellulose are a function of temperature and moisture content (MC) (Lenth and Kamke 2001a; Kutnar and Sernek 2007), the correct combination of press temperature and wood MC is required to ensure the cells are densified without being damaged, and stresses are adequately relieved to retain the compressed shape. To ensure the wood remains in a softened state, the wood either needs to be at a high temperature or maintain a consistently high MC during the densification process. For example, Lenth and Kamke (2001a) observed softening at 200°C in *Pinus taeda* at 0% MC, but this reduced to <100°C at 10-15% MC. To maintain high moisture contents at temperatures >100°C, elevated pressures are required (Lenth and Kamke 2001b). For this reason, densification is often performed in a "closed system" where mechanical force can be applied in a pressurized steam atmosphere (Navi and Sandberg 2012a).

Once the wood is set in its compressed state, contact with liquid water or changes in air humidity often lead to the wood swelling and regaining some of its original dimensions, a process known as "set-recovery" (Navi and Sandberg 2012a). Preventing set-recovery has been the subject of numerous studies (Kutnar and Kamke 2012; Laine et al 2013). Postdensification heat treatment, such as pressure steaming or thermal modification, is a very promising method of preventing set-recovery (Laine et al 2016). Kutnar and Kamke (2012) compared levels of set-recovery after densifying poplar in either saturated or atmospheric pressure steam, finding dramatically lower levels of set-recovery following water soaking for the samples compressed in pressurized (saturated) steam. Set-recovery is typically measured by comparing the initial specimen thickness with the thickness following water soaking and oven drying. This is often repeated over several water soaking steps (Fu et al 2017). Laine et al (2013) compared several different methods of quantifying set-recovery, including water soaking in hot or cold water and through changes in ambient humidity. They noted that set-recovery through changes in RH was more likely to replicate the conditions that many target products for densified wood would encounter in service, eg, wooden flooring.

Process conditions such as press temperature, initial wood temperature and MC, the degree of compression, and the rate of compression all impact the density profile and peak density (PD) of the compressed wood (Rautkari et al 2011; Zhou et al 2019). This gives the possibility of increasing the density throughout the entire wood thickness or restricting the densification to the wood surface, leaving the rest of the wood unchanged (Navi and Sandberg 2012b). Surface densification has the advantage of retaining more of the original wood thickness during densification and gives a product with a high surface hardness but with only a small increase in the overall density and weight of the wood.

Densification is typically performed in a radial orientation (compression force perpendicular to the growth ring orientation). This preferentially densifies the larger thinner-walled earlywood fibers (Kutnar et al 2015), and corresponds to the grain orientation typical of sawn timber of many softwoods (flat-sawing or back-sawing). Many eucalypt species are typically milled into quarter-sawn boards where the growth rings are perpendicular to the long face of the board. Densifying these boards would compress the wood in a tangential direction, meaning that both the earlywood and latewood bands are compressed at the same time. Wang and Cooper (2005) densified black spruce and balsam fir with three different grain orientations (growth rings oriented 0°, 45°, and 90° from the wide face of the board). For balsam fir, the density profile before densification showed distinct peaks for the late wood bands in the 0° (flat-sawn boards). These differences were retained after densification, with both the earlywood and latewood density increasing. For the 45° and 90° (quarter-sawn) boards, the vertical density profile was very uniform prior to modification, and following modification, there were definite density peaks near each surface of the board with a lower density in the center. For surface densification, where these density peaks are being sought, grain orientation may have a significant impact on the density profile, and hence on the success of the process (Wang and Cooper 2005).

Despite densification being a well-known process, it has not yet been investigated for New Zealand-grown eucalypts. Koumba et al (2014) densified Chilean-grown *E. nitens* and *Pinus radiata* in a steam environment but did not report any mechanical properties or dimensional stability data. Balasso et al (2020) densified a thin lamella of *E. nitens*, *P. radiata*, and Tasmanian Oak (a mix of *Eucalyptus regnans* and *Eucalyptus obliqua*). In this study, timber from *E. nitens* and *E. fastigata* has been densified using two densification processes (surface- and bulk densification), and with two grain orientations (flat-sawn and quarter-sawn), and then the properties of the densified wood were investigated.

MATERIALS AND METHODS

Densification

E. fastigata boards were sourced from a previous sawing study (Jones et al 2010). The trees were 25 yr old, and boards were cut from either the butt log or the 1st log of each tree. The boards were cut from 10 different trees. The *E. nitens* boards were also sourced from a sawing study using 18-yr-old trees grown in the southern South Island of New Zealand. These boards were all from the 1st log and were also cut from 10 different trees. For each species, equal numbers of flat- and quarter-sawn boards were cut to 500 mm long and were planed to 20 mm thick. Most boards were 100 mm wide, but some *E. nitens* boards were 90-95 mm wide. Each 500-mm-long board was cut into two matched 250-mm-long boards. The 250-mm-long boards were assigned to the following treatments:

- Undensified control
- Surface densification
- Bulk densification

The optimum press force and press closing gap (target densification thickness) were determined for each species prior to starting the experiments, to ensure a high degree of densification without cracking or splitting in the wood. The quarter-sawn *E. fastigata* boards had significant issues with bulk densification, where densifying to a final thickness below 16 mm caused substantial cracking and darkening of the wood. This meant that the *E. fastigata* was densified to a greater target thickness (ie, less densification) than the *E. nitens*.

For the experiment, for each combination of species, grain orientation, and densification process, 10 replicates were used, giving a total of 120 boards for property testing.

The thermo-hydro-mechanical (THM) densification treatment was applied as surface densification and as bulk densification. Table 1 presents the parameters used in the study.

The final thickness of the densified samples was determined by placing metal bars of an appropriate

Table 1. Parameters of the THM surface and bulk densification processes used in this study.

	Surface	Bulk
Top platen initial temperature (°C)	170	170
Bottom platen initial temperature (°C)	20	170
Press force (kPa)	3000	3000
Hold time at the initial temperature (minutes)	3	3
Heating rate to a high temperature (°C/min)	20	20
Top platen high temperature (°C)	200	200
Bottom platen high temperature (°C)	20	200
Top platen cooling temperature (°C)	60	60
Bottom platen cooling temperature (°C)	60	60
Target densified thickness[a] (mm)	17/16 (E. fastigata/E. nitens)	16/10 (E. fastigata/E. nitens)
Densification ratio[b]	0.15/0.2	0.2/0.5

[a] Target densified thickness is the thickness of the metal stops used to control the final press gap.

[b] Densification ratio is a theoretical degree of compression based on the nominal initial thickness and the press gap.

thickness (Table 1) into the press to control the final press gap.

The press was heated to the target temperature (Table 1). Then, the samples were loaded into the press, and the densification process was implemented according to the parameters in Table 1.

Prior to densification, the weight and dimensions of each board were measured. Following densification, once the boards were cool enough to handle (usually after 10-15 min), the width and thickness of the boards were measured again. The spring-back (recovery of board thickness immediately after pressing) and the width expansion of each board can be calculated:

$$\text{Spring-back} = \left(\frac{t_d - t_t}{t_o - t_t}\right) \times 100 \ [\%] \qquad (1)$$

Where:

t_o is the initial (uncompressed) thickness of the sample,

t_d is the thickness after densification

t_t is the target thickness (press gap)

Width expansion is defined by Eq 2.

$$\text{WE} = \left(\frac{w_o - w_d}{w_o}\right) \times 100 \ [\%] \qquad (2)$$

Where:

W_o is the original width of the sample

W_d is the width after densification

Following densification, the boards were conditioned at 20°C, 65% RH for 4 wk. The board dimensions were measured again following conditioning.

Property Testing

Set-recovery is the extent to which the densified sample resists returning to its original dimensions. This was assessed in two ways, 1) by soaking in water, and 2) by exposure to high-humidity air (RH cycling).

From each board, two 20×20 mm blocks were cut side by side, each at least 5 mm from the board edges and 60 mm from the board end (Fig 1). One block from each pair was assessed via water soaking and one via RH cycling.

For the water-soaking test, the thickness of the blocks was measured in three places. Then, the blocks were oven-dried overnight at 103°C, and their thickness was measured again.

In the next step, the blocks were submerged in water at 20°C for 24 h, then oven-dried at 103°C for 24 h, and their thickness was measured again. The water soaking, oven drying, and subsequent thickness measurement were repeated for a further 4 cycles.

Set-recovery after water soaking is calculated as follows:

$$\text{SR}_{\text{WS}} = \left(\frac{t_{w\text{OD}} - t_{\text{OD}}}{t_o - t_{\text{OD}}}\right) \times 100 \ [\%] \qquad (3)$$
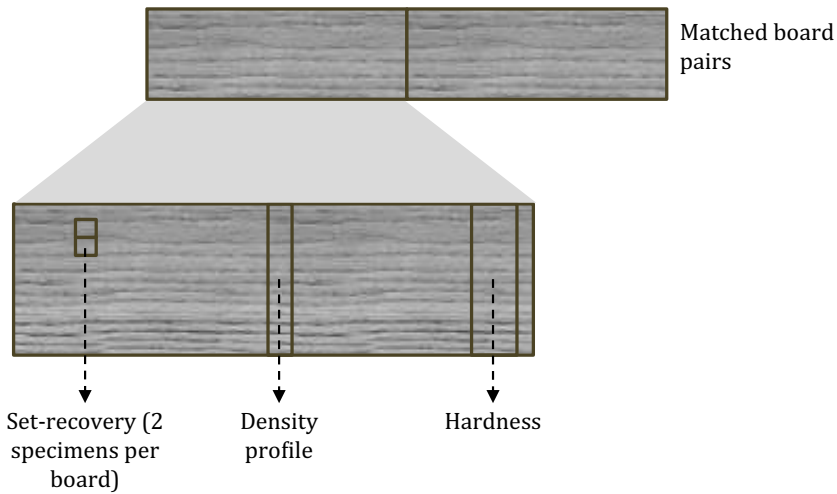
Figure 1.   A cutting plan showing the location of the property test specimens within each board. The view is of the upper face of the board.

Where:

t_o is the initial uncompressed thickness

t_{OD} is the oven-dried thickness following densification

t_{wOD} is the oven-dried thickness following water soaking

The RH cycling test was similar to the water soaking test, but instead of oven drying, the boards were conditioned at 25°C, 65% RH for 2 wk, and then, conditioned at 25°C, 85% RH for 2 wk, and their thickness was measured at the end of each conditioning period. After five conditioning cycles, the blocks were oven-dried, and their thickness was measured again.

Set-recovery after humidity cycling is calculated as follows:

$$SR_{RS} = \left(\frac{t_{85} - t_c}{t_o - t_c}\right) \times 100 \, [\%] \tag{4}$$

Where:

t_o is the initial uncompressed thickness

t_c is the thickness following densification and conditioning to 65% RH

t_{85} is the thickness after conditioning to 85% RH.

For hardness testing, 100×50 mm blocks were cut across the entire width of each board, starting around 5 mm from the board end (Fig 1). Because surface densification is primarily intended to change the properties of the wood surface and not necessarily the bulk of the wood sample, it is important to use a hardness test that does not penetrate too deeply into the sample (Scharf et al 2022). Here, a modified Brinell hardness test was used where a steel ball 11.28 mm in diameter was indented 4 mm into the surface of the sample and the applied load was recorded (Fig 2). Each tested sample was placed on a second board of the same material to minimize the effect of board thickness on the measured hardness. Some quarter-sawn bulk-densified boards split before the hardness testing was complete. For these boards, the applied load and indentation depth at the time of the break were recorded.

Brinell hardness (BHN) is calculated according to Eq 5.

$$BHN = \frac{2F}{\pi D \left(D - \sqrt{D^2 - d^2}\right)} \, [\text{kN/mm}^2] \tag{5}$$

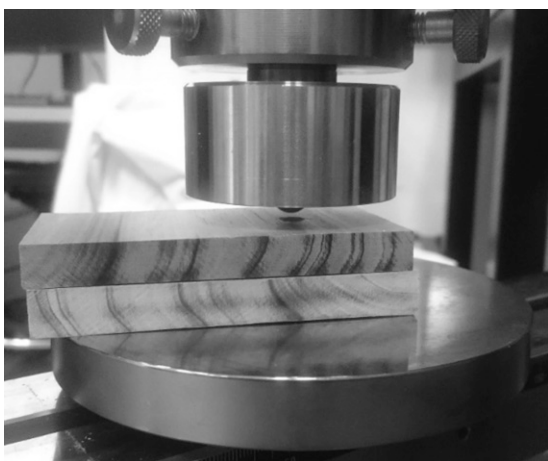Where:

F is the applied force (kN)

Figure 2.   Brinell hardness testing set up, showing the sample to be tested sitting on top of a second sample of the same species, grain orientation, and densification process (ie, surface- or bulk-densified).

D is the diameter of the ball (mm)

d is the maximum diameter of the indentation (mm)

The diameter of the indentation (*d*) was calculated as follows:

$$d = \sqrt{8h(D/2 - h/2)} \; [\text{mm}] \qquad (6)$$

Where:

h is the depth of the indentation (mm)

And *D* and *d* are as defined in Eq 5.

Density Profiles

Density measurements were made using the Scion DiscBot measurement system (Scion 2016). This consists of a range of measurement tools connected to an X-Y table to enable automated two-dimensional measurements of discs, cores, or small sections of boards.

A 25-mm-long sample was cut from near the center of each board (avoiding the end-most 50 mm of each end of the board, as shown in Fig 1) and these were equilibrated under standard conditions (25°C, 65% RH) until their weight stabilized. Prior to testing, the weight and dimensions of

each sample were recorded. These values were used to calculate a nominal gravimetric density for each sample, ie, the density of the wood plus associated moisture.

Prior to being measured in the DiscBot, each sample was fixed into a frame to ensure it was oriented correctly for the X-ray density measurement. Samples were oriented relative to their orientation in the hot press, namely, with the face compressed by the top platen facing in the same direction for every sample.

X-ray density measurements were taken using a polychromatic X-ray source (Spellman RB150 PN600X4009) with an output of 70 kV and 3 mA. The X-rays pass through the sample and are detected with a Hamamatsu Photonics model C9750-10F line camera. This measurement was repeated on a 0.4-mm grid over the entire surface of the sample. Density was calculated at the measurement pixel level from the X-ray intensity, plus an empirically derived mass attenuation coefficient (Eq 7). This was used to generate a two-dimensional map of nominal density values (converted to kg/m^3) on a 0.33 mm grid over the entire sample width and thickness.

$$\rho = \left(\frac{1}{\mu_m \, t}\right) \cdot \left(-\ln\left(\frac{I}{I_0}\right)\right) \; [\text{g/cm}^3] \qquad (7)$$

Where:

ρ is the specimen density (g/cm^3)

μ_m is the X-ray mass attenuation coefficient (0.2946 cm^2/g)

t is the specimen thickness (cm)

I is the X-ray intensity through the sample, minus the source-off signal

I_0 is the X-ray intensity through the air, minus the source-off signal

The nominal density values were adjusted using R software (R Core Team 2021). The samples were not always perfectly oriented to the X- and Y-axes of the DiscBot, so the samples were rotated when required, and a new coordinate system was applied so the board edges were parallel

to the X- and Y-axes. Linear interpolation was used to produce a new set of density values on a 0.5-mm grid using the new coordinate system. One-dimensional density profiles were produced by averaging the density values over the entire width (X-axis) for each point on the Y-axis, ie, at 0.5 mm spacing through the thickness of the original board.

For the densified samples, the one-dimensional density profiles were further characterized according to the metrics described by Zhou et al (2019), as reproduced in Fig 3. Briefly, the PD is the maximum density in the profile, and the peak density depth (PD_i) is the distance from the surface to the PD. For the surface densified samples, the thickness of the densified zone (DTh) was also quantified. This is defined as the thickness over which the density is greater than 80% of the PD.

For each combination of species, grain orientation, and densification process, an average (one-dimensional) density profile was produced by aligning all the samples with the equivalent of the top platen face and averaging the density values at each point through the wood thickness. Because the wood thickness does var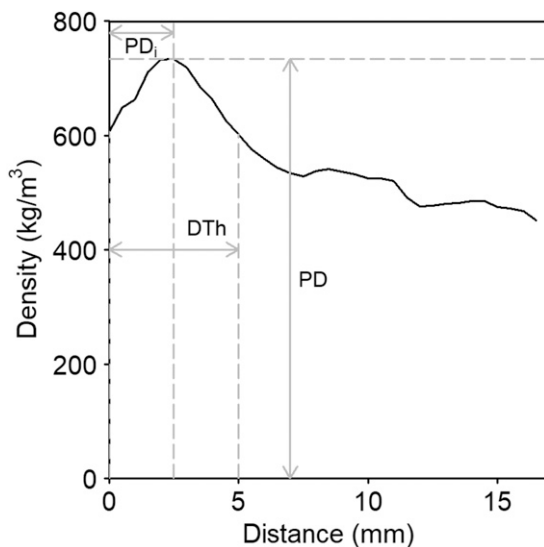y slightly between specimens, the thickness of each sample was normalized to the corresponding press gap (compressed thickness) for each species and densification process. This ensured consistent alignment of both the top and bottom surfaces across all the samples. For each densified sample, there is an equivalent undensified sample which was cut from the same board. The average density of each of these undensified samples was used to normalize the density of their equivalent densified boards, ie, each individual density value was divided by the average density of the equivalent undensified control sample.

Statistical Analysis

Because of the differences in target thickness, ie, the press gap between the two species, it was decided to analyze each species separately. Within each species, the data were initially assessed for normality and homogenous variances using Shapiro–Wilk and Levene's tests. Hardness, final density, and final MC were normally distributed. So a two-way ANOVA analysis was used to compare the means of the different densification processes and sawing orientations. Linear modeling was used to determine the significance of relationships between variables. All other variables were found to have significant variation from normality and homoscedasticity. Therefore, nonparametric test methods were used to assess the data. The Kruskal–Wallis test with Holm adjustment was used to determine significant differences between the densification processes and with different grain orientations.

RESULTS AND DISCUSSION

A summary of the board properties following THM densification is shown in Table 2. For both densification processes and for both grain orientations, the final thickness of the *E. fastigata* boards was, on average, significantly thicker than the press gap. The surface densified boards had a high percentage of spring-back (∼9-18% on average) which would contribute to the difference between the press gap, and the final board thickness. For *E. nitens*, the average final board thickness was not significantly different to the press

Figure 3. Metrics calculated to characterize the one-dimensional density profiles.

Table 2. Spring-back, width expansion, and final thickness for each species and sawing orientation. Prior to densification, the samples had an average width of 97 mm and an average thickness of 21 mm.

Species	Grain orientation	Densification type	Spring-back (%)	Width expansion (mm)	Final thickness (mm)
E. fastigata	Flat-sawn	Surface	17.7[a]	1.2[ab]	17.91[g]
E. fastigata	Quarter-sawn	Surface	9.1[ab]	1.0[b]	17.42[g]
E. fastigata	Flat-sawn	Bulk	3.5[b]	1.9[a]	16.34[g]
E. fastigata	Quarter-sawn	Bulk	6.4[ab]	1.5[ab]	16.36[g]
E. nitens	Flat-sawn	Surface	1.5[e]	1.6[e]	16.03
E. nitens	Quarter-sawn	Surface	2.9[e]	1.4[e]	16.13
E. nitens	Flat-sawn	Bulk	2.3[e]	4.9[f]	9.93
E. nitens	Quarter-sawn	Bulk	10.8[e]	3.6[f]	10.33

[a-f] Values followed by the same letters in superscript do not differ significantly from one another at alpha = 0.05.
[g] Final thickness is significantly different to press gap, ie, target final thickness.

gap for any of the grain orientations or densification processes. Spring-back can occur when elastic deformation in the wood cells is not adequately relieved before the press is opened. Low levels of spring-back are preferred, as this reduces thickness variation in the densified boards, and means that the energy put into compressing the boards is not lost when the press force is released. For *E. fastigata*, there were no substantial differences in width expansion between the different densification processes or sawing orientations. For *E. nitens*, the width expansion was significantly higher in the bulk densified boards compared with the surface densified, but there was no difference between sawing orientations. Lower width expansion is preferable, to avoid width variation in the densified boards.

Set-Recovery by Water Soaking

Set-recovery is a measure of how much the densified wood resists returning to its original undensified dimensions when the wood MC increases. A set-recovery of 0% means the board retains its densified dimensions, and a set-recovery of 100% means the board has reverted to its original undensified dimensions. The set-recovery resulting from repeated water soaking is shown in Fig 4. For both species, the surface-densified boards had a high set-recovery (average 75-85%), indicating the boards had regained over three-quarters of the reduction in thickness from densification. For *E. fastigata*, the bulk densified boards did not have a significantly different

set-recovery to the flat-sawn surface densified boards. For *E. nitens*, the bulk densified boards had significantly lower set-recovery, and there was no significant difference in set-recovery between the two grain orientations. The set-recovery of bulk densified *E. nitens* (average 40%) is somewhat higher than that found by Balasso et al (2020), who measured a set-recovery of 27.5% in densified *E. nitens* after a single water soaking cycle. However, the set-recovery values in this study are still much lower than those seen in other species. For example, Laine et al (2013) prepared bulk densified Scots pine which showed a set-recovery of 75% after 3 cycles of water soaking. In another attempt, Darwis et al (2017) bulk densified *Gmelina arborea* to various ratios (densification ratios from 0.125 to 0.375) and found that the set-recovery increased proportional to the densification ratio (from ∼60 to 80% set-recovery). The bulk-densified *E. nitens* had a higher densification ratio again (0.5), but much lower set-recovery. Despite the unusually low set-recovery for the bulk densified *E. nitens*, a 30-40% increase in thickness on contact with water is unlikely to be acceptable in service, since set-recovery would need to be eliminated for a commercially viable product. As shown by Darwis et al (2017), thermal modification can reduce the set-recovery. In their work, heat treatment at 180°C for 5 h reduced the set-recovery by more than half. Thermal modification could be considered here as a way to reduce the set-recovery of either bulk
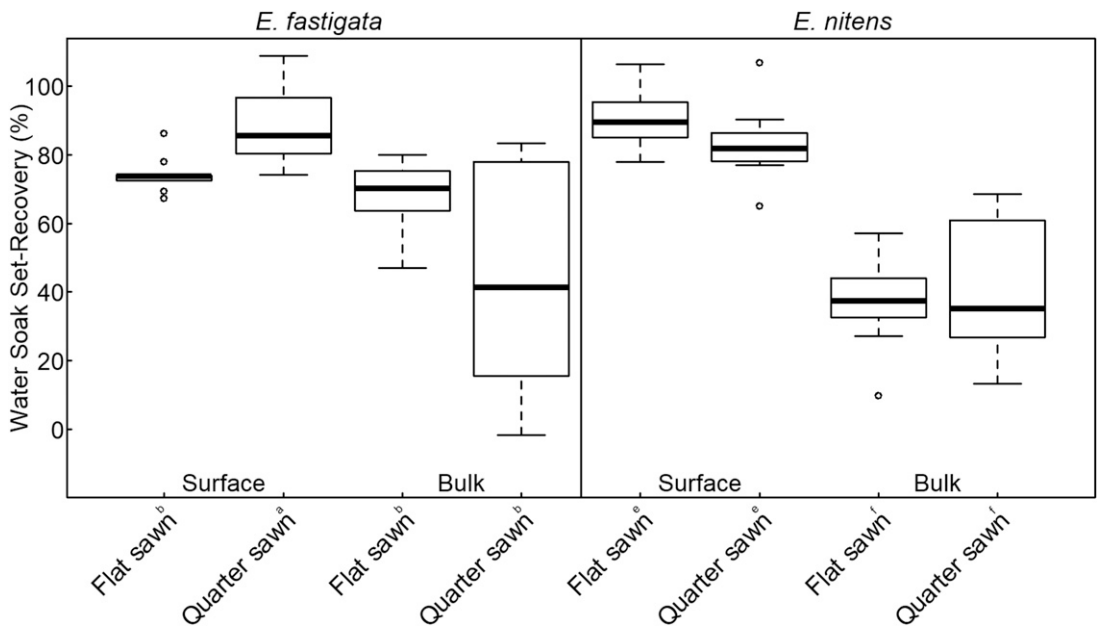
Figure 4.   Set-recovery by densification type, species, and grain orientation. Superscript letters indicate treatments within each species that are not significantly different from each other (95% confidence level, Kruskal-Wallis test with Holm adjustment).

densified or surface densified wood, potentially to an acceptably low level.

Set-Recovery by RH Cycling

As noted by Laine et al (2013), the water soaking test is a harsh test, especially for products such as flooring that are used indoors, which would generally be coated before use and are unlikely to become water saturated. As an alternative method of assessing set-recovery, the set-recovery after five cycles of alternating high and low RH was assessed. The obtained results are shown in Fig 5. The values of set-recovery were much lower than those obtained for the water soaking test but show similar trends. For *E. nitens*, the set-recovery was lower for the bulk densification compared with that of the surface densification, and there were no significant differences between the different grain orientations. The trend for *E. fastigata* was similar, with higher set-recovery for the surface densification compared with the bulk densification, but with significant differences between the two grain orientations for each densification process. These results also showed that the RH

cycling set-recovery of densified *E. nitens* is less than that of *E. fastigata* for all tested samples (Fig 5). The causes of this difference in set recovery between species are not known.

The EMC at 25°C, 65% RH following five humidity cycles is shown in Table 3. For both species, the EMC (EMC) reduced significantly with increasing degree of densification. Lower EMC can correspond to increased dimensional stability (Navi and Sandberg 2012c), implying that a significant reduction in EMC is a positive result. These results also show that grain orientation did not have a significant effect on EMC.

Density Profiles

The average PD, and PD_i are shown in Table 4. For the surface densified boards, the DTh is also shown. For the *E. fastigata* boards, there is no significant difference in PD between the different densification processes and no significant differences in the PD_i values obtained for different samples. However, for *E. nitens*, the bulk densified boards have a higher PD than those of the
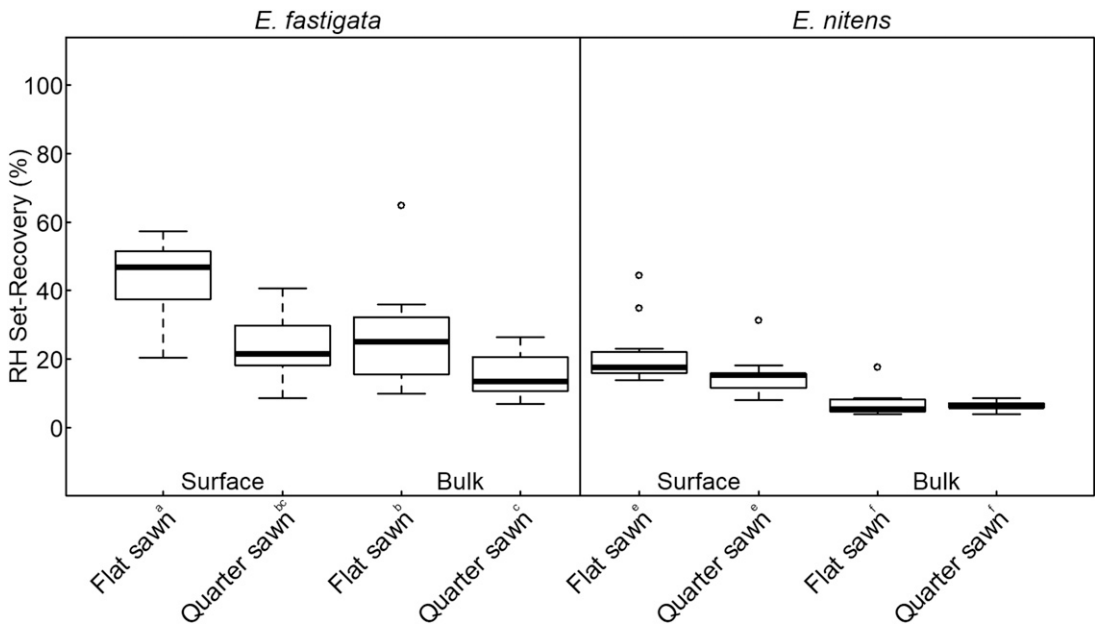
Figure 5. RH-cycling set-recovery by densification type, species, and grain orientation. Superscript letters indicate treatments within each species that are not significantly different from each other (95% confidence level, Kruskal-Wallis test with Holm adjustment).

surface densified boards, and the quarter-sawn surface densified boards have a higher PD than those of their flat-sawn equivalents. For the flat-sawn surface densified boards, the PD is significantly deeper into the board compared with the equivalent quarter-sawn boards and compared with the bulk densified boards (both sawing orientations), as indicated by measured PD_i values (Table 4). These results also revealed that, the DTh value of flat-sawn boards is larger than that of quarter-sawn boards when a surface densification is implemented for *E. fastigata*. The difference between the two grain orientations was not significant for *E. nitens* (Table 4).

Table 3. Nominal density following densification and conditioning, hardness and EMC (EMC) for each densification process, and undensified controls.

Species	Grain orientation	Densification type	Nominal density (kg/m³)	Brinell hardness (kN/mm²)	EMC (%)
E. fastigata	Flat-sawn	Control	712[cd]	26.6[bc]	12.8[ab]
E. fastigata	Quarter-sawn	Control	680[d]	20.7[c]	13.2[a]
E. fastigata	Flat-sawn	Surface	806[ab]	37.5[a]	12.4[bc]
E. fastigata	Quarter-sawn	Surface	734[bc]	31.1[ab]	12.1[c]
E. fastigata	Flat-sawn	Bulk	861[a]	37.3[a]	11.5[d]
E. fastigata	Quarter-sawn	Bulk	779[abc]	28.3[abc]	10.9[d]
E. nitens	Flat-sawn	Control	490[e]	15.0[e]	12.4[ef]
E. nitens	Quarter-sawn	Control	510[e]	15.7[e]	12.6[e]
E. nitens	Flat-sawn	Surface	582[f]	22.2[f]	11.6[fg]
E. nitens	Quarter-sawn	Surface	642[f]	31.4[fg]	11.5[g]
E. nitens	Flat-sawn	Bulk	916[g]	31.7[g]	10.3[h]
E. nitens	Quarter-sawn	Bulk	938[g]	34.7[g]	10.6[h]

[a-h] Superscript letters indicate treatment groups (within each species) that are not significantly different from each other (95% confidence level, Tukey's HSD test).

Table 4. Peak density (PD), Peak density depth (PD_i), and thickness of the densified region (DTH) for each species, densification process, and orientation.

Species	Densification process	Grain orientation	PD (kg/m^3)	PD_i (mm)	DTh (mm)
E. fastigata	Surface	Flat-sawn	886[a]	2.1[a]	4.0[a]
E. fastigata	Surface	Quarter-sawn	899[a]	0.8[a]	2.0[b]
E. fastigata	Bulk	Flat-sawn	898[a]	1.2[a]	—
E. fastigata	Bulk	Quarter-sawn	844[a]	0.5[a]	—
E. nitens	Surface	Flat-sawn	770[g]	1.4[e]	2.4[e]
E. nitens	Surface	Quarter-sawn	870[f]	0.3[f]	1.7[e]
E. nitens	Bulk	Flat-sawn	935[e]	0.4[f]	—
E. nitens	Bulk	Quarter-sawn	972[e]	0.2[f]	—

[a-f] Values followed by the same letters in superscript do not differ significantly from one another at alpha = 0.05.

The average one-dimensional density profile for each species, densification process, and grain orientation are shown in Fig 6. For the *E. fastigata* boards, the overall increase in density is small, with peak densities being around 1.3 times higher than the density prior to densification (Fig 6[a]). The density at the densified surface of the surface densified boards is similar to that of the outer surfaces of the bulk densified boards, while the undensified surface has a similar density to the undensified boards. This is a good result, as the surface densification process aims to produce a hard densified surface on one face of the board, without unduly compressing the remainder of the board thickness. The flat-sawn bulk densified boards showed a flatter density profile across the board thickness compared with the quarter-sawn boards, which have a central area with a density similar to the density prior to densification (Fig 6[a]).

The *E. nitens* boards presented a considerably larger increase in density compared with the undensified controls. (Fig 6[b]), due to the higher densification ratio used on this species. The bulk densified samples showed similar density profiles to the bulk densified *E. fastigata*, but with the average density being around 1.8-1.9 times higher than the density prior to densification. The surface-densified *E. nitens* has a slightly lower PD than the bulk-densified *E. nitens*. The quarter-sawn
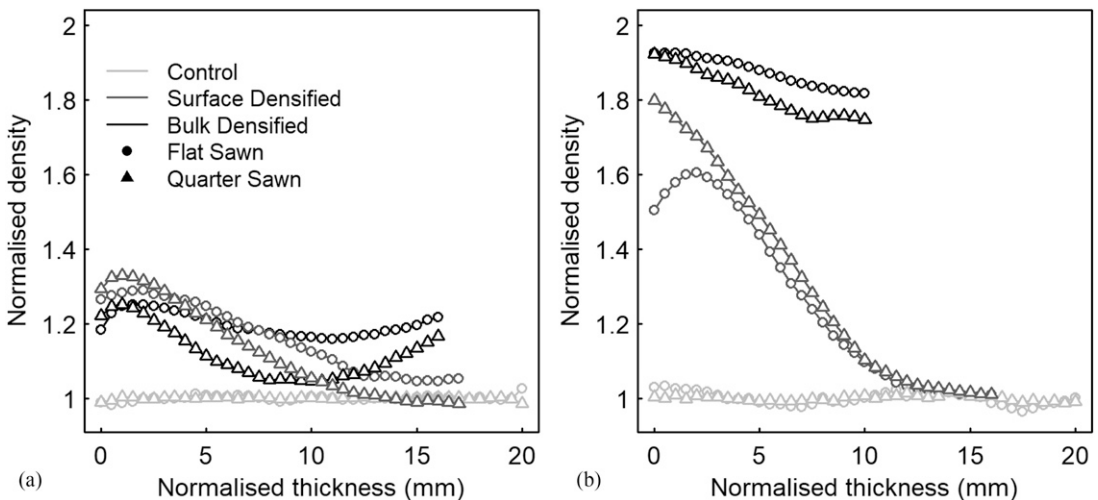

Figure 6.   Average density profiles for *E. Fastigata* (a) and *E. Nitens* (b). The normalized density is based on the pretest density of each board. The normalized thickness is based on the target thickness for each densification process.

surface-densified *E. nitens* has a density peak at the board surface, which provides the largest increase in surface density for a given densification ratio, which is the primary aim of the surface densification process. In contrast, the flat-sawn boards had a PD that was slightly below the wood surface (Fig 6[b]). As with *E. fastigata*, the undensified face of the surface-densified *E. nitens* had a similar density to the undensified controls.

Hardness and Bulk Density

The gravimetric (nominal) density of the densified samples and undensified controls are shown in Table 3. It should be noted that this is the density of the wood, plus associated moisture under standard conditions (25°C, 65% RH). Because the EMC of the wood is lower following the densification process (Table 3), this will alter the relationship between the nominal density and the oven-dry density for the densified samples. It is likely that the nominal density values reported here under-report the increase in oven-dry density of the bulk densified boards by a small amount (1-3%). For *E. nitens,* surface densification increased the density significantly compared with the undensified controls, and the bulk densification increased it further. No significant differences in final density were seen between sawing orientations. For *E. fastigata*, the differences in density were smaller, and there were not such clear-cut differences between the two densification processes. Additionally, for the bulk densified samples, the flat-sawn boards had a significantly higher density than the quarter-sawn boards. Balasso et al (2020) densified *E. nitens* to a target densification ratio of 0.39, which is somewhat less compression than the bulk densification in this study, however, their average final density ($800 \pm 9 \, kg/m^3$) was similar to the bulk densification in this study ($837 \pm 44 \, kg/m^3$). The undensified *E. fastigata* showed a higher density than the undensified *E. nitens*, which gives some explanation as to why the *E. nitens* boards could be densified to a greater degree without sustaining damage. For each species, the bulk densified boards were densified to the greatest extent possible

without damaging the wood, and for *E. nitens*, this resulted in a substantially higher final density than the *E. fastigata* boards, despite starting from a lower initial density. All things being equal, you would expect both species to reach a similar density before damage to the wood occurred. This suggests there are additional, unknown factors that make *E. nitens* more suitable for densification than *E. fastigata*, eg, wood structure or chemistry.

For the *E. nitens* boards, both surface and bulk densification significantly increased the wood hardness compared with the controls, and there were no significant differences in hardness between the two grain orientations. For *E. fastigata*, the flat-sawn surface- and bulk-densified samples had significantly higher hardness values than the undensified controls, but these differences were not significant for the quarter-sawn samples. For both species and for both densification processes, there were no significant differences in hardness between samples with different grain orientations.
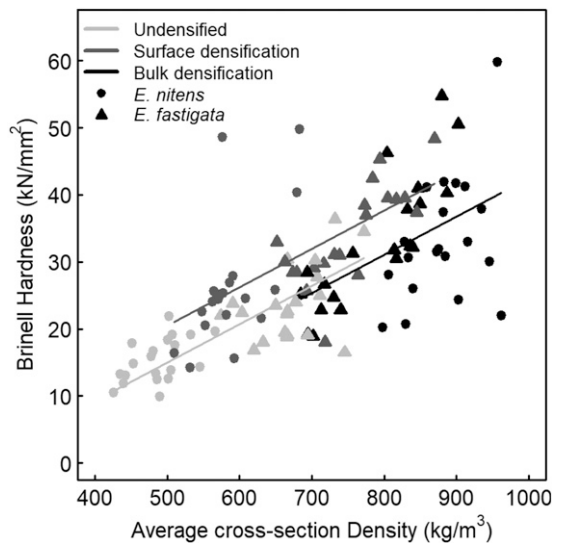

Figure 7.   Relationship between final density and Brinell hardness for each species and densification type. *E. Fastigata* is shown by triangles, *E. Nitens* by circles. The best fit lines show a correlation between density and hardness, taking the densification process into account. Adjusted $R^2 = 0.586$, $p < 0.001$.

Wood properties such as hardness are generally correlated with density. Linear regression was used to investigate the relationship between average cross-sectional density and Brinell hardness, after taking species, densification process, and grain orientation into account. The effects of species and grain orientation were not significant ($p = 0.73$ and $p = 0.64$, respectively). The relationship between hardness and density was significant ($p < 0.001$), and for a given density, surface-modified boards had on average, a Brinell hardness of $5.6\,kN/m^2$, higher than both the undensified boards and the bulk-densified boards. Individual board values and fitted lines for each densification treatment are shown in Fig 7.

CONCLUSIONS

E. nitens was able to be densified to a greater degree without sustaining damage than was observed for *E. fastigata* (maximum densification ratios of 0.5 and 0.2, respectively). This resulted in larger increases in density and surface hardness in the *E. nitens* boards (100-120% increase in surface hardness for *E. nitens* compared with 40-50% in *E. fastigata*).

The set-recovery following water soaking was surprisingly low in the bulk densified *E. nitens* boards (average 40%), whereas the *E. fastigata* and the surface densified *E. nitens* had higher set-recoveries (average 55-85%) which is more in line with values from other species seen in the literature.

Despite the bulk densified *E. nitens* having an unusually low set-recovery, this level of irreversible swelling is still unlikely to be acceptable in service, so an additional treatment, such as thermal modification, would be required to reduce the set-recovery further. Set-recovery following humidity cycling was lower than that following water soaking (averages from 7 to 32%), but it followed a similar trend with bulk densified *E. nitens* showing the lowest set-recovery in this study. It would be worth investigating ways of further reducing the set-recovery in *E. nitens* to see if it can be eliminated.

Density profiles showed that the PD for each sample was generally within 1-2 mm of the wood surface and was often right on the surface. Having a density peak close to the wood surface is beneficial because it results in the maximum increase in surface hardness for a given densification ratio, but allowances must be made for some of the surface material to be removed during final finishing, eg, sanding.

The relationship between surface hardness and average board density was independent of species and grain orientation for the tested samples. For a given density, surface densified boards had a higher surface hardness than undensified and bulk densified boards, which were not significantly different to each other.

In contrast with many softwood species, eucalypts are typically quarter-sawn, both for appearance and to reduce the incidence of drying degrade. Overall, there were minimal differences in performance between quarter-sawn and flat-sawn boards following densification in this study. In some cases, set-recovery and depth of PD, quarter-sawn boards performed slightly better than flat-sawn boards. This is a positive result for eucalypts, as the densification process could be incorporated with existing sawing and processing methods that produce quarter-sawn timber, and consequently, new applications of their use could be applied.

REFERENCES

Balasso M, Kutnar A, Niemelä EP, Mikuljan M, Nolan G, Kotlarewski N, Hunt M, Jacobs A, O'Reilly-Wapstra J (2020) Wood properties characterisation of thermo-hydro mechanical treated plantation and native Tasmanian timber species. Forests 11:1-15.

Darwis A, Wahyudi I, Dwianto W, Cahyono TD (2017) Densified wood anatomical structure and the effect of heat treatment on the recovery of set. J Ind Acad Wood Sci 14:24-31.

Fu Q, Cloutier A, Laghdir A (2017) Effects of heat and steam on the mechanical properties and dimensional stability of thermo-hygromechanically-densified sugar maple wood. BioResour 12:9212-9226.

Jones TG, McConnochie RM, Shelbourne T, Low CB (2010) Sawing and grade recovery of 25-year-old *Eucalyptus fastigata, E. globoidea, E. muelleriana* and *E. pilularis.* N Z J For Sci 40:19-31.

Koumba G, Chavez R, Bustos C, Cloutier A, Stevanovic T (2014) Chemical changes induced in *Pinus radiata* and *Eucalyptus nitens* following the densification process. J Sci Technol For Prod Process 4:20-22.

Kutnar A, Kamke FA (2012) Influence of temperature and steam environment on set recovery of compressive deformation of wood. Wood Sci Technol 46:953-964.

Kutnar A, Sandberg D, Haller P (2015) Compressed and moulded wood from processing to products: COST action FP0904 2010-2014: Thermo-hydro-mechanical wood behaviour and processing. Holzforschung 69: 885-897.

Kutnar A, Sernek M (2007) Densification of wood. Zbornik gozdarstva in lesarstva 82:53-62.

Laine K, Belt T, Rautkari L, Ramsay J, Hill CAS, Hughes M (2013) Measuring the thickness swelling and set-recovery of densified and thermally modified Scots pine solid wood. J Mater Sci 48:8530-8538.

Laine K, Segerholm K, Wålinder M, Rautkari L, Hughes M (2016) Wood densification and thermal modification: Hardness, set-recovery and micromorphology. Wood Sci Technol 50:883-894.

Lenth CA, Kamke FA (2001a) Moisture dependent softening behavior of wood. Wood Fiber Sci 33:492-507.

Lenth CA, Kamke FA (2001b) Equilibrium moisture content of wood in high-temperature pressurized environments. Wood Fiber Sci 33:104-118.

Navi P, Sandberg D (2012a) Wood densification and fixation of the compression-set by THM treatment. Pages 193-224 *in* Thermo-hydro-mechanical processing of wood. EPFL Press, Lausanne, Switzerland.

Navi P, Sandberg D (2012b) Surface densification. Pages 241-248 *in* Thermo-hydro-mechanical processing of wood. EPFL Press, Lausanne, Switzerland.

Navi P, Sandberg D (2012c) Heat treatment. Pages 249-286 *in* Thermo-hydro-mechanical processing of wood. EPFL Press, Lausanne, Switzerland.

R Core Team (2021) R: A language and environment for statistical computing. R Foundation for Statistical Computing, Vienna, Austria.

Rautkari L, Laine K, Laflin N, Hughes M (2011) Surface modification of Scots pine: The effect of process parameters on the through thickness density profile. J Mater Sci 46:4780-4786.

Scharf A, Neyses B, Sandberg D (2022) Hardness of surface-densified wood. Part 1: Material or product property? Holzforschung 76:503-514.

Scion (2016) DiscBot—automated wood properties scanning. https://www.youtube.com/watch?v=KVv8_GVXQbU (24 April 2023).

Wang JY, Cooper PA (2005) Effect of grain orientation and surface wetting on vertical density profiles of thermally compressed fir and spruce. Holz Roh Werkst 63: 397-402.

Zhou Q, Chen C, Tu D, Zhu Z, Li K (2019) Surface densification of poplar solid wood: Effects of the process parameters on the density profile and hardness. BioResour 14: 4814-4831.

IMAGE ANALYSIS TO ASSESS WOOD VARIABILITY IN LONGLEAF PINE CROSS-SECTIONAL DISKS

Sameen Raut*

PhD Candidate
E-mail: sameen.raut@uga.edu

Joseph Dahlen[†]

Associate Professor
Warnell School of Forestry and Natural Resources
University of Georgia
Athens, GA 30602-2152
E-mail: jdahlen@uga.edu

Abstract. Image analysis is an important method for rapidly measuring wood property variation, but it is infrequently applied to disks collected from forestry studies. The objective of this study was to compare image-estimated wood and bark volumes and diameters to reference measurements, and to extract more information from the images including the shape (out-of-round index, eccentric pith) and the amount and location of severe compression wood. A total of 1120 disks were cut from multiple height levels of 48 defect-free and 56 defect-containing (forking, excessive sweep, and ramicorn branching) longleaf pine (*Pinus palustris*) trees from 16 stands across Georgia (U.S.). Disks were machined on one transverse surface using a computer numeric controlled router to prepare a clean surface for imaging. Three images, one under white light, the second under blue light, and the third under blue light with a green longpass filter, were taken for each disk. Volumes and diameters estimated from images were in close agreement with reference methods. Linear models fitted as measured vs image volumes for wood and bark had coefficient of determination (R^2) values of >0.99 and 0.96. Linear models fitted as measured vs image diameters had R^2 values of >0.99. Out-of-round index and pith eccentricity values calculated from images showed a moderate positive correlation ($R = 0.43$). Algorithms developed were able to correctly identify severe compression wood, but not mild-to-moderate compression wood. Severe compression wood was moderately correlated to out-of-round index ($R = 0.54$) and pith eccentricity ($R = 0.48$). More than 98% of the disks having severe compression wood came from defect-containing trees.

Keywords: Compression wood, nondestructive evaluation, taper, wood and bark volume, wood imaging, wood and fiber quality.

INTRODUCTION

Wood is a natural heterogeneous material with properties that exhibit significant variability (Zobel and van Buijtenen 1989; Thumm et al 2010). Within a species, variability exists within annual rings, between annual rings, within trees due to changes in cardinal direction and height, between trees, between stands, and between different growing regions (Panshin and de Zeeuw 1980; Megraw 1985; Burdon et al 2004; Jordan et al 2008; Auty et al 2013, 2014; Eberhardt et al 2018). To measure variability in wood and fiber properties, typically cores are collected from trees, or disks are destructively sampled from different heights after felling (Zobel and van Buijtenen 1989; Eberhardt et al 2018). Disks are typically either processed "whole" to collect wood and bark specific gravity (SG) (density divided by the density of water) and MC, or further cut into pith-to-bark strips to provide information on radial variation (Dahlen et al 2018; Eberhardt et al 2018; Schimleck et al 2019).

Disks or bolts from felled trees can be used to assess changes in diameter from the stump (tree bottom) to the tip (tree top) to measure the stem taper (Burkhart and Tomé 2012). Outside bark diameter is typically measured using a diameter

---

* Corresponding author
† SWST member

tape, the inside bark diameter can be estimated using a bark gauge, or averaging two diameter measurements after felling, or from using a diameter tape following careful bark removal (Eberhardt et al 2017). These diameter measurements typically assume that the shape is circular, with tree shape evaluated qualitatively; however, research on quantitative assessment is advancing through the use of LiDAR or photogrammetric point clouds (Morgan et al 2022). In reality, disk shapes are variable, and the pith is not centered along the entire length of a tree. A major cause for eccentric radial growth is due to the formation of reaction wood, and in gymnosperms, it is termed compression wood (Timell 1986). Compression wood is generally darker in color than normal earlywood but lighter than normal latewood, and it has a high microfibril angle, high longitudinal shrinkage, high lignin content, and low cellulose content, which makes it unsuitable for lumber production and undesirable for pulp and paper (Timell 1986; Rune and Warensjö 2002).

Nondestructive evaluation of wood is increasingly being used in forestry and forest products research, operations, and manufacturing (Ross and Pellerin 1994; Ross 2015; Schimleck et al 2019). Imaging is one of many nondestructive evaluation tools which has seen extensive use (Evans 1994; Evans et al 1999; Bucur 2003a, 2003b; Decellee et al 2019; Wright et al 2019). For example, a major industrial application of imaging is in lumber manufacturing facilities, where the shape and volume of logs is measured using high-resolution laser scanners after debarking (Thomas and Bennett 2014; Sauter et al 2019). Lumber can be graded using single-pass X-ray scanners (Schajer 2001; Oh et al 2008, 2009), via the quantification of knots using the "tracheid effect", where a camera detects the returned orientation of a series of laser beams projected onto wood (Nyström 2003; Roblot et al 2010; Habite et al 2020), or using artificial intelligence (Lopes et al 2020; Hwang et al 2021; Kodytek et al 2022). Research instruments using imaging are numerous, but specific to wood and fiber quality research is the SilviScan suite of instruments that measure cell dimensions, microfibril angle, and wood density (Evans 1994; Evans

et al 1999; Schimleck et al 2019). Comparatively, there are a limited number of studies conducted that describe imaging work done on whole-disks; however, this is changing due to technological advancements. In this regard, Pont et al (2007) working with radiata pine (*Pinus radiata*) disks using red-green-blue (RGB) images, delineated annual rings and detected areas of compression wood, and then created a three-dimensional (3D) stem model showing varying levels of compression wood. Thumm et al (2010) developed partial least squares regression models for near IR hyperspectral imaging data collected from radiata pine cross-sectional disks to predict and visualize variation in lignin, galactose, and glucose content. Riddell et al (2012) deployed flatbed scanning of radiata pine disks (25-35-mm thick) using transmitted light to measure spiral grain angles. Thomas and Collings (2015) used circular polarized light to enable 3D visualization of compression wood and spiral grain in microtome-cut radiata pine transverse sections. Lerm et al (2017) constructed a mobile in-field RGB imaging system and imaged cross-cut sections of *Pinus patula* logs to construct 3D models showing resin pockets, pith location, branch structure, and log shape. The DiscBot system developed by Scion was designed to measure wood property variation both radially and in circumference (Schimleck et al 2019). Raatevaara et al (2020) used RGB images of the end faces of Norway spruce (*Picea abies*) logs to extract out-of-roundness and pith eccentricity data which they combined with stem taper data to predict maximum bow height.

To calculate whole-disk SG of wood or bark, green volume is typically measured using water displacement because of the nonuniform disk shape (ASTM 2017). Imaging presents an opportunity to not only replicate the volume measurements needed for SG calculation but to further extract information from disks particularly if the surface quality is improved prior to imaging. These additional measurements could include assessments of disk shape, including how much a disk is out of round and how far the pith is from the geometric center of the disk; and the quantity and location of compression wood. An important

Table 1. Summary of the diameter outside bark (DOB) and diameter inside bark (DIB) for all the longleaf pine cross-sectional disks used in this study.

Site type	Property	Defect-free					Defects				
		N	Mean	SD	Min	Max	N	Mean	SD	Min	Max
Cutover	DOB (cm)	268	13.8	5.0	6.3	30.9	251	13.2	4.5	6.3	23.6
(**N = 519**)	DIB (cm)		12.2	4.5	5.6	28.2		11.6	3.9	5.6	20.8
Old field	DOB (cm)	277	15.5	5.8	6.6	32.5	324	14.4	5.0	6.3	27.7
(**N = 601**)	DIB (cm)		14.0	5.2	5.8	29.7		12.9	4.5	5.3	23.9
Overall	DOB (cm)	545	14.6	5.5	6.3	32.5	575	13.9	4.8	6.3	27.7
(**N = 1120**)	DIB (cm)		13.1	4.9	5.6	29.7		12.3	4.3	5.3	23.9

advantage of imaging is being able to store a digital record of the samples, as it is not typically feasible to store disks well beyond the conclusion of a study due to space considerations. Opportunities to match images with reconstructed models, to show within-tree variation with images, or even determine outliers in data due to input errors, etc. are possible with images. Hence, the objective of this study was to compare wood and bark volume information and inside and outside bark diameters with reference measurements. Additional objectives were to use the images to measure shape information including how out of round the disks are along with the pith eccentricity, and to estimate the quantity of compression wood. Images of green longleaf pine (*Pinus palustris*) disks above the FSP without any drying were collected to save measurement time and reduce cracking that occurs during the drying of disks.

MATERIALS AND METHODS

Tree Selection and Disk Extraction

Samples used for this study were collected from 16 stands of planted, unthinned longleaf pine trees throughout southern Georgia (U.S.). Stands sampled were from either cutover forest sites (where the previous rotation was trees; most likely southern pine species) or old agricultural fields (the prior rotation was not a tree species) (Hainds 2004; Johnson and Gjerstad 2006; Kush et al 2006), with eight stands sampled per site type. Stands ages ranged from 12 to 25 yr. Trees were classified as defect-free (no visible stem defects), or defect-containing (herein referred to as defect trees) ie fork, excessive sweep, or ramicorn

branching present. From each stand, 20 trees were felled, with up to six defect trees sampled based on the frequency of defect trees within each stand (Raut et al 2022). From each stand, a subsample representing all of the defect trees sampled, and three defect-free trees representing a suppressed (small), codominant (medium), and dominant (large) tree were selected and used for the study for a total of 104 trees.

Cross-sectional disks (approximate thickness of 50 mm) were cut from the trees at fixed intervals: 0.15, 0.6, 1.37, and 2.44 m, and from there every 1.22 m along the tree up to the point, where the outside bark diameter was 76 mm. From the forked trees, disks were extracted from the same fixed height intervals up to the fork base before the bifurcation, from each of the fork bases after the bifurcation, and then from the height of the forks, where the outside bark diameter was 76 mm. A total of 1120 cross-sectional disks were examined, with 56 defect trees (575 disks) and 48 defect-free trees (545 disks) (Table 1). The disks were labeled, placed in plastic bags, sealed, and transported from the field to a freezer in the Wood and Fiber Quality lab at the University of Georgia, where they were kept frozen until further processing.

Disk Surfacing and Imaging

The disks were removed from the freezer and thawed for 48 h after which they were removed from their plastic bags. A three-axis computer numerical controlled (CNC) router (Fine Line Automation, Lebanon, PA) was used for machining one surface of the disks (Fig 1). The CNC

Figure 1. The three-axis computer numerical controlled (CNC) router preparing a cross-sectional disk surface for imaging.

router was controlled using an Arduino microcontroller (Arduino AG, Somerville, MA) with stepper motors used for linear motion. Since the disks were cut in the field using a chainsaw, the disk thickness varied. An ultrasonic distance sensor (Micro Detectors UK6, Modena, Italy) mounted on the y-axis of the CNC router was used to measure the thickness and the diameter of the disks. The disks were held on the router bed using a mechanical restraint. The router cut depth and cutting path was adjusted based on the disk thickness and diameter. The cutting bit used was an Amana Tool RC-2257 surface planer (Newton, IA). The router cut two passes on each disk, the first pass alternated the cut direction from left to right using the y-axis, where the router took approximately 6.4 mm off the surface of the disk (z-axis) in 28 mm passes (x-axis). The second pass skimmed the disk with 0.3 mm cut depth (z-axis) in 60.5 mm passes (x-axis). Cutting was from left to right for the second pass, and after each pass, the router returned to the left position of the y-axis before moving up on the x-axis. The second pass improved the surface for imaging (Fig 2).

Following surface preparation, images of the disks were taken using a custom-built setup with a white background and controlled using an Arduino microcontroller which interfaced with a computer running Python (Python Software Foundation, https://www.python.org/). Communication between the Arduino and Python was done using serial commands. The camera used was an Allied Vision Manta G-1236 with a 12.4-megapixel sensor (Stadtroda, Germany) and a 12 mm lens (f/2.8) (Computar, Cary, NC). The camera control was done using the Pymba library (https://github.com/morefigs/pymba). Prior to imaging, disk thickness was read by an ultrasonic sensor (Micro Detectors UK6). A linear translation stage with a stepper motor (step size = 0.0254 mm) moved the top surface of the disk to 600 mm from the camera based on the disk thickness reading from the ultrasonic sensor. Thus, each disk was imaged with a fixed focal length from the camera

Figure 2. The left image shows the typical surface quality of a chainsaw-cut wood disk; the right image shows the same disk after surface preparation (background removed from both images).

to ensure accurate calculation of diameter and area measurements.

It was found that different steps in image processing were best achieved when the disks were lit using different sources. As such, lighting for the disks was done using two LED strip light sources; white light with 4000K color temperature, and blue light (475 nm) (Super Bright LEDs Inc., St. Louis, MO). One challenge in working with images that contain both wood and bark was isolating the bark from the wood. During initial tests that were focused on using fluorescence imaging techniques with the blue LEDs and a 50-mm diameter green longpass filter (>525 nm) (Edmund Optics, Barrington, NJ) to detect compression wood (Thomas 2014), it was observed

that the fluorescence image had clear separation between the bark and the wood. A total of three RGB images were taken for each machined disk. The first image was taken using white light with 12.5 ms exposure time (herein referred to as the white image). The second image was taken using blue light with 80 ms exposure time (herein referred to as the blue image). The third image was taken under blue light with 500 ms exposure time with the longpass filter moved in front of the lens using a stepper motor (herein referred to as the filter image). The three images for one disk are shown in Fig 3(a), note that the paint used to mark the location on the tree to cut disks fluoresces and appears bright orange in the filter image (this was not intended and discovered after field sampling). Images were saved with each color

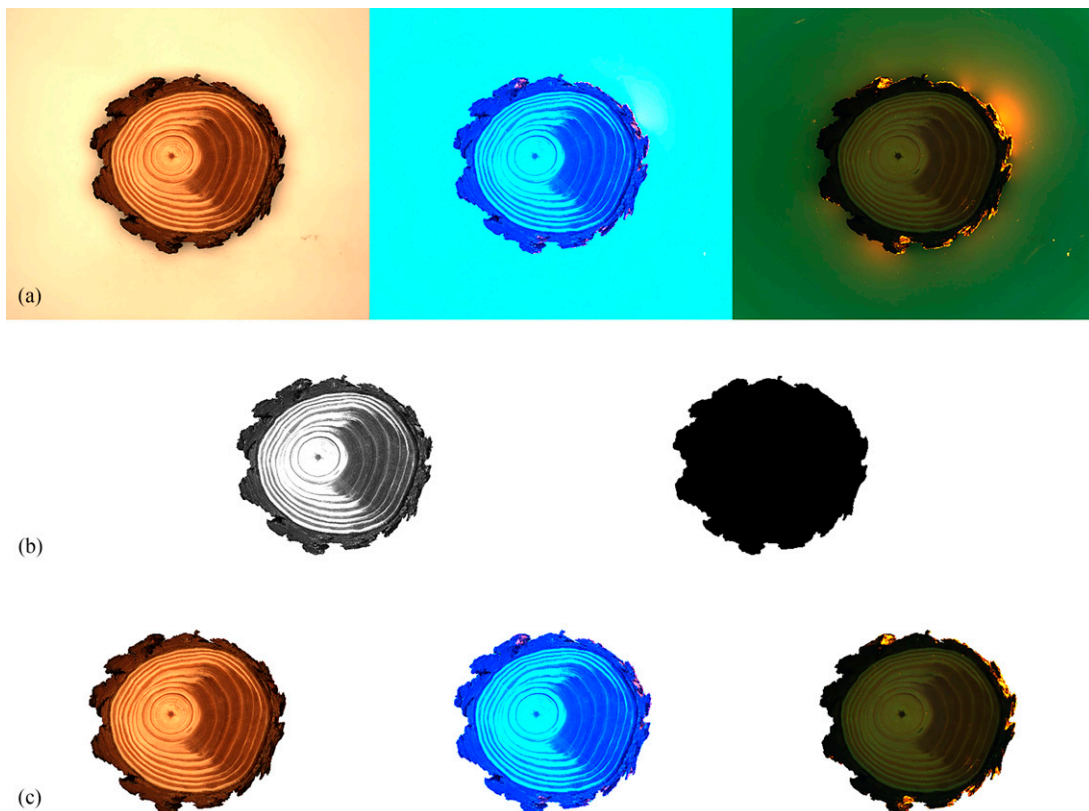Figure 3.   (a) A set of three images taken for a machined disk having a diameter outside bark (DOB) of 17.3 cm. Left: white image; middle: blue image; right: filter image. (b) Image showing the green channel of the blue image (left) and an image of the whole-disk mask (right). (c) White (left), blue (middle), and filter (right) images after the whole-disk mask was applied to the original images.

channel having an 8-bit depth, so pixel values ranged from 0 to 255 for each channel.

Disk Measurements

Following imaging, the outside bark diameters were measured to the nearest 0.1 cm with a diameter tape, and the disks were weighed to the nearest 0.01 g on a digital scale. The bark from the disks was peeled off, inside bark diameters measured, and the disks weighed again. The total bark weight for each disk was calculated from the difference in weight with and without bark. The largest piece of bark from each disk, and the peeled disks were used for volume measurement where they were labeled and submerged in water for 48-72 h. Following submerging, the bark pieces and the peeled disks were measured (separately) for their green volume to the nearest 0.01 cm^3 using water displacement (ASTM 2017). The green volume of the bark piece was then extrapolated to the total bark green volume using the total bark weight for each disk.

Image Processing

Image processing was done in Python version 3.7 (Python Software Foundation, https://www.python.org/) on the Spyder interface (Raybaut 2009) using the libraries OpenCV (Bradski 2000), NumPy (Harris et al 2020), and pandas (McKinney 2010). The camera was calibrated using various objects of known sizes and the lens was checked for distortion using OpenCV (Bradski 2000). Each pixel represented a length of 0.167 mm and an area of 0.0280 mm^2.

Background isolation. The first step in image processing was to isolate the background from the wood and the bark. The green channel of the blue image was used because the background was uniformly bright (pixel value = 255), whereas the wood and bark were darker (Fig 3[b], image on the left). A mask of the background was created by thresholding the image with any pixel less than 255 being converted to 0 (wood and bark), and any pixel equal to 255 as white (background) (Fig 3[b], image on the right). The mask from

each disk was then applied to the white, blue, and filter images (Fig 3[c]).

Wood and bark isolation. After isolating the background, the location of the pith was manually determined in Python with the coordinates saved in a CSV file. The red channel of the filter image was used to isolate the bark from the wood because the inner bark near the wood and outer bark were uniformly dark and thus enabled the clear separation of wood and bark. The one area where the bark was similar to the wood was at the pith, which is made up of ground tissue, rather than the rest of the wood made up of secondary xylem tissue (Beck 2010). To isolate the pith from the bark, a white mask was applied to the pith using the coordinates of the pith (Fig 4, top left image). An initial mask of the bark was created by thresholding the image with any pixel value less than 30 being converted to 255 (white) and the rest of the pixels converted to 0 (black). The bark mask was applied on the whole-disk white images to remove the bark; however, some regions on the outside of the bark were bright due to the orange paint that fluoresced (Fig 3[a], image on the right). To correct for this, the largest contour (Arbeláez et al 2011; Papari and Petkov 2011) of the image, which was the wood, was retained and converted to a mask. A corrected bark mask (Fig 4, top right image) was created using the whole-disk mask and the wood mask. The correct bark mask was then applied to each whole-disk white image to isolate the wood from the entire disk (Fig 4, bottom left image).

Wood and bark area. The whole-disk area in pixels containing both the wood and bark was determined by counting the number of nonwhite pixels (pixel value <255) in the blue channel of the white image (Fig 3 c, image on the left). The total wood area in pixels was determined by counting the number of nonwhite pixels (pixel value <255) from the blue channel of the isolated wood image (Fig 4, bottom left image). The blue channel of the white images was used in both these instances because only the background was white (pixel value 255) and none of the disk features had a pixel value of 255. Other channels
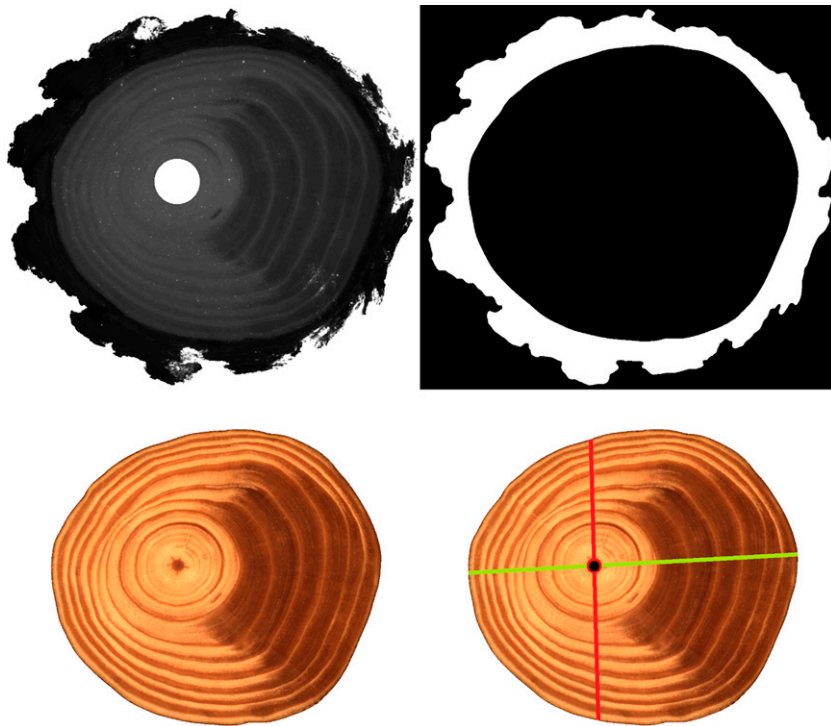
Figure 4.   The top left image shows the red channel of the filter image with a white mask applied to the pith and the wood appearing lighter than the bark which appears much darker. The top right image shows the bark mask made using the whole-disk mask and the wood mask found after finding the largest contour. The bottom left image shows the isolated wood after applying the mask. The bottom right image shows the longest (green) and the shortest (red) diameters passing through the pith.

that allow whole-disk and wood area calculation in a similar fashion include the green channel of the white images, the red channel of the blue images, and all the channels (red, green, and blue) of the filter images. Hence, the red channel of the white images, and the blue and green channels of the blue images are not suitable for this purpose because earlywood in these channels appeared white (pixel value 255). The bark area was calculated by subtracting the wood area from the whole-disk area.

Inside and outside bark diameters. The whole-disk mask and the wood mask were used to detect the edges by applying a canny edge detection algorithm (Canny 1986) which returns a one-pixel-wide outline of the wood and bark edges with the edges as white (pixel value 255)

and the rest of the image black (pixel value 0). To calculate the average inside and outside bark diameters, the Euclidean distance from the pith coordinates to each individual edge pixel coordinates was determined and the mean radius was calculated, which was converted to diameter. To obtain distinct edges prior to using canny edge detection, a median filter was applied to the whole-disk mask and the wood mask with a kernel (size 11×11), the images were then eroded with a kernel (size 7×7), after which they were dilated using a kernel (size 7×7) (Huang et al 1979; Efford 2000; Singh 2019).

Out-of-round index and pith eccentricity. The extent of a disk out of round was determined by calculating an index value adapted from Fallah et al (2012) which uses the maximum and the

minimum inside bark diameters in a plane that included the pith of each disk as

Out-of-round index

$$= \frac{\text{Maximum diameter} - \text{Minimum diameter}}{\text{Maximum diameter}}.$$

$$(1)$$

To calculate the maximum and minimum inside bark diameters, all the possible straight lines passing through the pith from each individual edge pixel coordinates to their opposite ends in the canny edge image of the wood mask were determined, and then the two straight lines with the maximum and minimum length found (Fig 4, bottom right image). With Eq 1, disks that were more out of round would have an index value closer to 1 while a disk from a circular stem would have an index value closer to 0.

Pith eccentricity as defined by Moya et al (2008) was calculated as the Euclidean distance between the geometric center of the disk and the pith coordinates and is expressed as a percentage of the mean disk radius:

Pith eccentricity (%)

$$= \frac{\substack{\text{Euclidean distance between the} \\ \text{pith and the geometric center}}}{\text{Mean radius}} \times 100.$$

$$(2)$$

To obtain the geometric center coordinates, a contour finder algorithm on wood masks was applied which would return a single contour and then the central coordinates of the contour extracted via image moments (Bradski 2000).

Severe compression wood. To detect severe compression wood in disks, the white isolated wood images (Fig 4, bottom left image) were used and converted from RGB color space to the YCrCB color space (Jack 2007). The Cb channel (Fig 5, top left) shows the severe compression wood as being brighter than the rest of the image. The image was binarized (threshold) whereby any pixel less than or equal to 95 (determined through experimentation) was not severe

compression wood, and any pixel value greater than 95 was severe compression wood. The area near the pith was falsely classified as severe compression wood so after converting the image to binary, the pith was removed based on its coordinates. A median filter (Huang et al 1979; Singh 2019) was applied using a kernel (size 9×9) to reduce noise. The resultant compression wood mask is shown in Fig 5, top right. For the illustration of severe compression wood, the black pixels were converted to lime green (R = 153, G = 255, and B = 51) and this mask was applied to the wood images (Fig 5, bottom left). The resultant images were then manually checked to determine if the technique classified severe compression wood correctly.

The spatial distribution of severe compression wood in disks from defect trees was quantified by dividing the disks using a circular grid beginning at the pith (Fig 5, bottom right). Triangles originating from the pith were constructed at 10-degree increments with 20-pixel radius increments. At each subsection, the amount of severe compression wood as a percent of the subsection was calculated. This provided both the quantity and location of severe compression wood occurrence within a disk.

Statistical Analysis

Following the image analysis work in Python (Python Software Foundation, https://www.python.org/), the results were saved to a CSV file. For the remaining statistical analysis and graphics, R (R Core Team 2020) with the R studio interface (RStudio 2020) was used, along with the tidyverse collection of packages (Wickham et al 2019) for data munging and ggplot2 (Wickham 2016) for plotting. The length and area measurements in pixels were converted to cm or cm^2. Wood and bark areas were multiplied by the thickness of the disk (recorded using the ultrasonic sensor that positioned the disk at a fixed distance from the lens) to calculate the wood and bark volumes in cm^3. Plots were made for all volumes and diameter measurements and linear models were fitted to determine how accurate the images were to the reference measurements. The accuracy of the
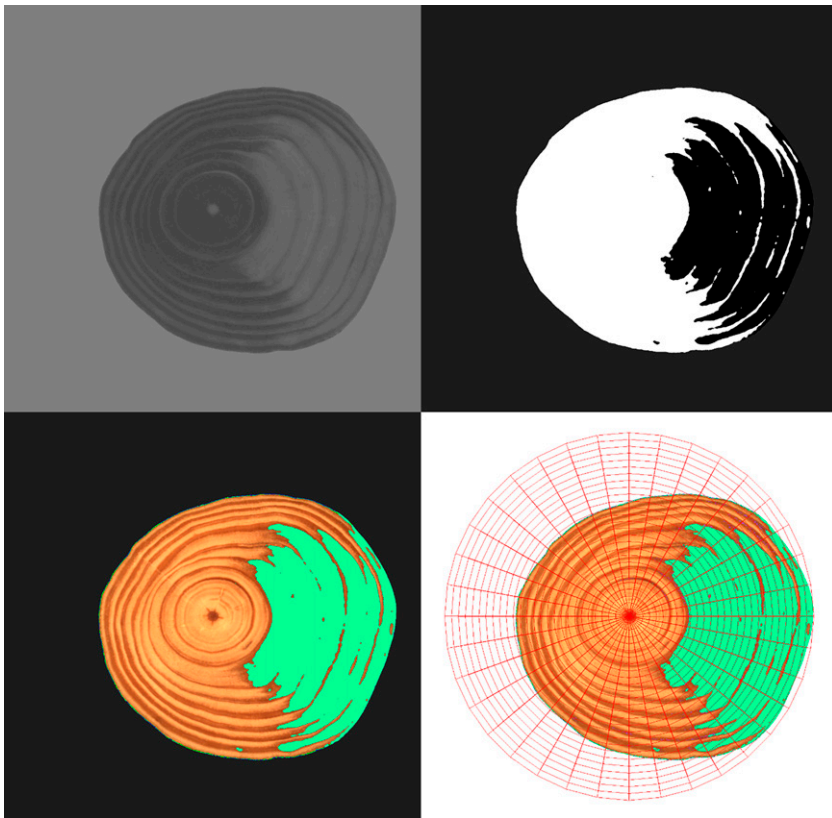
Figure 5.   Steps involved in the detection and quantification of severe compression wood using the Cb channel (top left) from the YCrCb colorspace image. Image after thresholding and binarizing after removing the pith and applying a median filter (top right). The identified compression wood areas were then overlaid on wood-only images with lime green color for visualization (bottom left). A figure showing the circular grid divided into a definite number of spatially labeled subsections overlaid on to disk images from defect trees to enable quantification of severe compression wood with their location within a disk (bottom right).

image measurements was assessed by calculating the coefficient of determination (R^2) and mean absolute percentage error.

A plot showing the out-of-round index for the disks from defect and defect-free trees as a function of relative height (disk height divided by the total height) was produced. Analysis of variance (ANOVA) by means of a linear mixed effects model where stands and trees were treated as random factors was conducted using the lmerTest package (Kuznetsova et al 2017) to test for differences in out-of-round index and pith eccentricity in disks from defect and defect-free trees, and from cutover and old field sites. A plot to show the relationship between out-of-round index and

pith eccentricity was created and a locally estimated scatterplot smoothing curve was fitted to the data points. Severe compression wood detection accuracy was determined qualitatively through a side-by-side visual inspection of white images with images in which severe compression wood was labeled. Spearman rank correlation was computed to indicate the strength of association between the amount of severe compression wood occurrence in a disk with out-of-round index and pith eccentricity. Quantity and location information of severe compression wood in disks from defect trees was used to create a single final map that showed the spatial distribution of severe compression wood. This was achieved in *R* using the
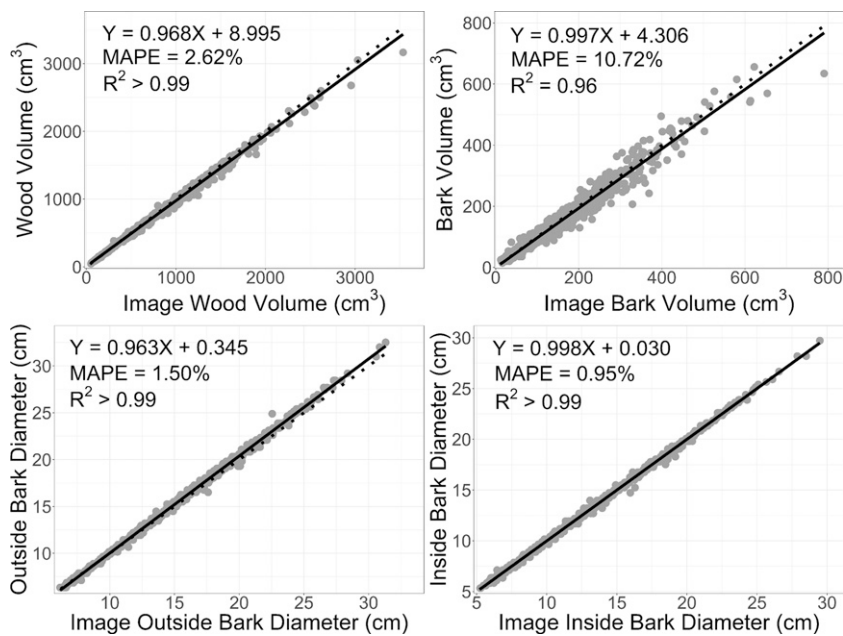
Figure 6.   Reference wood and bark volumes and outside and inside bark diameter of disks plotted against the same estimates obtained from images. The solid line in each of the four plots represents the linear model fitted for the data and the dotted line represents the 1:1 line.

gstat (Pebesma 2004; Gräler et al 2016), raster (Hijmans 2022), and spatstat (Baddeley et al 2015) packages.

RESULTS

Wood and Bark Volumes and Outside Bark and Inside Bark Diameters

The relationship between the reference measurements and the image-estimated volume and diameter measurements is shown in Fig 6. The four measurements were in close agreement with the image estimated measurements. The 1:1 line (dotted line) showed that the images slightly overpredicted wood and bark volumes. The images

slightly underpredicted the outside bark diameters, particularly as the diameter increased, while there was little difference between the two inside bark diameter measurements.

Out-of-Round Index and Pith Eccentricity

The mean out-of-round index value for the disks in this study was 0.06 (Table 2). The disks from defect trees had a significantly higher mean out-of-round index value (0.08) as compared with the disks from defect-free trees (0.05) ($p < 0.0001$). The first plot in Fig 7 shows that all the disks that have an out-of-round index value greater than 0.20 come from defect trees. Mean out-of-round index values for disks from cutover sites (0.07)

Table 2. Summary of out-of-round index and pith eccentricity for the overall data and separated by defect and defect-free longleaf pine trees.

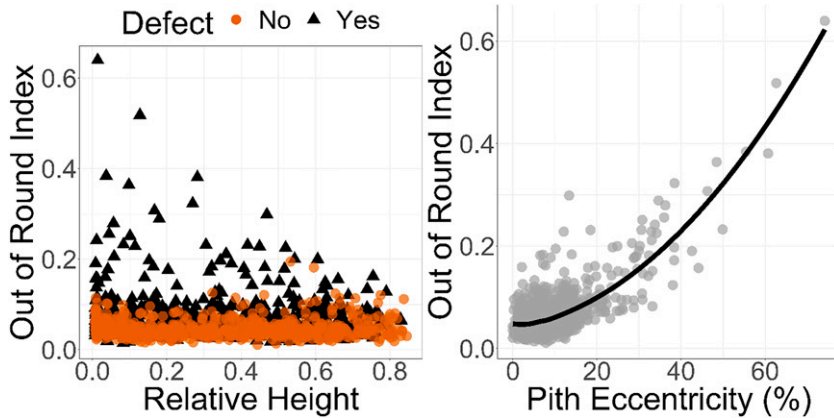| Property	Overall				Defect-free				Defect				p value
	Mean	SD	Min	Max	Mean	SD	Min	Max	Mean	SD	Min	Max	
Out-of-round index	0.06	0.05	0.01	0.64	0.05	0.02	0.01	0.19	0.08	0.06	0.01	0.64	<0.0001
Pith eccentricity (%)	8.2	7.5	0.0	74.2	5.7	3.6	0.0	28.7	10.8	9.4	0.0	74.2	<0.0001

Figure 7.   Out-of-round index plotted against relative height for all the disks (first plot). Out-of-round index plotted against pith eccentricity and a locally estimated scatterplot smoothing curve fitted to the data points shown in the second plot.

were not significantly different from old field sites (0.06) (p = 0.232). Disks that had the highest out-of-round index values (>0.3) came from relative heights less than 0.3 from defect trees (Fig 7, first plot). Disks that had the highest pith eccentricity values (>40%) came from relative heights less than 0.4 from defect trees, otherwise similar conclusions as found for out-of-round index apply here. Pith eccentricity showed a moderate positive correlation with out-of-round index (R = 0.43), and when plotted (Fig 7, second plot) shows a nonlinear relationship where out-of-round index increased at an increasing rate as pith eccentricity increased.

Severe Compression Wood

A total of 89 disks having severe compression wood were visually identified and the amount of severe compression wood was quantified. On disks that did not have severe compression wood (the remaining 1031 disks), latewood was falsely classified as compression wood. Hence, the algorithm is not recommended for images of disks that

do not have severe compression wood or have only mild-to-moderate compression wood. In the 89 disks that had severe compression wood, on average 30.3% of the wood portion of the disks was comprised of severe compression wood (Table 3). There were 49 disks from cutover sites with 33.5% of the wood portion of the disks composed of severe compression wood, which was not significantly different from the 40 disks from old field sites that had 26.3% (p = 0.496). Examining the tree defect types for the 89 disks that were classified as having severe compression wood, a majority (54 out of 89) of the disks came from trees that had excessive sweep (Table 4). On average, 35.1% of the wood portion in those 54 disks from sweep trees was severe compression wood. A total of 23 disks from trees classified as having a combination of at least two or all possible visible stem defects which include forking, sweep, and ramicorn branching had severe compression wood occurrence; trees having such a combination of visible stem defects were labeled as "mixed defect" trees. There was only one disk from a tree with no visible stem defect that had

Table 3. Summary of the 89 longleaf pine disks that had severe compression wood.

Property	Overall (N = 89)				Cutover (N = 49)				Old field (N = 40)				p value
	Mean	SD	Min	Max	Mean	SD	Min	Max	Mean	SD	Min	Max	
Compression wood (%)	30.3	15.8	6.8	62.3	33.5	16.4	6.8	61.9	26.3	14.2	7.2	62.3	0.496
Diameter inside bark (cm)	11.2	3.5	5.8	19.8	11.1	2.9	5.8	17.8	11.2	4.2	6.1	19.8	0.831

Table 4. Summary of the 89 longleaf pine disks having severe compression wood occurrence in different defect types.

Defect	Compression wood (%)				Out-of-round index				Pith eccentricity (%)			
	Mean	SD	Min	Max	Mean	SD	Min	Max	Mean	SD	Min	Max
Fork ($N = 11$)	25.9	10.4	11.0	43.3	0.15	0.07	0.07	0.30	24.8	9.1	11.0	38.0
Sweep ($N = 54$)	35.1	16.9	6.8	62.3	0.17	0.12	0.04	0.64	26.2	15.6	4.4	74.2
Mixed defects ($N = 23$)	21.3	10.4	7.2	41.1	0.14	0.06	0.05	0.23	22.3	10.6	1.1	38.4
Defect-free ($N = 1$)	24.8	—	—	—	0.07	—	—	—	21.9	—	—	—

Mixed defects include disks from trees that had a combination of at least two visible stem defects which included forking, sweep, and ramicorn branching.

severe compression wood (Table 4). Spearman rank correlation coefficients, calculated to investigate the strength of association between out-of-round index and pith eccentricity with severe compression wood quantity, showed that both out-of-round index and pith eccentricity were moderately correlated to severe compression wood quantity with correlation coefficient values of 0.54 and 0.48, respectively. A plot showing the spatial distribution of severe compression wood occurrence relative to the disk diameter in disks from defect trees is shown in Fig 8. On average, disks from defect trees had lower severe

compression wood ($<1\%$) near the pith and the amount increased toward the bark (6%).

DISCUSSION

It was demonstrated that imaging can be used to replicate reference measurements done on wood disks to calculate volume and diameter measurements. Overall, the volume and diameter results from the images provided similar results as the reference measurements determined using water displacement to measure volume, or using a diameter tape to measure the diameter of the disks. This was possible because of accurate camera calibration and a fixed focal length. The images slightly overpredicted the wood and bark volumes. The reason for the overprediction of wood volume is that the disk surface is assumed smooth in the images, with equal thickness throughout the entire disk. However, as only one surface was machined for imaging, the bottom surface was still rough cut from the chainsaw. This uneven surface on the bottom of the disk resulted in a slight overprediction of volume. Another reason for possible differences at the individual disk level is that images are two-dimensional, and the area calculated is for the one surface that is imaged, and thus the imaging ignores diameter changes with height due to taper (Burkhart and Tomé 2012). Other possible sources of error are localized growth deformations on the sides of the disks which are not accounted for during imaging. In addition to biological differences within the disks themselves is the accuracy of the ultrasonic sensor and the assumption that the disks were of even thickness. It is important to note that these errors were small and
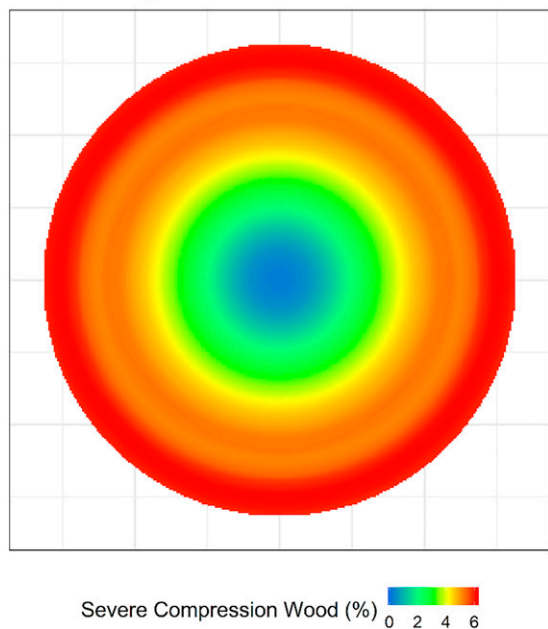

Figure 8. Spatial distribution of severe compression wood relative to the disk diameter in disks from defect trees.

imaging for wood volume had $R^2 > 0.99$. Another possible source of error is any error in the reference method, since no method is without error.

The bark volume had lower accuracy than the wood volume, but still high prediction accuracy ($R^2 = 0.96$). For wood volume, the volume measurement of wood and the imaging are done on the exact same piece, that is the full disk. Bark has more error because the image volume of bark was the entire bark, whereas with the reference method, the largest piece of bark was used (since bark comes off in pieces during the peeling process), and the volume of the piece is scaled up to the full bark volume based on the weight of the bark vs the weight of the piece. Because the image bark volume represents the entire bark volume, the image measurement is likely more accurate than the work done on the piece of bark.

The measurement of diameter from the images consistently underpredicted the outside bark diameter, whereas there was almost no difference in inside bark diameter measurements. After peeling the bark from the wood, the wood surface is relatively smooth and nearly free of any fissures. Whereas with the outside bark diameter, as the disks get larger, the outer bark shape is more irregular with more fissures (Eberhardt 2015). When measuring the diameter using a diameter tape, the diameter tape is pulled tight over the fissures which overestimate the diameter slightly. With smaller disks found higher up the tree, bark thickness is more uniform, and smaller differences were observed between the reference and the image measurements. In longleaf pine, the inner bark is approximately 15% of the total bark thickness at the stump height, whereas toward the top of the tree, the inner bark thickness is more than 40% of the total bark thickness (Eberhardt 2013).

Using the white light disk images, the amount of severe compression wood within the disks was estimated. It was acknowledged that it is an estimate as the technique only worked for severe compression wood. Generally, mild compression wood can be difficult to quantify (Thomas and Collings 2015). Here it was relatively easy to determine if the method was working for a disk by

overlaying algorithm-detected severe compression wood onto the actual image, and manually verifying each disk for accuracy. The disks were imaged green as the compression wood in fresh disks had a darker reddish appearance which can improve accuracy in detection when using an RGB camera (Timell 1986; Nyström and Kline 2000). However, many researchers have noted the inability of an RGB camera alone to accurately detect compression wood areas (Duncker and Spiecker 2009), particularly for segmenting mild compression wood from latewood (Pont et al 2007). Latewood SG increases from pith to bark in southern pines including longleaf pine, with the latewood band of cells having lower density near the pith, and these rings can be difficult to distinguish even at higher resolution (Dahlen et al 2018). Nyström and Kline (2000) used a multivariate regression model to identify compression wood, using a color line scan camera and X-rays. They concluded that X-rays were not effective at compression wood identification; however, their multivariate regression model which focused on color information had an accuracy of more than 87% in detecting compression wood. The relatively high accuracy of compression wood identification by Nyström and Kline (2000) may be due to the surface imaged; they scanned the tangential and radial surfaces of green lumber, whereas the transverse surface of cross-sectional disks were imaged here. The amount of compression wood can be manually segmented on the disks themselves using a planimeter, or alternatively, the areas can be manually segmented using an image software, but both methods are extremely time consuming (Andersson and Walter 1995; Thomas 2014).

The fluorescence image could result in reliable separation between the latewood and the compression wood, but it was not the case. Thomas (2014) found that global values for thresholding compression wood were not successful for very juvenile radiata pine (*Pinus radiata*) (aged 1-3 yr old), and the same conclusion was reached here for longleaf pine. At an individual disk level, mild compression wood can be distinguished from latewood, and thus in the future, it may be possible to correctly identify compression wood using a machine

learning approach (Michelucci 2018; Bhuyan 2019; Singh 2019); however, labeling the compression wood is time-consuming. Duncker and Spiecker (2009) found that hyperspectral imaging had an accuracy greater than 91% in classifying severe compression wood, moderate compression wood, normal wood, and cracks in cross-sectional disks of Norway spruce (*Picea abies*). Cutting samples thin, either using a microtome, or to a few mm in thickness and using transmitted light can result in accurate quantification of compression wood, at the expense of greatly increased sample preparation (Andersson and Walter 1995; Rune and Warensjö 2002; Thomas 2014; Thomas and Collings 2015). Even though there are clear challenges with compression wood identification, the method was successful in extracting more information than is typically attained without imaging and the measurement and verification process is relatively fast.

A major advantage of imaging disks over the reference methods is that the images enable other measurements to be collected. For example, how much a disk was out of round and how far the pith was from the geometric center expressed as pith eccentricity was calculated. Rune and Warensjö (2002) calculated pith eccentricity and out-of-roundness for 6-yr-old, planted Scots pine (*Pinus sylvestris*) trees grown in Sweden and reported that pith eccentricity values were highest near the stem base, a finding that agrees with our pith eccentricity results. Eccentric radial growth and compression wood formation are often synonymous (Timell 1980). Rune and Warensjö (2002) reported a Spearman rank correlation coefficient of 0.44 between severe compression wood and pith eccentricity, similar to 0.48 that was found in this study. However, they found almost no correlation ($R = 0.06$) between out-of-roundness and severe compression wood and moderate correlations ($R = 0.36$) between out-of-roundness and pith eccentricity. Rune and Warensjö (2002) calculate out-of-roundness and pith eccentricity slightly different from this study; however, it is more probable that the different species and the age of the trees impacted the results. Some studies calculated the out-of-roundness and pith

eccentricity the same way as Rune and Warensjö (2002) (Warensjö and Rune 2004; Raatevaara et al 2020) while others calculated them differently (Williamson 1975; Moya et al 2008; Medhurst et al 2011; Fallah et al 2012; Sauter et al 2019). The study objective was not to go in-depth and compare different studies on their methods to calculate out-of-round index and pith eccentricity values, but rather to show that the image analysis steps described can provide information to enable such calculations.

An additional advantage to imaging is the digital record of the image itself, which can be used for a number of purposes including comparing models generated to the actual disks, visual reference for different silvicultural treatments, as well as others. There is comparably little information available in the literature on imaging wood disks. The closest work is from Scion's DiscBot—which is a purpose-built wood quality instrument consisting of an RGB camera, a hyperspectral imaging system, an acoustic velocity scanner, and an X-ray system (Schimleck et al 2019). The DiscBot uses dry disks which are cut in half prior to drying to avoid cracking that occurs due to differential shrinkage (radial shrinkage is less than tangential shrinkage). After drying, the DiscBot system captures wood property variation both radially and circumferentially. Most wood and fiber quality studies looking at within-tree variation collect disks from multiple height levels, but from each disk, wood property variation is typically only measured radially, and hence, variation in circumference is not usually measured (Schimleck et al 2019). For example, the laboratory instruments used at the Wood and Fiber Quality laboratory at the University of Georgia are generally set up to work for radial variation and thus cannot be used on large disks. Here, using imaging on green disks, the surface of the disks is machined, imaged, and then processed as per the normal laboratory procedures. While variation due to circumference is usually ignored, Eberhardt et al (2018) found the northern side of mature longleaf pine trees growing in the southeastern United States to have higher ring SG and higher latewood proportion compared with the southern side.

Advancement in computing hardware in recent times has enabled complex image analysis to be carried out. For example, deep learning is one such modern machine learning image processing and data analysis tool that has shown considerable potential (Kamilaris and Prenafeta-Boldú 2018). Computer vision-based wood identification is a new research field in wood science where imaging in combination with machine learning techniques has been used to accurately identify various wood species (Yadav et al 2017; Hwang and Sugiyama 2021; Ravindran et al 2021, 2022a, 2022b). It has been noted that more complex, nonlinear methods such as deep learning with neural networks that use various convolutions to provide a hierarchical representation of data could provide more accurate estimates than existing, conventional methods (Raatevaara et al 2020; Hwang and Sugiyama 2021). However, one drawback of deep learning methods is the need for large datasets when training the models (Hwang and Sugiyama 2021). Perhaps in the future, deep learning methods of image classification of compression wood could result in accurate quantification of mild and moderate compression wood.

CONCLUSIONS

An imaging technique was developed to replicate reference wood and bark volume measurements typically made using water displacement. The results from image analysis were in close agreement with the results from the standard methods. Outside bark and inside bark diameters measured from images were also in close agreement with the measurements taken using a diameter tape. Imaging combined with effective surface preparation of green disks can aid in extracting accurate spatial measurements from images. Discrepancies between wood volume measurements were less than bark volume measurements because the wood volume measurement is done on whole-disks for both the standard and imaging methods; whereas the standard bark volume measurement is done only on the largest piece obtained after peeling bark from the green disk and the volume of that piece is then extrapolated to the total bark volume using the bark weight. Because the image represents the entire surface of the bark, it is possible that bark volume measurement from an image is more accurate than the reference method made using a bark piece. There was almost no difference between methods for measuring diameter inside bark, whereas outside bark diameter had more variability. The outside bark surface is usually rough with fissures whereas the inside bark surface is smooth and more consistent.

Estimates of how much a cross-sectional disk was out of shape by calculating an out-of-round index, and how far the pith was from the geometric center by calculating pith eccentricity values were made. Out-of-round index was found to have a moderate positive correlation with pith eccentricity. Disks that had the highest out-of-round index and pith eccentricity values came from lower sections of a defect tree having at least one visible stem defect. Both out-of-round index and pith eccentricity were moderately correlated to severe compression wood quantity. More than 98% of the disks that had severe compression wood occurrence came from defect trees. A majority of the disks (more than 60%) having severe compression wood came from trees that had excessive sweep. It was not possible to isolate mild-to-moderate compression wood from latewood using global parameters, thus the parameters would need to be tuned for each disk which necessitates the use of complex machine-learning algorithms. The methods developed in this study can be universally applied to cross-sectional disks from other southern pines and tree species of different age groups with slight modifications to the threshold values mentioned for segmentation.

Rayonier for allowing us to collect samples from their planted longleaf pine stands. We are grateful to Bryan Simmons, Thomas Harris, Mark Porter, and the Plantation Management Research Cooperative field crew members for their help with field work and sample collection.

REFERENCES

Andersson C, Walter F (1995) Classification of compression wood using digital image analysis. Forest Prod J 45:87-92.

Arbeláez P, Maire M, Fowlkes C, Malik J (2011) Contour detection and hierarchical image segmentation. IEEE Trans P Anal Mach Intell 33:898-916. https://doi.org/10.1109/TPAMI.2010.161

ASTM (2017) D2395-17. Standard test methods for density and specific gravity (relative density) of wood and wood-based materials. ASTM, West Conshohocken, PA.

Auty D, Achim A, Macdonald E, Cameron AD, Gardiner BA (2014) Models for predicting wood density variation in Scots pine. Forestry 87:449-458. https://doi.org/10.1093/forestry/cpu005

Auty D, Gardiner BA, Achim A, Moore JR, Cameron AD (2013) Models for predicting microfibril angle variation in Scots pine. Ann Sci 70:209-218. https://doi.org/10.1007/s13595-012-0248-6

Baddeley A, Rubak E, Turner R (2015) Spatial point patterns: methodology and applications with R. Chapman and Hall/CRC Press, London, UK.

Beck CB (2010) An introduction to plant structure and development: plant anatomy for the twenty-first century, 2nd edition. Cambridge University Press, Cambridge, UK.

Bhuyan MK (2019) Computer vision and image processing: fundamentals and applications. CRC Press, Boca Raton, FL.

Bradski G (2000) The OpenCV library. Dr Dobb's J Softw Tools 120:122-125.

Bucur V (2003a) Nondestructive characterization and imaging of wood. Springer, Heidelberg.

Bucur V (2003b) Techniques for high resolution imaging of wood structure: a review. Meas Sci Technol 14:R91-R98. https://doi.org/10.1088/0957-0233/14/12/R01

Burdon RD, Paul Kibblewhite R, Walker JCF, Megraw RA, Evans R, Cown DJ (2004) Juvenile versus mature wood: a new concept, orthogonal to corewood versus outerwood, with special reference to *Pinus radiata* and *P. taeda*. Forest Sci 50:399-415. https://doi.org/10.1139/x84-145

Burkhart HE, Tomé M (2012) Modeling forest trees and stands. Springer, Dordrecht, Netherlands.

Canny J (1986) A computational approach to edge detection. IEEE Trans P Anal Mach Intell PAMI-8:679-698. https://doi.org/10.1109/TPAMI.1986.4767851

Dahlen J, Auty D, Eberhardt TL (2018) Models for predicting specific gravity and ring width for loblolly pine from intensively managed plantations, and implications for wood utilization. Forests 9:1-20. https://doi.org/10.3390/f9060292

Decellee R, Ngo P, Debled-Rennesson I, Mothe F, Longuetaud F (2019) A new algorithm to automatically detect the pith on rough log-end images. Pages 518-523 *in* X Wang, UH Sauter, RJ Ross, eds. Proceedings, 21st International Nondestructive Testing and Evaluation of Wood Symposium, September 24–27, 2019. General Technical Report FPL-GTR-272. USDA Forest Service, Forest Products Laboratory, Madison, WI.

Duncker P, Spiecker H (2009) Detection and classification of Norway spruce compression wood in reflected light by means of hyperspectral image analysis. IAWA J 30:59-70. https://doi.org/10.1163/22941932-90000203

Eberhardt TL (2013) Longleaf pine inner bark and outer bark thicknesses: measurement and relevance. South J Appl For 37:177-180. https://doi.org/10.5849/sjaf.12-023

Eberhardt TL (2015) Thickness and roughness measurements for air-dried longleaf pine bark. Pages 374-379 *in* AG Holley, KF Connor, JD Haywood eds. Proceedings, 17th Biennial Southern Silvicultural Research Conference, March 5–7, 2013. e-General Technical Report SRS-203. USDA Forest Service, Southen Research Station, Asheville, NC.

Eberhardt TL, Dahlen J, Schimleck L (2017) Species comparison of the physical properties of loblolly and slash pinewood and bark. Can J Res 47:1495-1505. https://doi.org/10.1139/cjfr-2017-0091

Eberhardt TL, So CL, Leduc DJ (2018) Wood variability in mature longleaf pine: differences related to cardinal direction for a softwood in a humid subtropical climate. Wood Fiber Sci 50:1-14.

Efford N (2000) Digital image processing: a practical introduction using Java, 1st edition. Addison-Wesley Longman Publishing Co., Inc., Boston, MA.

Evans R (1994) Rapid measurement of the transverse dimensions of tracheids in radial wood sections from *Pinus radiata*. Holzforschung 48:168-172. https://doi.org/10.1515/hfsg.1994.48.2.168

Evans R, Hughes M, Menz D (1999) Microfibril angle variation by scanning X-ray diffractometry. Appita J 52:363-367.

Fallah A, Riahifar N, Barari K, Parsakhoo A (2012) Investigating the out-of-roundness and pith-off-centre in stems of three broadleaved species in Hyrcanian forests. J Sci 58:513-518. https://doi.org/10.17221/13/2012-jfs

Gräler B, Pebesma E, Heuvelink G (2016) Spatio-temporal interpolation using gstat. R J 8:204-218.

Habite T, Olsson A, Oscarsson J (2020) Automatic detection of pith location along Norway spruce timber boards on the basis of optical scanning. Eur J Wood Wood Prod 78:1061-1074. https://doi.org/10.1007/s00107-020-01558-1

Hainds MJ (2004) Establishing longleaf pine seedlings on agricultural fields and pastures. Pages 309–313 *in*

Connor KF, ed. Proceedings, 12th Biennial Southern Silvicultural Research Conference, February 24–28, 2003. General Technical Report SRS-71. USDA Forest Service, Southern Research Station, Asheville, NC.

Harris CR, Millman KJ, van der Walt SJ, Gommers R, Virtanen P, Cournapeau D, Wieser E, Taylor J, Berg S, Smith NJ, Kern R, Picus M, Hoyer S, van Kerkwijk MH, Brett M, Haldane A, Del Río JF, Wiebe M, Peterson P, Gérard-Marchant P, Sheppard K, Reddy T, Weckesser W, Abbasi H, Gohlke C, Oliphant TE (2020) Array programming with NumPy. Nature 585:357-362. https://doi.org/10.1038/s41586-020-2649-2

Hijmans RJ (2022) raster: geographic data analysis and modeling. R package version 3.5-21. https://CRAN.R-project.org/package=raster (4 April 2022).

Huang TS, Yang GJ, Tang GY (1979) A fast two-dimensional median filtering algorithm. IEEE Trans Acoust 27:13-18. https://doi.org/10.1109/TASSP.1979.1163188

Hwang SW, Lee T, Kim H, Chung H, Choi JG, Yeo H (2021) Classification of wood knots using artificial neural networks with texture and local feature-based image descriptors. Holzforschung 76:1-13. https://doi.org/10.1515/hf-2021-0051

Hwang SW, Sugiyama J (2021) Computer vision-based wood identification and its expansion and contribution potentials in wood science: a review. Plant Methods 17:47. https://doi.org/10.1186/s13007-021-00746-1

Jack K (2007) Video demystified: a handbook for the digital engineer, 5th edition. Newnes, Newton, MA.

Johnson R, Gjerstad D (2006) Restoring the overstory of longleaf pine ecosystems. Pages 271-295 in S Jose, EJ Jokela, DL Miller, eds. The longleaf pine ecosystem: ecology, silviculture, and restoration. Springer, New York, NY.

Jordan L, Clark A, Schimleck LR, Hall DB, Daniels RF (2008) Regional variation in wood specific gravity of planted loblolly pine in the United States. Can J Res 38:698-710. https://doi.org/10.1139/X07-158

Kamilaris A, Prenafeta-Boldú FX (2018) Deep learning in agriculture: a survey. Comput Electron Agric 147:70-90. https://doi.org/10.1016/j.compag.2018.02.016

Kodytek P, Bodzas A, Bilik P (2022) A large-scale image dataset of wood surface defects for automated vision-based quality control processes. F1000 Res 10:581. https://doi.org/10.12688/f1000research.52903.2

Kush JS, Goelz JCG, Williams RA, Carter DR, Linehan PE (2006) Longleaf pine growth and yield. Pages 251–267 in S Jose, EJ Jokela, DL Miller, eds. The longleaf pine ecosystem: ecology, silviculture, and restoration. Springer, New York, NY.

Kuznetsova A, Brockhoff PB, Christensen RHB (2017) lmerTest package: tests in linear mixed effects models. J Stat Softw 82:1-26. https://doi.org/10.18637/jss.v082.i13

Lerm FJ, Blumentritt M, Brink WH, Wessels CB (2017) A method for three-dimensional stem analysis and its application in a study on the occurrence of resin pockets in *Pinus patula*. Eur J For Res 136:411-420. https://doi.org/10.1007/s10342-017-1041-8

Lopes DJV, Bobadilha GDS, Grebner KM (2020) A fast and robust artificial intelligence technique for wood knot detection. BioResources 15:9351-9361. https://doi.org/10.15376/biores.15.4.9351-9361

McKinney W (2010) Data structures for statistical computing in Python. Pages 56-61 in Proceedings, 9th Python in Science Conference, June 28–July 3, 2010. Austin, Texas.

Medhurst J, Ottenschlaeger M, Wood M, Harwood C, Beadle C, Valencia JC (2011) Stem eccentricity, crown dry mass distribution, and longitudinal growth strain of plantation-grown *Eucalyptus nitens* after thinning. Can J Res 41:2209-2218. https://doi.org/10.1139/x11-135.

Megraw RA (1985) Wood quality factors in loblolly pine: the influence of tree age, position in tree, and cultural practice on wood specific gravity, fiber length, and fibril angle. TAPPI Press, Peachtree Corners, GA, USA.

Michelucci U (2018) Advance applied deep learning. Springer, New York, NY.

Morgan CJ, Powers M, Strimbu BM (2022) Estimating tree defects with point clouds developed from active and passive sensors. Remote Sens 14:1938. https://doi.org/10.3390/rs14081938

Moya R, Araya L, Vilchez B (2008) Variation in the pith parameter of *Gmelina arborea* trees from fast growth plantations in Costa Rica. Ann Sci 65:612-621. https://doi.org/10.1051/forest:2008045

Nyström J (2003) Automatic measurement of fiber orientation in softwoods by using the tracheid effect. Comput Electron Agric 41:91-99. https://doi.org/10.1016/S0168-1699(03)00045-0

Nyström J, Kline DE (2000) Automatic classification of compression wood in green southern yellow pine. Wood Fiber Sci 32:301-310.

Oh JK, Kim KM, Lee JJ (2008) Development of knot quantification method to predict bending strength using X-ray scanner. J Korean Wood Sci Technol 36:33-41.

Oh JK, Shim K, Kim KM, Lee JJ (2009) Quantification of knots in dimension lumber using a single-pass X-ray radiation. J Wood Sci 55:264-272. https://doi.org/10.1007/s10086-009-1031-7

Panshin AJ, de Zeeuw C (1980) Textbook of wood technology: structure, identification, properties, and uses of commercial woods of the United States and Canada, 4th edition. McGraw Hill, New York, NY.

Papari G, Petkov N (2011) Edge and line oriented contour detection: state of the art. Image Vis Comput 29:79-103. https://doi.org/10.1016/j.imavis.2010.08.009

Pebesma EJ (2004) Multivariable geostatistics in S: the gstat package. Comput Geosci 30:683-691.

Pont D, Brownlie RK, Grace JC (2007) Disc image-processing software for three-dimensional mapping of stem ring width and compression wood. N Z J For Sci 37:169-185.

R Core Team (2020) R: a language and environment for statistical computing. R Foundation for Statistical Computing, Vienna, Austria. https://www.R-project.org/ (3 April 2020).

Raatevaara A, Korpunen H, Mäkinen H, Uusitalo J (2020) Log end face image and stem tapering indicate maximum bow height on Norway spruce bottom logs. Eur J For Res 139:1079-1090. https://doi.org/10.1007/s10342-020-01309-0

Raut S, Dahlen J, Bullock B, Montes CR, Dickens D (2022) Models to predict whole-disk specific gravity and moisture content in planted longleaf pine from cutover and old field sites. Can J Res 52:137-147. https://doi.org/10.1139/cjfr-2021-0092

Ravindran P, Owens FC, Wade AC, Shmulsky R, Wiedenhoeft AC (2022a) Towards sustainable North American wood product value chains, Part I: computer vision identification of diffuse porous hardwoods. Front Plant Sci 12:758455. https://doi.org/10.3389/fpls.2021.758455

Ravindran P, Owens FC, Wade AC, Vega P, Montenegro R, Shmulsky R, Wiedenhoeft AC (2021) Field-deployable computer vision wood identification of Peruvian timbers. Front Plant Sci 12:647515. https://doi.org/10.3389/fpls.2021.647515

Ravindran P, Wade AC, Owens FC, Shmulsky R, Wiedenhoeft AC (2022b) Towards sustainable North American wood product value chains, Part 2: computer vision identification of ring-porous hardwoods. Can J Res 52:1014–1027. https://doi.org/10.1139/cjfr-2022-0077

Raybaut P (2009) Spyder-documentation. https://www.spyder-ide.org. Accessed April 4, 2020.

Riddell M, Cown D, Harrington J, Lee J, Moore J (2012) Assessing spiral grain angle by light transmission: -proof of concept -. IAWA J 33:1-14. https://doi.org/10.1163/22941932-90000075

Roblot G, Bléron L, Mériaudeau F, Marchal R (2010) Automatic computation of the knot area ratio for machine strength grading of Douglas-fir and Spruce timber. Eur J Environ Civ Eng 14:1317-1332. https://doi.org/10.3166/ejece.14.1317-1332

Ross RJ (2015) Nondestructive testing and evaluation of wood. Page 169 in RJ Ross ed. Nondestructive evaluation of wood, 2nd edition. General Technical Report FPL-GTR-238. USDA Forest Service, Forest Products Laboratory, Madison, WI.

Ross RJ, Pellerin RF (1994) Nondestructive testing for assessing wood members in structures: a review. General Technical Report FPL-GTR-70. USDA Forest Service, Forest Products Laboratory, Madison, WI.

RStudio (2020) RStudio: integrated development for R. RStudio, Inc., Boston, MA. http://www.rstudio.com/ (3 April 2020).

Rune G, Warensjö M (2002) Basal sweep and compression wood in young Scots pine trees. Scand J Fr Res 17:529-537. https://doi.org/10.1080/02827580260417189

Sauter UH, Staudenmaier J, Huber M (2019) High-precision determination of round wood diameters and cross-section areas. Pages 584-587 in X Wang, UH Sauter, RJ Ross eds. Proceedings, 21st International Nondestructive Testing and Evaluation of Wood Symposium, September 24–27, 2019. General Technical Report FPL-GTR-272. USDA Forest Service, Forest Products Laboratory, Madison, WI.

Schajer GS (2001) Lumber strength grading using X-ray scanning. Forest Prod J 51:43-52.

Schimleck L, Dahlen J, Apiolaza LA, Downes GM, Emms GW, Evans R, Moore JR, Pâques L, Van den Bulcke J, Wang X (2019) Non-destructive evaluation techniques and what they tell us about wood property variation. Forests 10:728. https://doi.org/10.3390/f10090728

Singh H (2019) Practical machine learning and image processing. Springer, New York, NY.

Thomas J (2014) An investigation on the formation and occurrence of spiral grain and compression wood in radiata pine (Pinus radiata D. Don.). PhD thesis, University of Canterbury, Christchurch, New Zealand.

Thomas J, Collings DA (2015) Three-dimensional visualization of spiral grain and compression wood in Pinus radiata imaged by circular polarized light and fluorescence. Wood Fiber Sci 48:22-27.

Thomas RE, Bennett ND (2014) Accurately determining log and bark volumes of saw logs using high-resolution laser scan data. Pages 299-310 in JW Groninger, EJ Holzmueller, CK Nielsen, and DC Dey, eds. Proceedings, 19th Central Hardwood Forest Conference, March 10–12, 2014. GTR-NRS-P-142. USDA Forest Service, Northern Research Station, Carbondale, IL.

Thumm A, Riddell M, Nanayakkara B, Harrington J, Meder R (2010) Near infrared hyperspectral imaging applied to mapping chemical composition in wood samples. J Near Infrared Spectrosc 18:507-515. https://doi.org/10.1255/jnirs.909

Timell TE (1980) Karl Gustav Sanio and the first scientific description of compression wood. IAWA J 1:147-153.

Timell TE (1986) Compression wood in gymnosperms. Springer-Verlag, Berlin, Germany.

Warensjö M, Rune G (2004) Stem straightness and compression wood in a 22-year-old stand of container-grown Scots pine trees. Silva Fenn 38:143-153. https://doi.org/10.14214/sf.424

Wickham H (2016) ggplot2: elegant graphics for data analysis. Springer-Verlag, New York, NY.

Wickham H, Averick M, Bryan J, Chang W, McGowan LDA, François R, Grolemund G, Hayes A, Henry L, Hester J, Kuhn M, Pedersen TL, Miller E, Bache SM, Müller K, Ooms J, Robinson D, Seidel DP, Spinu V, Takahashi K, Vaughan D, Wilke C, Woo K, Yutani H (2019) Welcome to the tidyverse. J Open Source Softw 4:1686. https://doi.org/10.21105/joss.01686

Williamson RL (1975) Out-of-roundness in Douglas-fir stems. Forest Sci 21:365-370.

Wright S, Dahlen J, Montes C, Eberhardt TL (2019) Quantifying knots by image analysis and modeling their

effects on the mechanical properties of loblolly pine lumber. Eur J Wood Wood Prod 77:903-917. https://doi.org/10.1007/s00107-019-01441-8

Yadav A, Anand RS, Dewal M, Gupta S (2017) Binary wavelet transform-based completed local binary pattern texture descriptors for classification of microscopic images of hardwood species. Wood Sci Technol 51: 909-927. https://doi.org/10.1007/s00226-017-0902-0

Zobel BJ, van Buijtenen JP (1989) Wood variation: its causes and control. Springer-Verlag, Berlin, Heidelberg.

EVALUATION OF TEST SPECIMEN SURFACE PREPARATION ON MACROSCOPIC COMPUTER VISION WOOD IDENTIFICATION

Prabu Ravindran

Scientist III
Department of Botany
University of Wisconsin
Madison, WI
and
Center for Wood Anatomy Research
USDA Forest Service, Forest Products Laboratory
Madison, WI
E-mail: pravindran@wisc.edu

Frank C. Owens†*

Associate Professor
Department of Sustainable Bioproducts
Mississippi State University
Starkville, MS
E-mail: fco7@msstate.edu

Adriana Costa†

Assistant Professor
Department of Sustainable Bioproducts
Mississippi State University
Starkville, MS
E-mail: adc751@msstate.edu

Brunela Pollastrelli Rodrigues†

Assistant Professor
Department of Forestry and Environmental Conservation
Clemson University
Clemson, SC
E-mail: brunelr@clemson.edu

Manuel Chavesta

Profesor Principal
Department of Wood Industry
Universidad Nacional Agraria La Molina
Lima, Peru
E-mail: mchavesta@lamolina.edu.pe

Rolando Montenegro

Profesor Asociado
Department of Wood Industry
Universidad Nacional Agraria La Molina
Lima, Peru
E-mail: rmontenegro@lamolina.edu.pe

---

* Corresponding author
† SWST member

Rubin Shmulsky†

Professor and Head
Department of Sustainable Bioproducts
Mississippi State University
Starkville, MS
E-mail: rs26@msstate.edu

Alex C. Wiedenhoeft

Research Botanist and Team Leader
Center for Wood Anatomy Research
USDA Forest Service, Forest Products Laboratory
Madison, WI
and
Department of Botany
University of Wisconsin
Madison, WI
and
Department of Sustainable Bioproducts
Mississippi State University
Starkville, MS
and
Department of Forestry and Natural Resources
Purdue University
West Lafayette, IN
and
Departamento de Ciências Biológicas (Botânica)
Universidade Estadual Paulista—Botucatu
São Paulo, Brasil
E-mail: acwieden@wisc.edu

Abstract. Previous studies on computer vision wood identification (CVWID) have assumed or implied that the quality of sanding or knifing preparation of the transverse surface of wood specimens could influence model performance, but its impact is unknown and largely unexplored. This study investigates how variations in surface preparation quality of test specimens could affect the predictive accuracy of a previously published 24-class XyloTron CVWID model for Peruvian timbers. The model was trained on images of Peruvian wood specimens prepared at 1500 sanding grit and tested on images of independent specimens (not used in training) prepared across a series of progressively coarser sanding grits (1500, 800, 600, 400, 240, 180, and 80) and high-quality knife cuts. The results show that while there was a drop in performance at the lowest sanding grit of 80, most of the higher grits and knife cuts did not exhibit statistically significant differences in predictive accuracy. These results lay the groundwork for a future larger-scale investigation into how the quality of surface preparation in *both* training *and* testing data will impact CVWID model accuracy.

Keywords: XyloTron, computer vision wood identification, machine learning, deep learning, surface preparation.

INTRODUCTION

The implementation and enforcement of sustainable, legal, and monetizable forest products value chains require access to wood identification expertise (Gasson 2011; Johnson and Laestadius 2011; Lowe et al 2016; UNODC 2016). This expertise, using traditional laboratory methods, is currently restricted to a handful of wood identification experts and centers and is difficult to scale up to meet global needs (Wiedenhoeft et al 2019). Multiple technologies for automated wood identification have been researched to help address this dearth of wood identification experts (Schmitz et al 2020). Powered by advances in machine

learning, democratized access to macroscopic imaging tools such as the XyloTron and Xylo-Phone (Ravindran et al 2020; Wiedenhoeft 2020), and cloud-based processing platforms, computer vision wood identification (CVWID, Khalid et al 2008; Hwang and Sugiyama 2021) has been demonstrated to be an effective and affordable technology for automated wood identification at country and continental scales for field screening purposes (Ravindran et al 2018, 2019, 2020, 2022a, 2022b; de Geus et al 2020; Arévalo et al 2021).

In traditional macroscopic wood identification (Panshin and de Zeeuw 1980; Hoadley 1990; Wheeler and Baas 1998; Ruffinatto et al 2015), experts with extensive training view anatomical features on the transverse, and often radial and/or tangential surface(s), and make taxonomical determinations based on the size, frequency, combinations, and/or patterns of features they observe (Miller et al 2002; Wiedenhoeft 2011; Arévalo et al 2020; Arévalo and Wiedenhoeft 2022). In CVWID, images with relevant wood anatomical features are processed by a model to make an identification (Khalid et al 2008; Esteban et al 2009; Filho et al 2014; Kwon et al 2017, 2019; Rosa da Silva et al 2017; Barmpoutis et al 2018; Figueroa-Mata et al 2018; Tang et al 2018; Damayanti et al 2019; de Andrade et al 2020; He et al 2020; Lens et al 2020; Souza et al 2020; Fabijańska et al 2021; Wu et al 2021). While a taxonomic determination can be based on microscopic or macroscopic features in the wood specimen, the focus of this study is macroscopic wood identification, and CVWID will refer to image-based macroscopic wood identification.

In both methods, since it is presumed that disparate taxa can be identified based on visual differences in anatomy, surface preparation is commonly employed to make anatomical features visible (or more visible). For traditional macroscopic wood identification, a specimen's transverse surface is typically cut cleanly with a hand-held utility knife (Hoadley 1990; Wiedenhoeft 2011), whereas both knife cuts and sanding have been used for specimen surface preparation in prior CVWID works

(Cerre 2016; Barbosa et al 2021; Hwang and Sugiyama 2021).

While previous CVWID studies have assumed or implied that the quality of surface preparation could influence model performance, its impact is unknown and largely unexplored (Wang et al 2013; Tang et al 2018; Damayanti et al 2019; de Andrade et al 2020). Hwang and Sugiyama (2021) suggest that effective models can be developed only by using images that show species-specific anatomical features and posit that surface preparation with a knife or sandpaper is necessary to clearly reveal those characteristics. Ravindran and Wiedenhoeft (2022) also argue that surface preparation must be sufficient to reveal anatomical characteristics relevant for identification. To the authors' knowledge, no study to date has attempted to evaluate the impact of surface preparation on CVWID model performance, especially when there is a difference in sample preparation between images of the training and testing specimens.

Ravindran et al (2021) presented the first national scale, anatomically informed 24-class CVWID model for Peruvian woods. They evaluated model predictive accuracies using a novel surrogate field testing methodology whereby mutually exclusive training and testing specimens were procured from separate xylaria—a practice that has been shown to be critical for evaluating model generalizability (Ravindran and Wiedenhoeft 2022). The specimens in both the training dataset and the testing dataset were polished to a sanding grit of 1500. As this Peruvian CVWID field model is ready for deployment, there is an urgent need to determine the approximate minimum surface quality needed for test specimens to maintain high predictive accuracy in real-life implementation.

This study evaluates the predictive accuracy of Ravindran et al's (2021) 24-class Peruvian CVWID model, trained on images of specimens prepared at 1500 sanding grit, with new testing images of the prior test specimens prepared across a series of progressively coarser sanding grits (1500, 800, 600, 400, 240, 180, and 80) and high-quality knife cuts to determine if the reduction in surface quality leads to any reduction in model

performance. Results of this initial study are expected to inform future investigations into the impact of surface preparation quality (of training *and* testing data) on CVWID models. It should be noted that the Peruvian CVWID model is evaluated as previously published, with no subsequent training or fine-tuning of the model weight parameters.

<center>MATERIALS AND METHODS</center>

Datasets

Image datasets for model testing were captured using 167 specimens from the David A. Kribs Wood Collection (PACw) and teaching collections at Mississippi State University. One hundred fifteen specimens used in field model testing in Ravindran et al (2021) were included and supplemented with 52 correctly identified and validated specimens from the teaching wood collection. Four specimens used for model testing in Ravindran et al (2021) were not included in this study due to size and geometry constraints regarding the effects of repeated sanding on specimen longevity.

The transverse surfaces of the 167 specimens were sanded by hand on a benchtop disc sander at descending grits in the following order: 1500, 800, 600, 400, 240, 180, and 80. The sander was equipped with an adjustable worktable to ensure that the transverse surface remained perpendicular to the longitudinal axis of each specimen during preparation. After sanding, each sample was inspected for burn marks and atypical sanding artifacts. If any were found, they were gently resanded at the same grit to remove them. Up to five images of the prepared surfaces were collected using the Xylo-Tron from each specimen after every grit setting.

A subset (75/167) of the sanded specimens were cut cleanly with a hand-held utility knife (Wiedenhoeft 2011) on their transverse surface. After cutting, each sample was inspected with a hand lens to ensure that the surface condition left by the 80-grit preparation had been removed. The specimens were imaged to yield up to five images per specimen.

For the knife-cut dataset, it was not possible to prepare specimens in PACw from two of the classes (Poulsenia and Schizolobium) due to reduced specimen size from repeated sanding. Ten specimens of each of these missing classes were prepared and imaged from the reference collection housed at the Universidad Nacional Agraria La Molina (UNALM) in Peru. This resulted in seven multigrit, 24-class image datasets using 167 specimens and one knife-cut image dataset from 95 specimens.

Dataset details are summarized in Table 1. As in Ravindran et al (2021), when referring to a

Table 1. Specimen counts for the test image datasets.

Class label	Sanded (specimen counts)	Knife-cut[a] (specimen counts)
Amburana	2	1
Aniba	2	1
Aspidosperma	5	2
BrosimumA	9	4
BrosimumU	2	2
Calycophyllum	7	2
Cariniana	8	4
Cedrela	20	7
Cedrelinga	6	6
Chorisia	5	4
Copaifera	3	3
Dipteryx	5	4
Eucalyptus	28	11
Guazuma	5	1
Hura	4	3
Maquira	2	1
Myroxylon	6	3
Ormosia	6	1
Pinus	2	1
Poulsenia	1	–
Pouteria	4	3
Schizolobium	3	–
Swietenia	15	8
Virola	17	3
Total	167	75

[a]For the knife-cut dataset, images from the Poulsenia and Schizolobium classes were not possible to source from the PACw and Mississippi State University teaching collections due to reduced size from repeated sanding. Ten additional images for each of those missing classes were sourced from the UNALM collection; however, those 20 images were not used in the main comparison with the data from the sanding grits due to statistical constraints, though, for completeness, they are mentioned in Appendix A.

CVWID class we use the class name without italics, but when referring to the same woods as botanical entities, we use italicization (eg the class Schizolobium vs the genus *Schizolobium*). Exemplar images from one specimen of *Cariniana* sp. were compiled to show the differences in visual surface quality at each grit (Fig 1).

Model Evaluation at Each Surface Quality

The XyloTron field model presented in Ravindran et al (2021) was trained with transfer learning (Pan and Yang 2010) using transverse surface images from 1300 specimens (housed in the USDA Forest Products Laboratory's MADw and SJRw collections) and prepared at exactly one
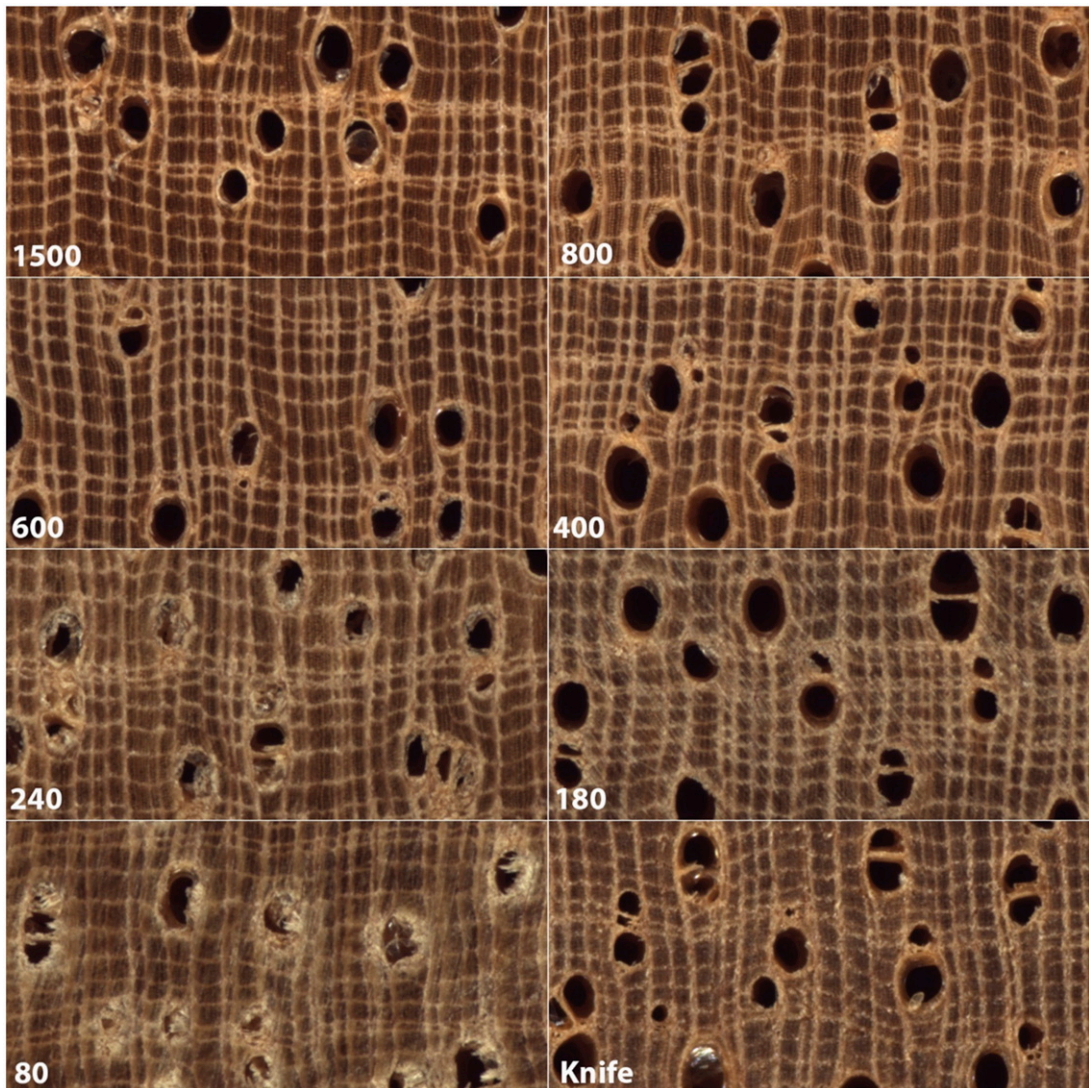
Figure 1. Exemplar images from the same specimen of *Cariniana* sp. showing the gradual decline in visual quality by descending grit number. With coarser grits (smaller number), a gradual decline in feature visibility/clarity and gradual increase in sandpaper artifacts can be observed. Each image shows 3.174 mm × 1.587 mm of tissue.

sanding grit: 1500. The published weights for the 24-class convolutional neural network (CNN, LeCun et al 1989; Goodfellow et al 2016), using the ResNet50 (He et al 2015, 2016) backbone, were used **as-is** with no further model training or finetuning to generate specimen-level class predictions for the eight image datasets. The model prediction pipeline was implemented using PyTorch (Paszke et al 2019) and Scikit-learn (Pedregosa et al 2011).

For each sample preparation condition, the top-1 and top-2 specimen-level prediction accuracies were generated using image predictions from up to five images contributed by the specimen. The majority vote, with equal weighting, of the top-k image-level predictions was taken as the corresponding top-k specimen-level prediction for the specimen contributing the images. A specimen is correctly classified if its true label is in the k predicted labels.

Statistical Analyses

Differences in field model predictive accuracy values (percent of specimens correctly identified) among the eight sanding/knife preparation groups were evaluated for statistical significance by Cochran's Q using IBM SPSS Statistics 28. Multiple comparisons were made by the method proposed in Dunn (1964). p-Values were adjusted using a Bonferroni correction to ensure an experiment-wise error rate of 0.05. p-Values are summarized in the main text. All test statistics and p-values for individual multiple comparisons are provided in Appendix A. Additionally, since the statistical tests require that all data come from the same specimens ($N=75$), the data from the 20 UNALM specimens were not used for comparison with the sanding data, but, for the sake of completeness, have been included as a separate analysis (where $N=95$) in Appendix A.

RESULTS AND DISCUSSION

The exemplar images of *Cariniana* sp. show a gradual decline in surface quality and visibility of anatomical features as the grit number decreases and the coarseness of the surface increases

(Fig 1). While the decline is barely perceptible in the higher grits, a noticeable decrease in feature clarity and an increase in sanding artifacts can be observed at around 240 grit. The knife-cut image is perhaps most comparable to the sanding quality at 400 grit.

For the specimens listed by class in Table 1, confusion matrices for the top-1 specimen-level predictions of the ResNet50-based model are provided to indicate visually where and how frequently inaccurate predictions occurred (Fig 2). The more inaccurate the performance, the more off-diagonal cells appear darkened. A quick visual comparison of the matrices reveals that the 80-grit matrix in the lower left exhibits the most off-diagonal cells. The individual confusion matrices in Fig 2, along with cell values and annotations, are presented in Appendix A.

As the sample size for the knife-cut group ($N = 75$) was smaller than those of the sanding grit groups ($N = 167$), the results are presented in two ways. When comparing the predictive accuracies (percentages of correctly identified specimens) by sanding grit group only, where $N = 167$, there was no statistically significant difference ($p > 0.05$) among the percentages of correctly identified specimens for 1500 (89.2%), 800 (95.2%), 600 (94.6%), 400 (93.4%), and 240 (88.6%) (Fig 3). Grit 180 (84.4%) was significantly different ($p < 0.05$) from 800 (95.2%), 600 (94.6%), and 80 (62.9%) only. Grit 80 (62.9%) showed a statistically significant difference from all other grits.

When comparing the predictive accuracies by sanding grit and knife-cut groups, where $N = 75$, there was no statistically significant difference ($p > 0.05$) among the percentages of correctly identified specimens for grits 1500 (93.3%), 800 (94.7%), 600 (96.0%), 400 (92.0%), 240 (92.0%), 180 (85.3%), and knife cuts (90.7%) (Fig 4). Grit 80 (69.3%) showed a statistically significant difference between all other grit and knife-cut groups ($p < 0.05$).

The results of this investigation suggest that, for these datasets, the CVWID model's predictive accuracy is robust to differences in surface
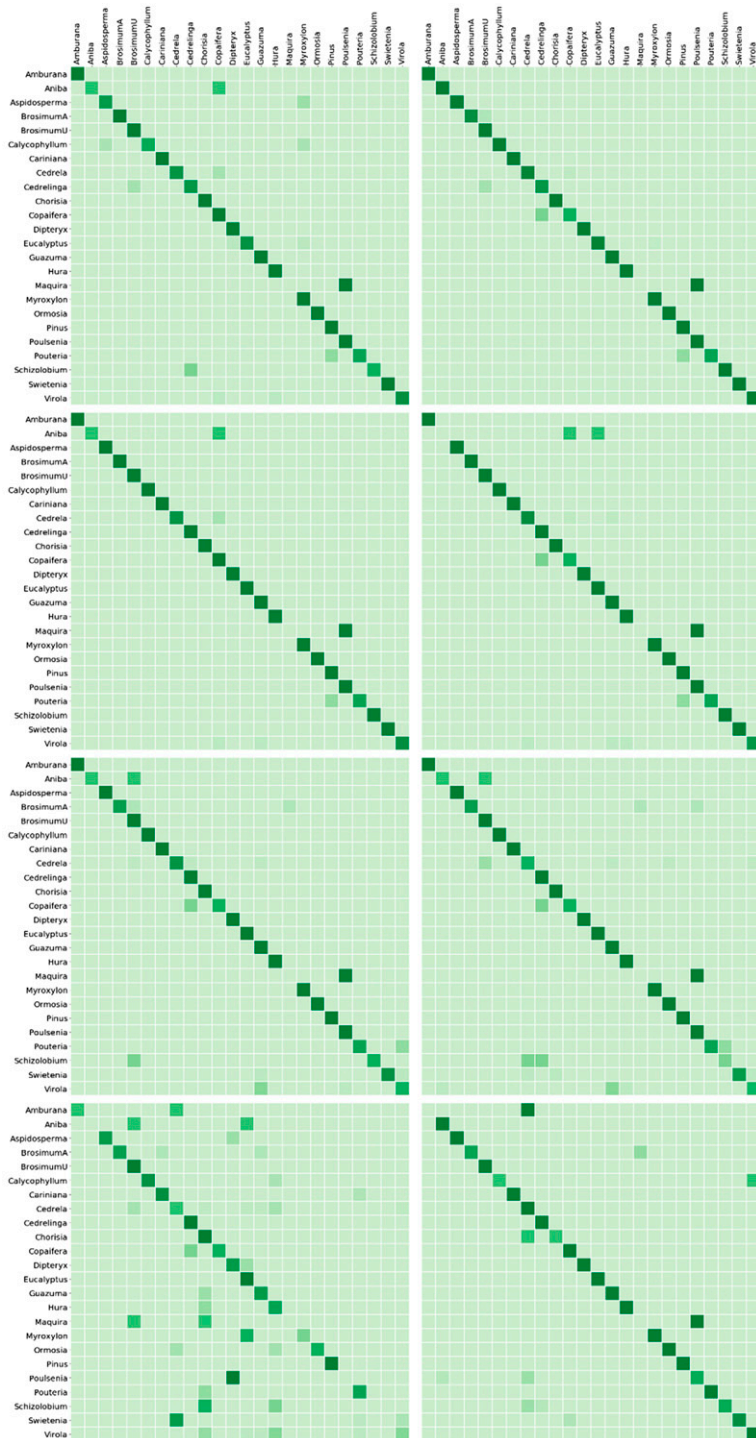
Figure 2.   Confusion matrices for top-1 specimen-level predictions of the ResNet50-based model. The sample preparation settings, in raster order, are sanding at grits 1500, 800, 600, 400, 240, 180, 80, and knife cuts. The individual confusion matrices in this figure, along with annotations, are presented in Appendix A.
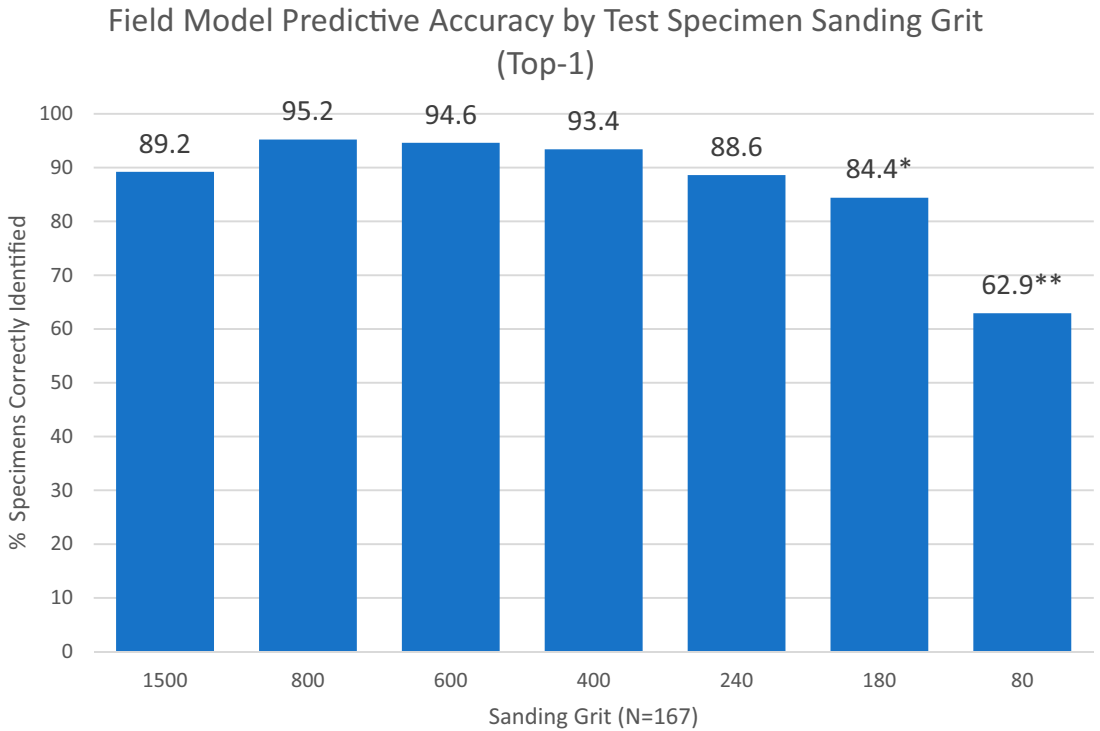
Field Model Predictive Accuracy by Test Specimen Sanding Grit (Top-1)

Figure 3. Comparison of Peru field model predictive accuracy (top-1) by sanding grit only ($N = 167$). The percentages of specimens correctly identified among the sanding grits were compared using Cochran's Q with post hoc multiple comparisons per Dunn (1964) with an experiment-wise error of 0.05. Multiple comparisons showed that there were no significant differences ($p > 0.05$) among the groups with the following exceptions. * There was a statistically significant difference ($p < 0.05$) between 180 grit and 800, 600, and 80, respectively. ** There was a statistically significant difference ($p < 0.05$) between 80 grit and all other grits, respectively.

preparation among the knife cut and sanding grits from 240 upward. At 80 grit, a sharp reduction in predictive accuracy can be observed, which might be due to the decline in feature visibility/clarity (pore boundaries, rays, etc.) and an increase in sandpaper artifacts of the kind exemplified by Fig 1. This suggests that there is a point at which the obscuring of anatomical detail and/or the increase in surface preparation artifacts results in reduced model performance, though this point could vary by species due to differences in specific gravity, hardness, and/or other properties. As variation in surface quality is a practical concern for field deployment, the impact of obscured anatomical features and sanding/knifing artifacts merits further investigation to ensure that predictive accuracy is not unnecessarily reduced by insufficient specimen preparation.

The deployment of CVWID systems can be impacted by covariate shifts (between training and deployment data), which can occur due to wood anatomy variations (eg natural forest grown vs plantation grown, changes due to environmental stresses) or operating condition variations (eg sample preparation methods, imaging parameter settings, operator skill). The focus of this study was to evaluate the predictive accuracy of a CVWID model with respect to one potential source of operator-induced covariate shift—explicit sample preparation differences between training and testing stages. Our results show that a model trained on a 1500-grit dataset has predictive accuracies that are acceptable for field screening, on images from surfaces sanded at grits coarser than 1500. Even though the predictive accuracy drops sharply for the 80-grit dataset, a
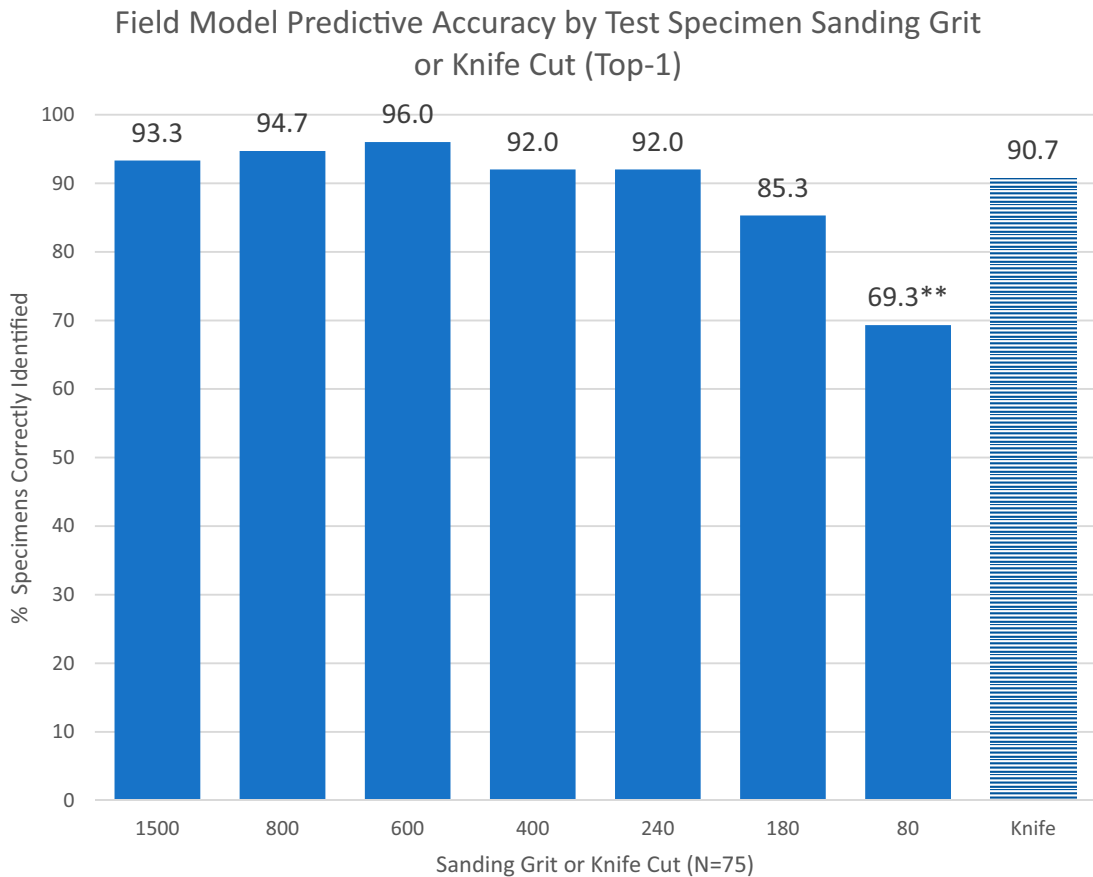
Field Model Predictive Accuracy by Test Specimen Sanding Grit or Knife Cut (Top-1)

Figure 4.   Comparison of Peru field model predictive accuracy (top-1) by sanding grit (solid bars) and knife-cut (patterned bar) groups ($N = 75$). The percentages of specimens correctly identified among all the groups were compared using Cochran's Q with post hoc multiple comparisons per Dunn (1964) with an experiment-wise error of 0.05. Multiple comparisons showed that there were no significant differences ($p > 0.05$) among the groups with the following exceptions. ** There was a statistically significant difference ($p < 0.05$) between 80 grit and all other grit and knife cut groups, respectively.

surface coarseness where the complete range of anatomical features may not be reliably discerned, the obtained accuracy of 62.9% is still considerably better than random guessing (ie for a model with 24 classes, an accuracy of ~4% would be expected). This suggests that the model generalizes acceptably in the presence of sanding grit differences between training and deployment data when the surrogate field-testing approach is employed for datasets from specimens from multiple xylaria.

It has been shown that there are biases inherent in surrogate field testing (Ravindran and Wiedenhoeft 2022). It should be noted that the question of

optimal sample preparation during the training and testing phases is still unknown and unexplored. The results of this study suggest that for field implementation of a model trained on high-grit images with a human-in-the-loop modality (eg in the *xyloinf* software for the XyloTron platform, as distributed in Ravindran et al 2020), the predictions are highly reliable at grits as low as 240. Field polishing of a specimen from 80 to 240 grit with a cordless drill and an appropriate sanding pad requires only about 20 s (Wiedenhoeft, personal observation). Field polishing requires significantly less skill and training than making high-quality utility knife cuts but has a higher hardware burden (cordless drill, batteries, chargers,

access to power to recharge, the need to carry abrasives, etc.), and so may well not be practical in some field contexts.

A comprehensive investigation of the effect surface preparation has on the predictive accuracy of CVWID models would necessitate examining the effects each surface quality has on *both* training *and* testing. As specimen preparation for the type of imaging performed in this study is both labor and time intensive, the authors elected to examine first how varying the surface quality of the test specimens might affect predictive accuracy when the model was trained on images prepared at the highest quality (1500 grit) as that directly impacts the timely release of the Peruvian CVWID field model. Results showing both statistically significant and practical differences in performance among various surface preparations in testing justify a much greater investment of time and resources introducing a second variable of training specimen preparation quality. As the training specimens from the MADw and SJRw collections outnumber the testing specimens in the PACw collection by approximately eight times, repeating this study with two variables would require many more person-hours.

Prior works in CVWID have used sanding or knife cuts for sample preparation before imaging the prepared surfaces. Both these methods have their pros and cons. The knife-cut method is "quick" and field deployment friendly but making consistent and safe knife cuts to produce a clean surface on which the anatomical features are readily observable is a skill that is practice-intensive. In addition, manipulating the knife, hand, and wrist to cleanly cut the ends of flush and tightly packed bundled lumber *in situ* without first extracting a small subsample may prove difficult or impossible. On the other hand, sanding produces consistent surfaces and is well-suited for collecting large image datasets, thus a method of choice heretofore. One way to leverage the positives of the two approaches would be to employ sanding for training image datasets and using good, clean, and skillful utility knife cuts in the field, but, as noted above, this requires operator training and skill and may not be logistically

feasible in some field contexts. Another advantage of constructing training datasets from finely sanded surfaces is that they can be used for the creation of digital archives of reference images which can be used for educational purposes. It is also easier to apply software-based image degradation approaches for data augmentation during the training procedure to improve model generalizability if one begins with high-quality images showing anatomical detail—there is no known method to enhance a low-quality dataset to include anatomical features not already observable. While our results suggest that the approach of using data from sanded surfaces for training and using utility knife cuts during deployment may be feasible for the creation of operational, field-deployable CVWID systems, the question of the optimal sanding grit for the training dataset is still open.

In principle, a path to robust models would be to train models by pooling datasets from different studies thus capturing a wide range of botanically and operationally induced covariate shifts. Until efforts for sharing and pooling multiple CVWID datasets gain traction, and workers publish the spatial scale of the images they collect (which is often not done), the method of using finely sanded specimens for training models and employing a quicker method of sample preparation (clean knife cuts or coarser grit sanding) in the field may be a reasonable pathway to operational, field-deployable CVWID systems.

CONCLUSIONS

This evaluation of a previously published 24-class CVWID model, trained on images of Peruvian specimens prepared at 1500 sanding grit, with new testing images of the prior test specimens prepared across a series of progressively coarser sanding grits (1500, 800, 600, 400, 240, 180, and 80) showed a robustness of predictive accuracy at grits 240 and higher and a reduction in performance at 180 grit and 80 grit. Moreover, it indicated that the predictive accuracy on the specimens prepared with utility knife cuts was not statistically different from that of the images

prepared at 180 grit and above. These results suggest that there is a point at which the obscuring of anatomical detail and/or the increase in surface preparation artifacts on test specimens result in reduced model performance, but minor differences at higher levels of surface preparation quality have little to no practical effect. As variation in surface preparation quality is a pragmatic concern for field deployment, the impact it has on predictive accuracy merits further investigation. These results lay the groundwork for a future larger-scale investigation into how the quality of surface preparation in *both* training *and* testing data will impact CVWID model accuracy. Models will be trained at progressively coarser grits and tested, for each grit, against the images of each testing grit used in this study.

Author Contributions: F.C.O. and R.S. provided access to and supervised data acquisition from the PACw test specimens. B.P.R. prepared and imaged the PACw specimens. M.C. and R.M. prepared and imaged the UNALM specimens. P.R. implemented the machine learning pipelines for the study. P.R. and A.C.W. conducted data analysis and synthesis. F.C.O. provided statistical analysis. P.R., A.C.W., A.C., and F.C.O. wrote the paper. All authors contributed

REFERENCES

Arévalo R, Ebanyenle E, Ebeheakey AA, Bonsu KA, Lambog O, Soares R, Wiedenhoeft AC (2020) Field identification manual for Ghanaian timbers. General technical report FPL-GTR-190. U.S. Department of Agriculture, Forest Service, Forest Products Laboratory, Madison, WI. 130 pp.

Arévalo R, Pulido ENR, Solórzano JFG, Soares R, Ruffinatto F, Ravindran P, Wiedenhoeft AC (2021) Image based identification of Colombian timbers using the XyloTron: A proof of concept international partnership. Colomb For 24(1):5-16.

Arévalo R, Wiedenhoeft AC (2022) Identification of Central American, Mexican, and Caribbean woods. General technical report FPL-GTR-190. U.S. Department of Agriculture, Forest Service, Forest Products Laboratory, Madison, WI. 376 pp.

Barbosa ACF, Gerolamo CS, Lima AC, Angyalossy V, Pace MR (2021) Polishing entire stems and roots using sandpaper under water: An alternative method for

macroscopic analyses. Appl Plant Sci 9(5):10.1002/aps3.11421.

Barmpoutis P, Dimitropoulos K, Barboutis I, Nikos G, Lefakis P (2018) Wood species recognition through multidimensional texture analysis. Comput Electron Agric 144:241-248.

Cerre JC (2016) Incident light microphotography at high depth of focus. IAWA J 37(3):506-510.

Damayanti R, Prakasa E, Krisdianto Dewi LM, Wardoyo R, Sugiarto B, Pardede HF, Riyanto Y, Astutiputri VF, Panjaitan GR, Hadiwidjaja ML, Maulana YH, Mutaqin IN (2019) LignoIndo: Image database of Indonesian commercial timber. IOP Conf Ser: Earth Environ 374:012057.

de Andrade BG, Basso VM, Latorraca JVF (2020) Machine vision for field-level wood identification. IAWA J 41(4):681-698.

de Geus A, da Silva SF, Gontijo AB, Silva FO, Batista MA, Souza JR (2020) An analysis of timber sections and deep learning for wood species classification. Multimedia Tools Appl 79:34513-34529.

Dunn OJ (1964) Multiple comparisons using rank sums. Technometrics 6:241-252.

Esteban LG, Fernández FG, de Palacios P, Romero RM, Cano NN (2009) Artificial neural networks in wood identification: The case of two *Juniperus* species from the Canary Islands. IAWA J 30(1):87-94.

Fabijańska A, Danek M, Barniak J (2021) Wood species automatic identification from wood core images with a residual convolutional neural network. Comput Electron Agric 181:105941.

Figueroa-Mata G, Mata-Montero E, Valverde-Otárola JC, Arias-Aguilar D (2018) Automated image-based identification of forest species: Challenges and opportunities for 21st century Xylotheques. *in* Proceedings, 2018 IEEE International Work Conference on Bioinspired Intelligence, July 18-20, 2018, San Carlos, Costa Rica, 1–8.

Filho PLP, Oliveira LS, Nisgoski S, Britto AS Jr. (2014) Forest species recognition using macroscopic images. Mach Vis Appl 25:1019-1031.

Gasson P (2011) How precise can wood identification be? Wood anatomy's role in support of the legal timber trade, especially CITES. IAWA J 32(2):137-154.

Goodfellow I, Bengio Y, Courville A (2016) Deep learning. The MIT Press, Cambridge, MA. 800 pp.

He K, Zhang X, Ren S, Sun J (2015) Delving deep into rectifiers: Surpassing human-level performance on ImageNet classification. *in* Proceedings, IEEE International Conference on Computer Vision (ICCV), December 7-13, 2015, Santiago, Chile, 1-11.

He K, Zhang X, Ren S, Sun J (2016) Deep residual learning for image recognition. *in* Proceedings, 2016 IEEE Conference on Computer Vision and Pattern Recognition (CVPR), June 27-30, 2016, Las Vegas, NV, 1-12.

He T, Lu Y, Jiao L, Zhang Y, Jiang X, Yin Y (2020) Developing deep learning models to automate rosewood tree species identification for CITES designation and implementation. Holzforschung 74(12):1123-1133.

Hoadley RB (1990) Identifying wood: Accurate results with simple tools. Taunton Press, Newtown, CT. 223 pp.

Hwang SW, Sugiyama J (2021) Computer vision-based wood identification and its expansion and contribution potentials in wood science: A review. Plant Methods 17:47, 1-21.

Johnson A, Laestadius L (2011) New laws, new needs: The role of wood science in global policy efforts to reduce illegal logging and associated trade. IAWA J 32(2):125-136.

Khalid M, Lew E, Lee Y, Yusof R, Nadaraj M (2008) Design of an intelligent wood species recognition system. Int J Simul Syst Sci Technol 9(3):9-19.

Kwon O, Lee H, Yang S-Y, Kim H, Park S-Y, Choi I-G, Yeo H (2019) Performance enhancement of automatic wood classification of Korean softwood by ensembles of convolutional neural networks. J Korean Wood Sci Technol 47:265-276.

Kwon O, Lee HG, Lee M-R, Jang S, Yang S-Y, Park S-Y, Choi I-G, Yeo H (2017) Automatic wood species identification of Korean softwood based on convolutional neural networks. J Korean Wood Sci Technol 45:797-808.

LeCun Y, Boser B, Denker JS, Henderson D, Howard RE, Hubbard W, Jackel LD (1989) Backpropagation applied to handwritten zip code recognition. Neural Comput 1(4):541-551.

Lens F, Liang C, Guo Y, Tang X, Jahanbanifard M, da Silva FSC, Ceccantini G, Verbeek FJ (2020) Computer-assisted timber identification based on features extracted from microscopic wood sections. IAWA J 41(4):660-680.

Lowe AJ, Dormontt EE, Bowie MJ, Degen B, Gardner S, Thomas D, Clarke C, Rimbawanto A, Wiedenhoeft A, Yin Y, Sasaki N (2016) Opportunities for improved transparency in the timber trade through scientific verification. Bioscience 66(11):990-998.

Miller R, Wiedenhoeft AC, Ribeyron M-J (2002) CITES identification guide—Tropical woods. Environment Canada, Canada.

Pan SJ, Yang Q (2010) A survey on transfer learning. IEEE Trans Knowl Data Eng 22(10):1345-1359.

Panshin AJ, de Zeeuw C (1980) Textbook of wood technology: Structure, identification, properties, and uses of the commercial woods of the United States and Canada. McGraw-Hill, New York. 736 pp.

Paszke A, Gross S, Massa F, Lerer A, Bradbury J, Chanan G, Killeen T, Lin Z, Gimelshein N, Antiga L, Desmaison A, Kopf A, Yang E, DeVito Z, Raison M, Tejani A, Chilamkurthy S, Steiner B, Fang L, Bai J, Chintala S (2019) Pytorch: An imperative style, high-performance deep learning library. Pages 8026-8037 *in* Proceedings, 2019 NeurIPS, December 3, 2019, Vancouver, Canada. https://arxiv.org/abs/1912.01703

Pedregosa F, Varoquaux G, Gramfort A, Michel V, Thirion B, Grisel O, Blondel M, Prettenhofer P, Weiss R, Dubourg V, Vanderplas J, Passos A, Cournapeau D, Brucher M, Perrot M, Duchesnay E (2011) Scikit-learn: Machine learning in Python. J Mach Learn Res 12(85): 2825-2830.

Ravindran P, Costa A, Soares R, Wiedenhoeft AC (2018) Classification of CITES-listed and other neotropical Meliaceae wood images using convolutional neural networks. Plant Methods 14:25, 1-10.

Ravindran P, Ebanyenle E, Ebeheakey AA, Abban KB, Lambog O, Soares R, Costa A, Wiedenhoeft AC (2019) Image based identification of Ghanaian timbers using the XyloTron: Opportunities, risks, and challenges. *in* Proceedings, 33rd NeurIPS, December 2019, Vancouver, Canada, 1-10. https://arxiv.org/abs/1912.00296

Ravindran P, Owens FC, Wade AC, Shmulsky R, Wiedenhoeft AC (2022a) Towards sustainable North American wood product value chains, part I: Computer vision identification of diffuse porous hardwoods. Front Plant Sci 12:758455.

Ravindran P, Owens FC, Wade AC, Vega P, Montenegro R, Shmulsky R, Wiedenhoeft AC (2021) Field-deployable computer vision wood identification of Peruvian timbers. Front Plant Sci 12:647515.

Ravindran P, Thompson BJ, Soares RK, Wiedenhoeft AC (2020) The XyloTron: Flexible, open-source, image-based macroscopic field identification of wood products. Front Plant Sci 11:1015, 1-8.

Ravindran P, Wade AC, Owens FC, Shmulsky R, Wiedenhoeft AC (2022b) Towards sustainable North American wood product value chains, part 2: Computer vision identification of ring-porous hardwoods. Can J For Res 52:1014-1027.

Ravindran P, Wiedenhoeft AC (2022) Caveat emptor: On the need for baseline quality standards in computer vision wood identification. Forests 13(4):632, 1-19.

Rosa da Silva N, De Ridder M, Baetens JM, den Bulcke JVB (2017) Automated classification of wood transverse cross-section micro-imagery from 77 commercial Central-African timber species. Ann Sci 74:30, 1-14.

Ruffinatto F, Crivellaro A, Wiedenhoeft AC (2015) Review of macroscopic features for hardwood and softwood identification and a proposal for a new character list. IAWA J 36(2):208-241.

Schmitz N, Beeckman H, Blanc-Jolivet C, Boeschoten L, Braga JWB, Cabezas JA, Chaix G, Crameri S, Deklerck V, Degen B, Dormontt E, Espinoza E, Gasson P, Haag V, Helmling S, Horacek M, Koch G, Lancaster C, Lens F, Lowe A, Martínez-Jarquín S, Nowakowska JA, Olbrich A, Paredes-Villanueva K, Pastore TCM, Ramananantoandro T, Razafimahatratra AR, Ravindran P, Rees G, Soares LF, Tysklind N, Vlam M, Watkinson C, Wheeler E, Winkler R, Widenhoeft AC, Zemke VT, Zuidema P (2020) Overview of current practices in data analysis for wood identification. A guide for the different timber tracking methods. Global Timber Tracking Network, GTTN Secretariat, European Forest Institute and Thünen Institute.

Souza DV, Santos JX, Vieira HC, Naide TL, Nisgoski S, Oliveira LES (2020) An automatic recognition system of Brazilian flora species based on textural features of macroscopic images of wood. Wood Sci Technol 54: 1065-1090.

Tang XJ, Tay YH, Siam NA, Lim SC (2018) MyWood-ID: Automated macroscopic wood identification system using smartphone and macro-lens. Pages 37–43 *in* Proceedings, 2018 International Conference on Computational Intelligence and Intelligent Systems (CIIS 2018). Association for Computing Machinery, New York, NY.

UNODC (2016) Best practice guide for forensic timber identification. United Nations Office on Drugs and Crime, New York, NY.

Wang HJ, Qi HN, Wang XF (2013) A new Gabor based approach for wood recognition. Neurocomputing 116: 192-200.

Wheeler EA, Baas P (1998) Wood identification—A review. IAWA J 19(3):241-264.

Wiedenhoeft AC (2011) Identification of Central American woods (Identificacion de las Especies Maderables de Centroamerica). Forest Products Society, Madison, WI. Publication #7215-11.

Wiedenhoeft AC (2020) The XyloPhone: Toward democratizing access to high-quality macroscopic imaging for wood and other substrates. IAWA J 41(4):699-719.

Wiedenhoeft AC, Simeone J, Smith A, Parker-Forney M, Soares R, Fishman A (2019) Fraud and misrepresentation in retail forest products exceeds U.S. forensic wood science capacity. PLoS One 14(7):e0219917.

Wu F, Gazo R, Haviarova E, Benes B (2021) Wood identification based on longitudinal section images by using deep learning. Wood Sci Technol 55:553-563.

APPENDIX A

Table A1. Cochran's Q test for Fig 3.

Total N	167
Test statistic	152.437
Degree of freedom	6
Asymptotic sig. (2-sided test)	0.000

Table A2. Pairwise comparisons for Fig 3.

Sample 1-Sample 2	Test statistic	Std. error	Std. test statistic	Sig.	Adj. sig.[a]
Grit80-Grit180	0.216	0.032	6.815	<0.001	0.000
Grit80-Grit240	0.257	0.032	8.140	<0.001	0.000
Grit80-Grit1500	0.263	0.032	8.329	0.000	0.000
Grit80-Grit400	0.305	0.032	9.655	0.000	0.000
Grit80-Grit600	0.317	0.032	10.033	0.000	0.000
Grit80-Grit800	0.323	0.032	10.222	0.000	0.000
Grit180-Grit240	0.042	0.032	1.325	0.185	1.000
Grit180-Grit1500	0.048	0.032	1.514	0.130	1.000
Grit180-Grit400	0.090	0.032	2.840	0.005	0.095
Grit180-Grit600	0.102	0.032	3.218	0.001	0.027
Grit180-Grit800	0.108	0.032	3.407	<0.001	0.014
Grit240-Grit1500	0.006	0.032	0.189	0.850	1.000
Grit240-Grit400	0.048	0.032	1.514	0.130	1.000
Grit240-Grit600	0.060	0.032	1.893	0.058	1.000
Grit240-Grit800	0.066	0.032	2.082	0.037	0.784
Grit1500-Grit400	−0.042	0.032	−1.325	0.185	1.000
Grit1500-Grit600	−0.054	0.032	−1.704	0.088	1.000
Grit1500-Grit800	−0.060	0.032	−1.893	0.058	1.000
Grit400-Grit600	0.012	0.032	0.379	0.705	1.000
Grit400-Grit800	0.018	0.032	0.568	0.570	1.000
Grit600-Grit800	0.006	0.032	0.189	0.850	1.000

Each row tests the null hypothesis that the Sample 1 and Sample 2 distributions are the same. Asymptotic significances (2-sided tests) are displayed. The significance level is 0.05.

[a]Significance values have been adjusted by the Bonferroni correction for multiple tests.

Table A3. Cochran's Q test for Fig 4.

Total N	75
Test statistic	56.751
Degree of freedom	7
Asymptotic sig. (2-sided test)	<0.001

Table A4. Pairwise comparisons for Fig 4.

Sample 1-Sample 2	Test statistic	Std. error	Std. test statistic	Sig.	Adj. sig.[a]
Grit80-Grit180	0.160	0.043	3.735	<0.001	0.005
Grit80-Knife	−0.213	0.043	−4.980	<0.001	0.000
Grit80-Grit400	0.227	0.043	5.292	<0.001	0.000
Grit80-Grit240	0.227	0.043	5.292	<0.001	0.000
Grit80-Grit1500	0.240	0.043	5.603	<0.001	0.000
Grit80-Grit800	0.253	0.043	5.914	<0.001	0.000
Grit80-Grit600	0.267	0.043	6.225	<0.001	0.000
Grit180-Knife	−0.053	0.043	−1.245	0.213	1.000
Grit180-Grit400	0.067	0.043	1.556	0.120	1.000
Grit180-Grit240	0.067	0.043	1.556	0.120	1.000
Grit180-Grit1500	0.080	0.043	1.868	0.062	1.000
Grit180-Grit800	0.093	0.043	2.179	0.029	0.822
Grit180-Grit600	0.107	0.043	2.490	0.013	0.358
Knife-Grit400	0.013	0.043	0.311	0.756	1.000
Knife-Grit240	0.013	0.043	0.311	0.756	1.000
Knife-Grit1500	0.027	0.043	0.623	0.534	1.000
Knife-Grit800	0.040	0.043	0.934	0.350	1.000
Knife-Grit600	0.053	0.043	1.245	0.213	1.000
Grit400-Grit1500	0.013	0.043	0.311	0.756	1.000
Grit240-Grit1500	0.013	0.043	0.311	0.756	1.000
Grit400-Grit800	0.027	0.043	0.623	0.534	1.000
Grit240-Grit800	0.027	0.043	0.623	0.534	1.000
Grit400-Grit600	0.040	0.043	0.934	0.350	1.000
Grit240-Grit600	0.040	0.043	0.934	0.350	1.000
Grit400-Grit240	0.000	0.043	0.000	1.000	1.000
Grit1500-Grit800	−0.013	0.043	−0.311	0.756	1.000
Grit1500-Grit600	−0.027	0.043	−0.623	0.534	1.000
Grit800-Grit600	−0.013	0.043	−0.311	0.756	1.000

Each row tests the null hypothesis that the Sample 1 and Sample 2 distributions are the same. Asymptotic significances (2-sided tests) are displayed. The significance level is 0.05.

[a]Significance values have been adjusted by the Bonferroni correction for multiple tests.
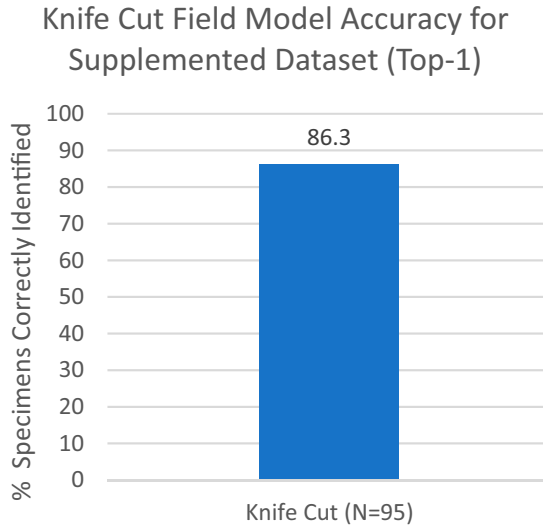
Knife Cut Field Model Accuracy for Supplemented Dataset (Top-1)

Figure A1. Predictive accuracy for knife-cut dataset including 10 additional specimens of Poulsenia and 10 additional specimens of Schizolobium, all from the UNALM collection ($N = 95$).

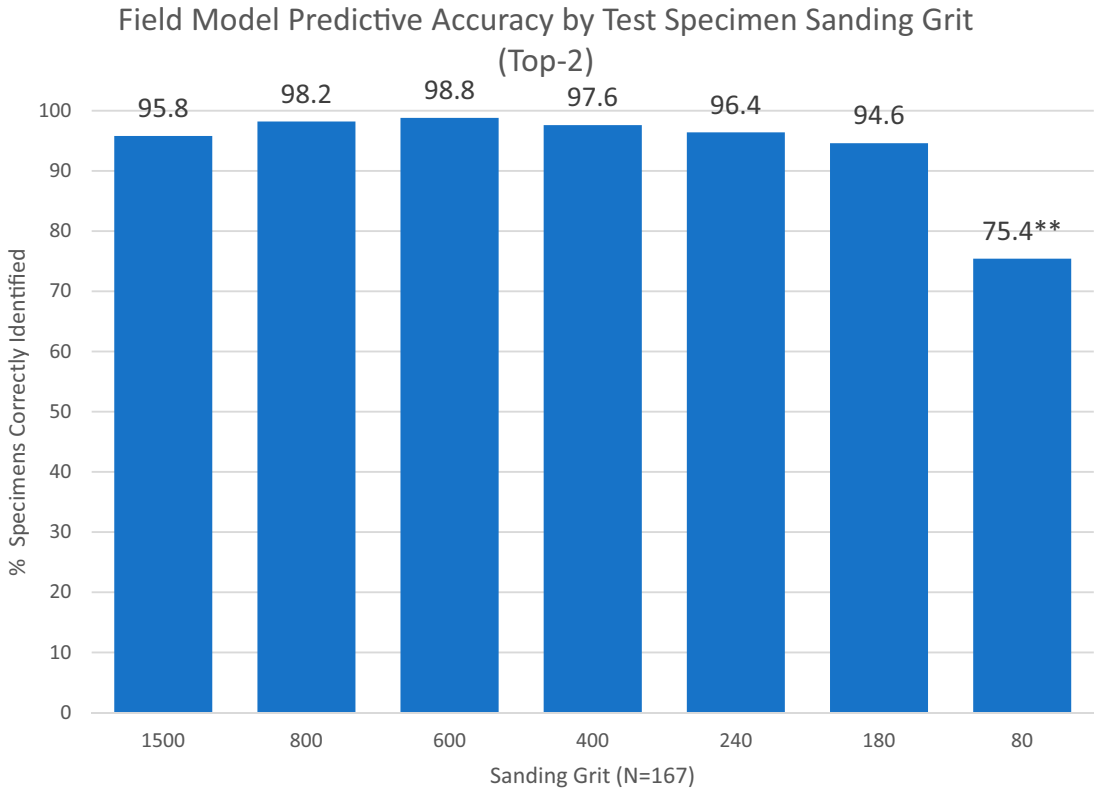## Field Model Predictive Accuracy by Test Specimen Sanding Grit (Top-2)

Figure A2. Comparison of Peru field model predictive accuracy (top-2) by sanding grit only ($N = 167$). The percentages of specimens correctly identified among all the groups were compared using Cochran's Q with post hoc multiple comparisons per Dunn (1964) with an experiment-wise error of 0.05. Multiple comparisons showed that there were no significant differences ($p > 0.05$) among the groups with the following exceptions. ** There was a statistically significant difference ($p < 0.05$) between 80 grit and all other grits, respectively.

Table A5. Cochran's Q test for Fig A2.

Total N	167
Test statistic	141.089
Degree of freedom	6
Asymptotic sig. (2-sided test)	0.000

Table A6. Pairwise comparisons for Fig A2.

Sample 1-Sample 2	Test statistic	Std. error	Std. test statistic	Sig.	Adj. sig.[a]
T2_Grit80-T2_Grit180	0.192	0.024	7.976	<0.001	0.000
T2_Grit80-T2_Grit1500	0.204	0.024	8.475	0.000	0.000
T2_Grit80-T2_Grit240	0.210	0.024	8.724	0.000	0.000
T2_Grit80-T2_Grit400	0.222	0.024	9.223	0.000	0.000
T2_Grit80-T2_Grit800	0.228	0.024	9.472	0.000	0.000
T2_Grit80-T2_Grit600	0.234	0.024	9.721	0.000	0.000
T2_Grit180-T2_Grit1500	0.012	0.024	0.499	0.618	1.000
T2_Grit180-T2_Grit240	0.018	0.024	0.748	0.455	1.000
T2_Grit180-T2_Grit400	0.030	0.024	1.246	0.213	1.000
T2_Grit180-T2_Grit800	0.036	0.024	1.496	0.135	1.000
T2_Grit180-T2_Grit600	0.042	0.024	1.745	0.081	1.000
T2_Grit1500-T2_Grit240	−0.006	0.024	−0.249	0.803	1.000
T2_Grit1500-T2_Grit400	−0.018	0.024	−0.748	0.455	1.000
T2_Grit1500-T2_Grit800	−0.024	0.024	−0.997	0.319	1.000
T2_Grit1500-T2_Grit600	−0.030	0.024	−1.246	0.213	1.000
T2_Grit240-T2_Grit400	0.012	0.024	0.499	0.618	1.000
T2_Grit240-T2_Grit800	0.018	0.024	0.748	0.455	1.000
T2_Grit240-T2_Grit600	0.024	0.024	0.997	0.319	1.000
T2_Grit400-T2_Grit800	0.006	0.024	0.249	0.803	1.000
T2_Grit400-T2_Grit600	0.012	0.024	0.499	0.618	1.000
T2_Grit800-T2_Grit600	−0.006	0.024	−0.249	0.803	1.000

Each row tests the null hypothesis that the Sample 1 and Sample 2 distributions are the same. Asymptotic significances (2-sided tests) are displayed. The significance level is 0.05.

[a]Significance values have been adjusted by the Bonferroni correction for multiple tests.

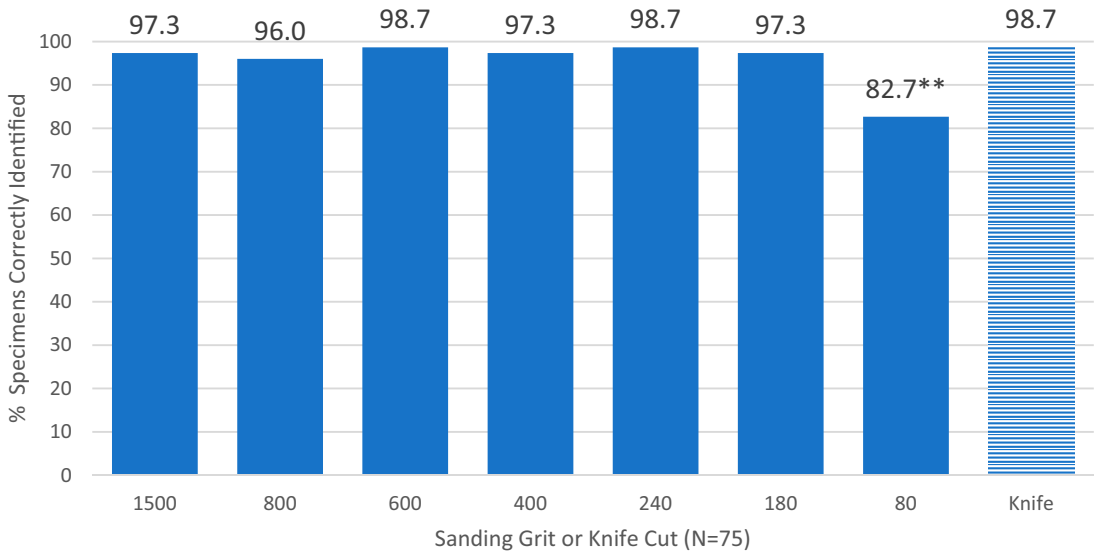## Field Model Predictive Accuracy by Test Specimen Sanding Grit or Knife Cut (Top-2)

Figure A3.   Comparison of Peru field model predictive accuracy (top-2) by sanding grit (solid bars) and knife-cut (patterned bar) groups ($N = 75$). The percentages of specimens correctly identified among all the groups were compared using Cochran's Q with post hoc multiple comparisons per Dunn (1964) with an experiment-wise error of 0.05. Multiple comparisons showed that there were no significant differences ($p > 0.05$) among the groups with the following exceptions. ** There was a statistically significant difference ($p < 0.05$) between 80 grit and all other grits, respectively.

Table A7. Cochran's Q test for Fig A3.

Total N	75
Test statistic	47.652
Degree of freedom	7
Asymptotic sig. (2-sided test)	<0.001

Table A8. Pairwise comparisons for Fig A3.

Sample 1-Sample 2	Test statistic	Std. error	Std. test statistic	Sig.	Adj. sig.[a]
T2_Grit80-T2_Grit800	0.133	0.029	4.554	<0.001	0.000
T2_Grit80-T2_Grit1500	0.147	0.029	5.010	<0.001	0.000
T2_Grit80-T2_Grit400	0.147	0.029	5.010	<0.001	0.000
T2_Grit80-T2_Grit180	0.147	0.029	5.010	<0.001	0.000
T2_Grit80-T2_Grit600	0.160	0.029	5.465	<0.001	0.000
T2_Grit80-T2_Grit240	0.160	0.029	5.465	<0.001	0.000
T2_Grit80-T2_ Knife	−0.160	0.029	−5.465	<0.001	0.000
T2_Grit800-T2_Grit1500	0.013	0.029	0.455	0.649	1.000
T2_Grit800-T2_Grit400	−0.013	0.029	−0.455	0.649	1.000
T2_Grit800-T2_Grit180	−0.013	0.029	−0.455	0.649	1.000
T2_Grit800-T2_Grit600	−0.027	0.029	−0.911	0.362	1.000
T2_Grit800-T2_Grit240	−0.027	0.029	−0.911	0.362	1.000
T2_Grit800-T2_Knife	−0.027	0.029	−0.911	0.362	1.000
T2_Grit1500-T2_Grit400	0.000	0.029	0.000	1.000	1.000
T2_Grit1500-T2_Grit180	0.000	0.029	0.000	1.000	1.000
T2_Grit1500-T2_Grit600	−0.013	0.029	−0.455	0.649	1.000
T2_Grit1500-T2_Grit240	−0.013	0.029	−0.455	0.649	1.000
T2_Grit1500-T2_Knife	−0.013	0.029	−0.455	0.649	1.000
T2_Grit400-T2_Grit600	0.013	0.029	0.455	0.649	1.000
T2_Grit180-T2_Grit600	0.013	0.029	0.455	0.649	1.000
T2_Grit400-T2_Grit180	0.000	0.029	0.000	1.000	1.000
T2_Grit400-T2_Grit240	−0.013	0.029	−0.455	0.649	1.000
T2_Grit400-T2_ Knife	−0.013	0.029	−0.455	0.649	1.000
T2_Grit180-T2_Grit240	0.013	0.029	0.455	0.649	1.000
T2_Grit180-T2_ Knife	−0.013	0.029	−0.455	0.649	1.000
T2_Grit600-T2_Grit240	0.000	0.029	0.000	1.000	1.000
T2_Grit600-T2_ Knife	0.000	0.029	0.000	1.000	1.000
T2_Grit240-T2_ Knife	0.000	0.029	0.000	1.000	1.000

Each row tests the null hypothesis that the Sample 1 and Sample 2 distributions are the same. Asymptotic significances (2-sided tests) are displayed. The significance level is 0.05.

[a]Significance values have been adjusted by the Bonferroni correction for multiple tests.
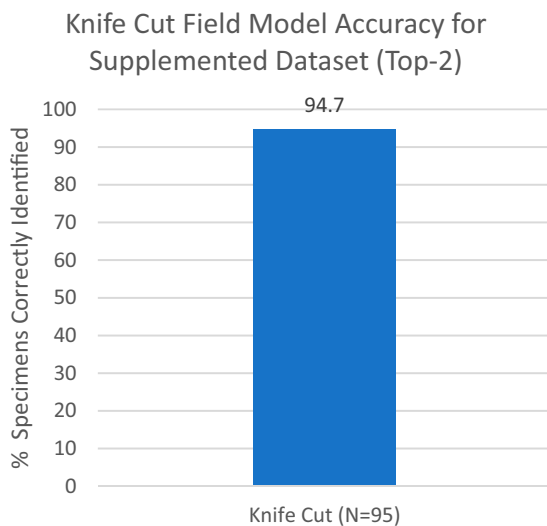

Figure A4.   Predictive accuracy for knife-cut dataset including 10 additional specimens of Poulsenia and 10 additional specimens of Schizolobium, all from the UNALM collection ($N = 95$).
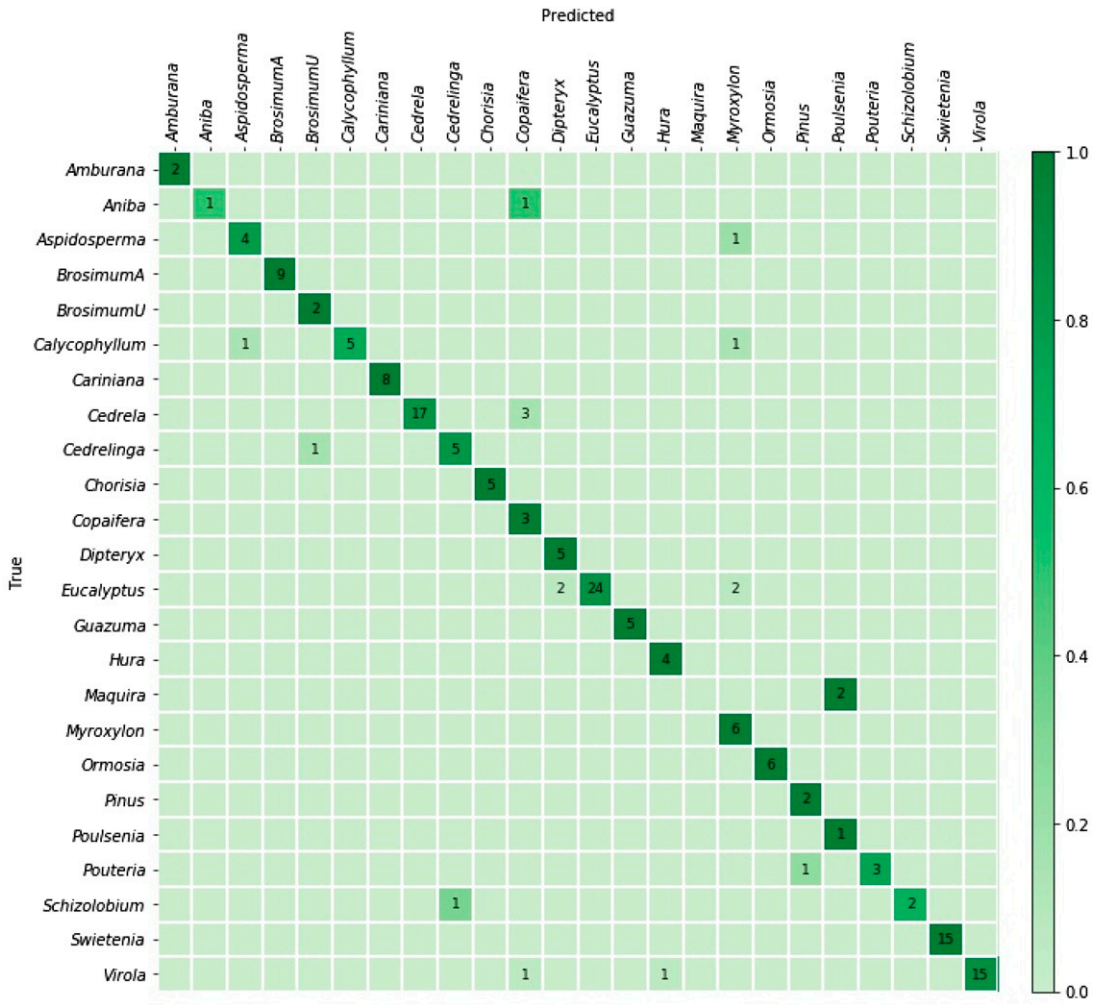
Figure A5.   Confusion matrix for ResNet50, 1500 sanding grit.
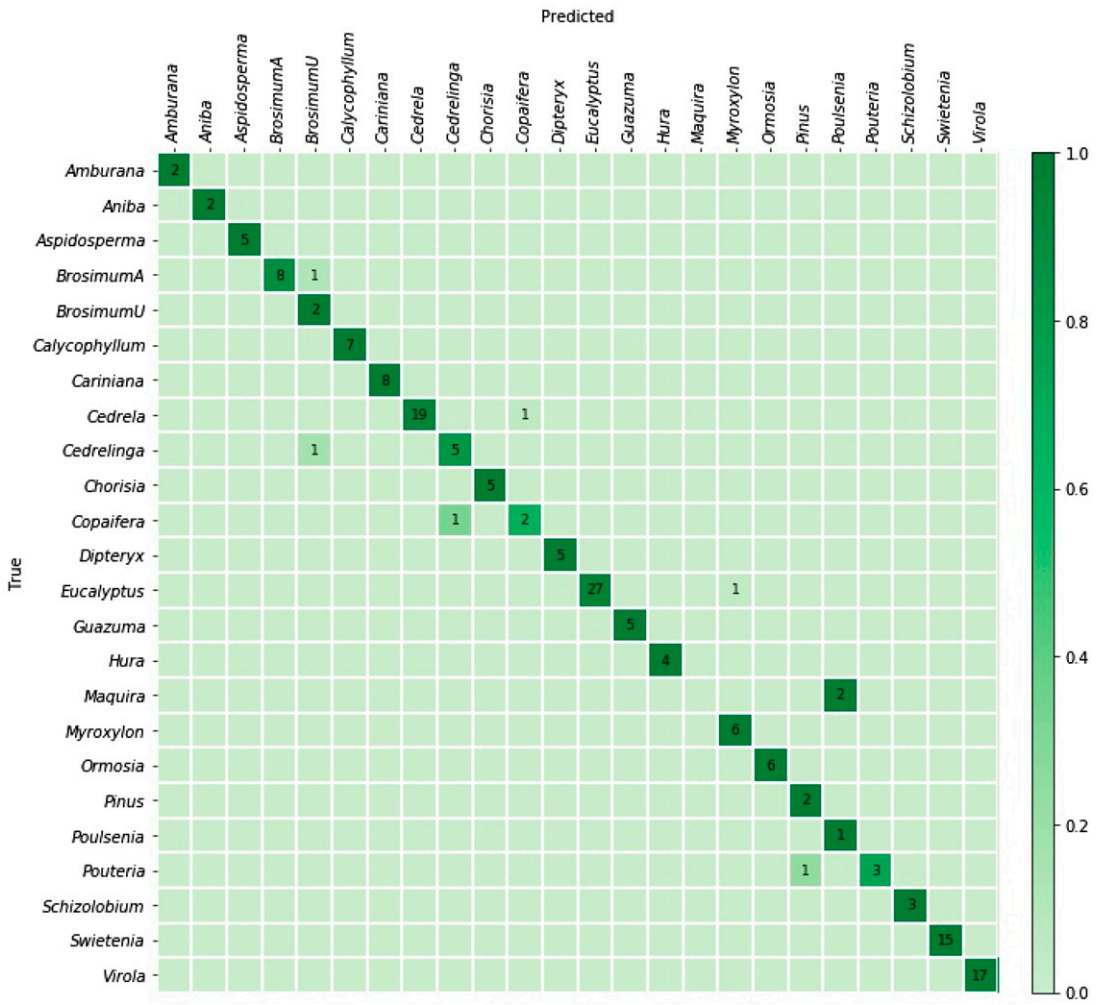
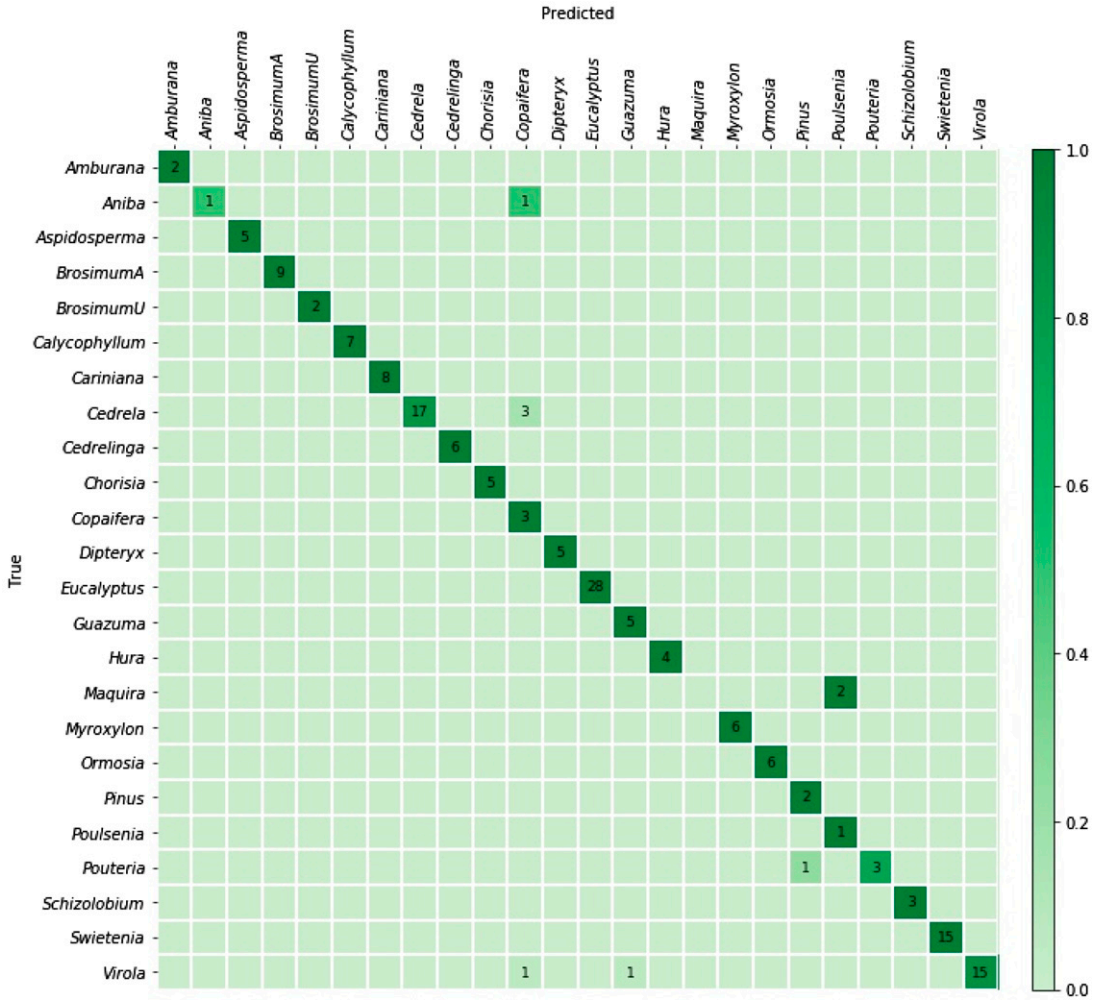Figure A6.　Confusion matrix for ResNet 50, 800 sanding grit.

Figure A7.   Confusion matrix for ResNet 50, 600 sanding grit.
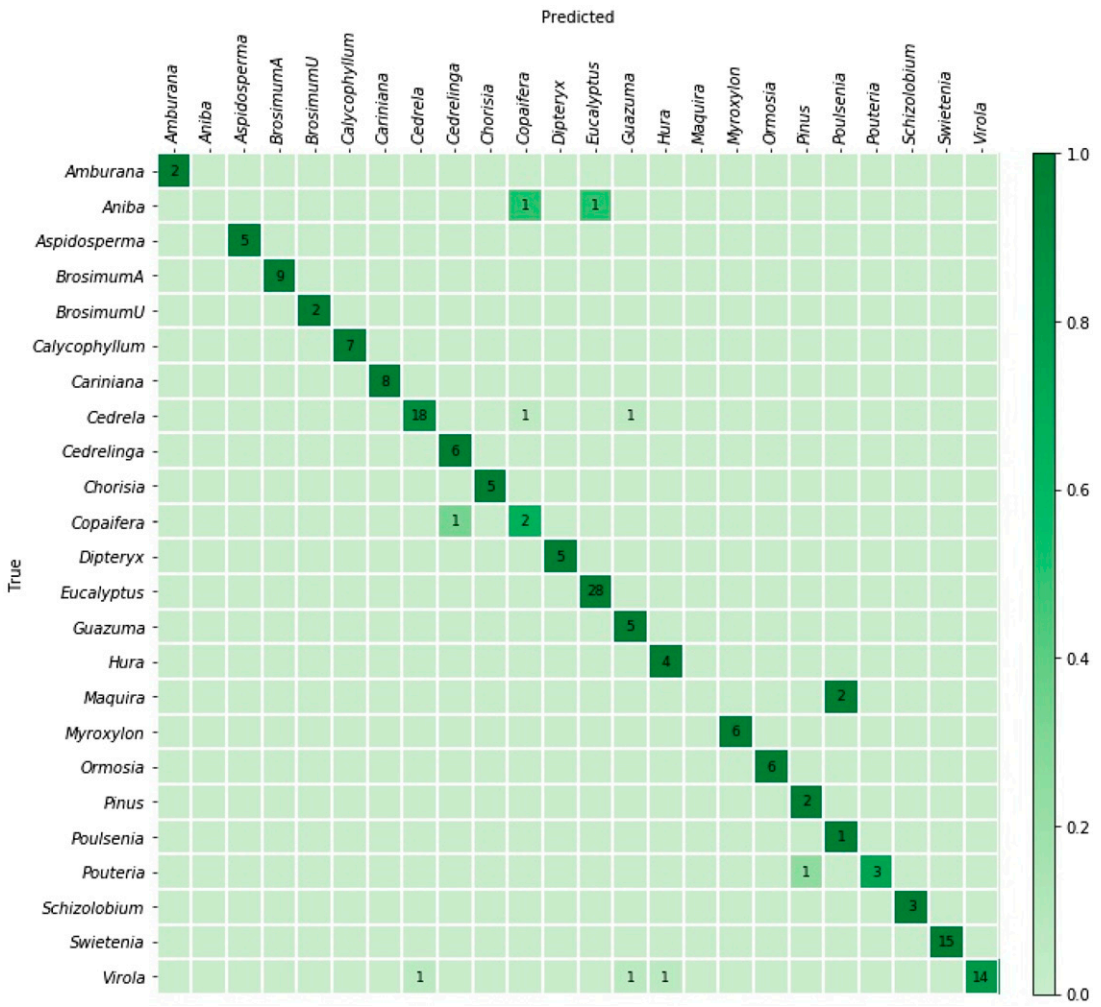
Figure A8.   Confusion matrix for ResNet 50, 400 sanding grit.
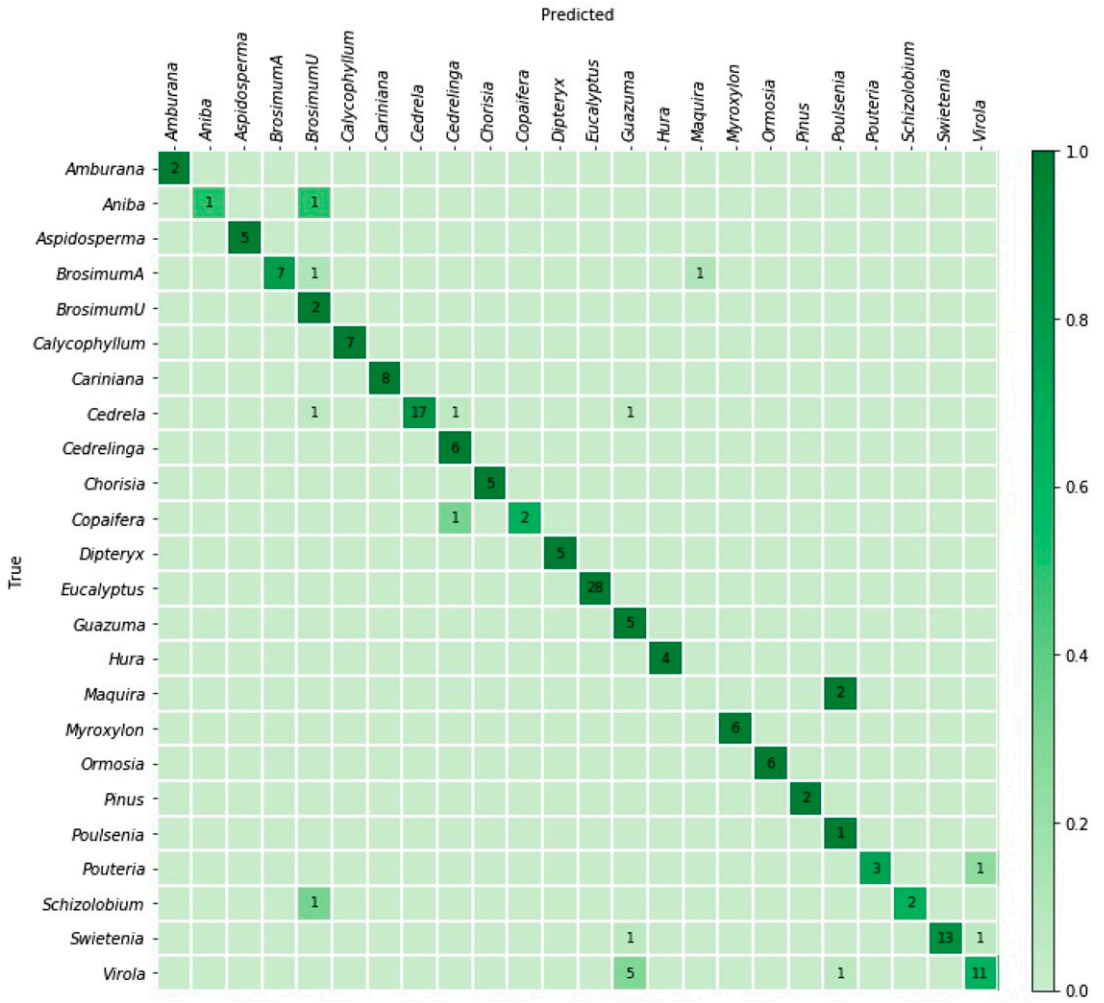
Figure A9.   Confusion matrix for ResNet 50, 240 sanding grit.
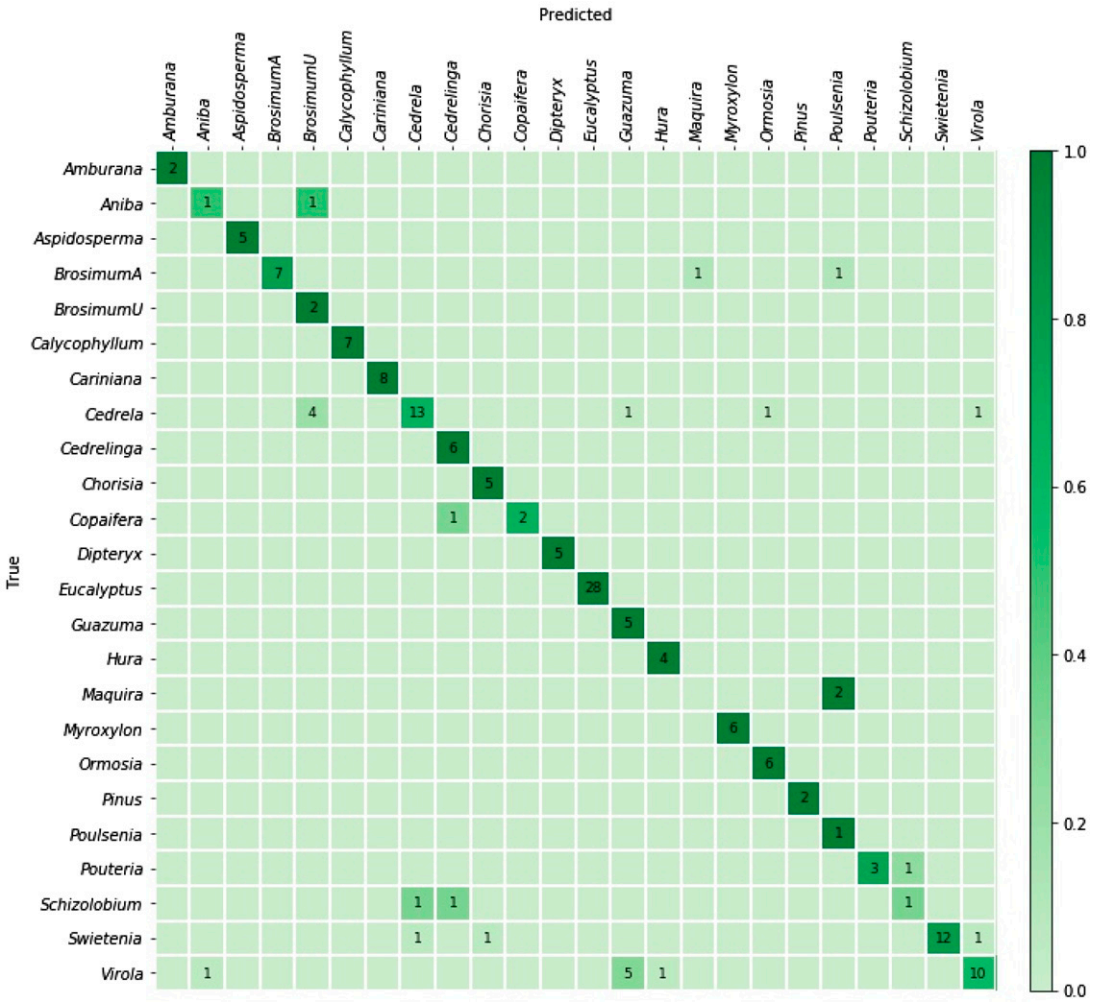
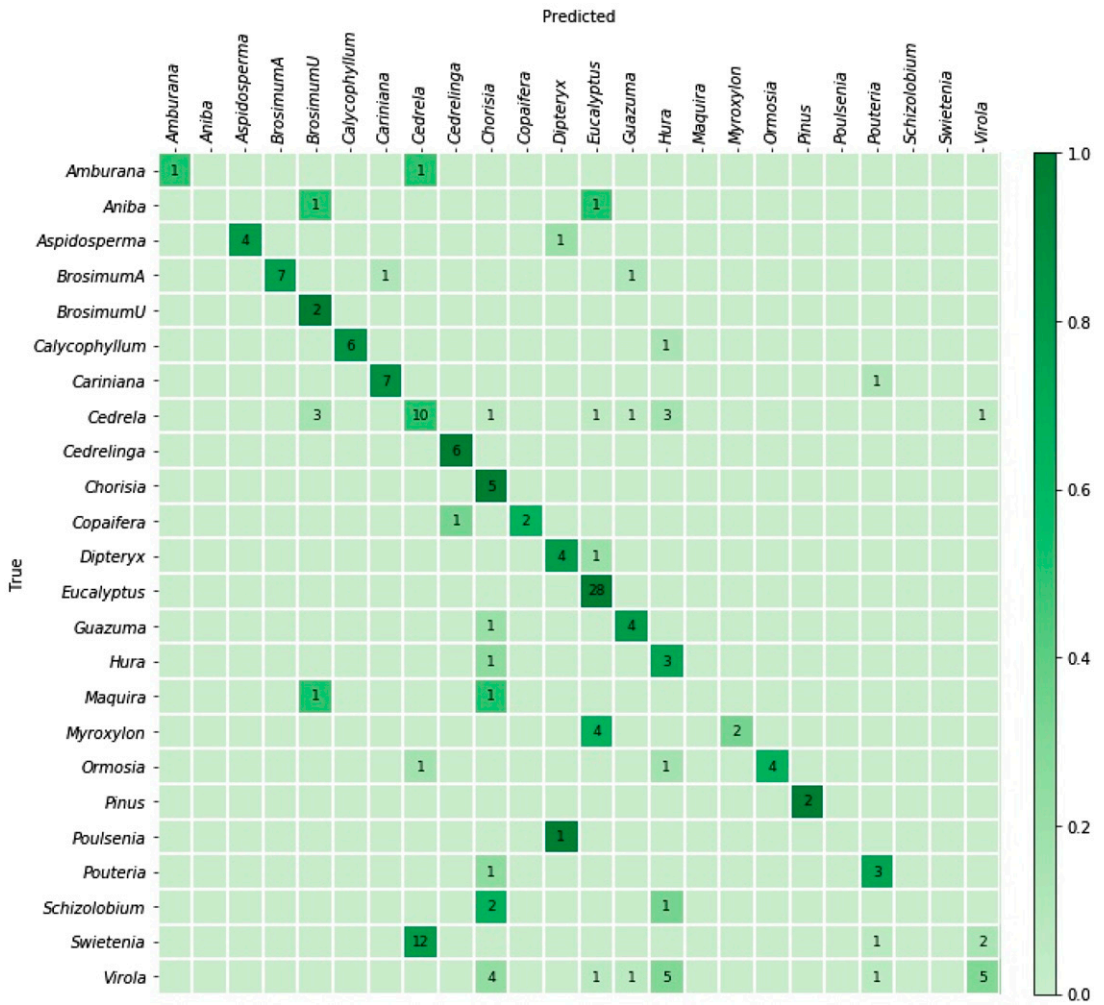Figure A10.   Confusion matrix for ResNet 50, 180 sanding grit.

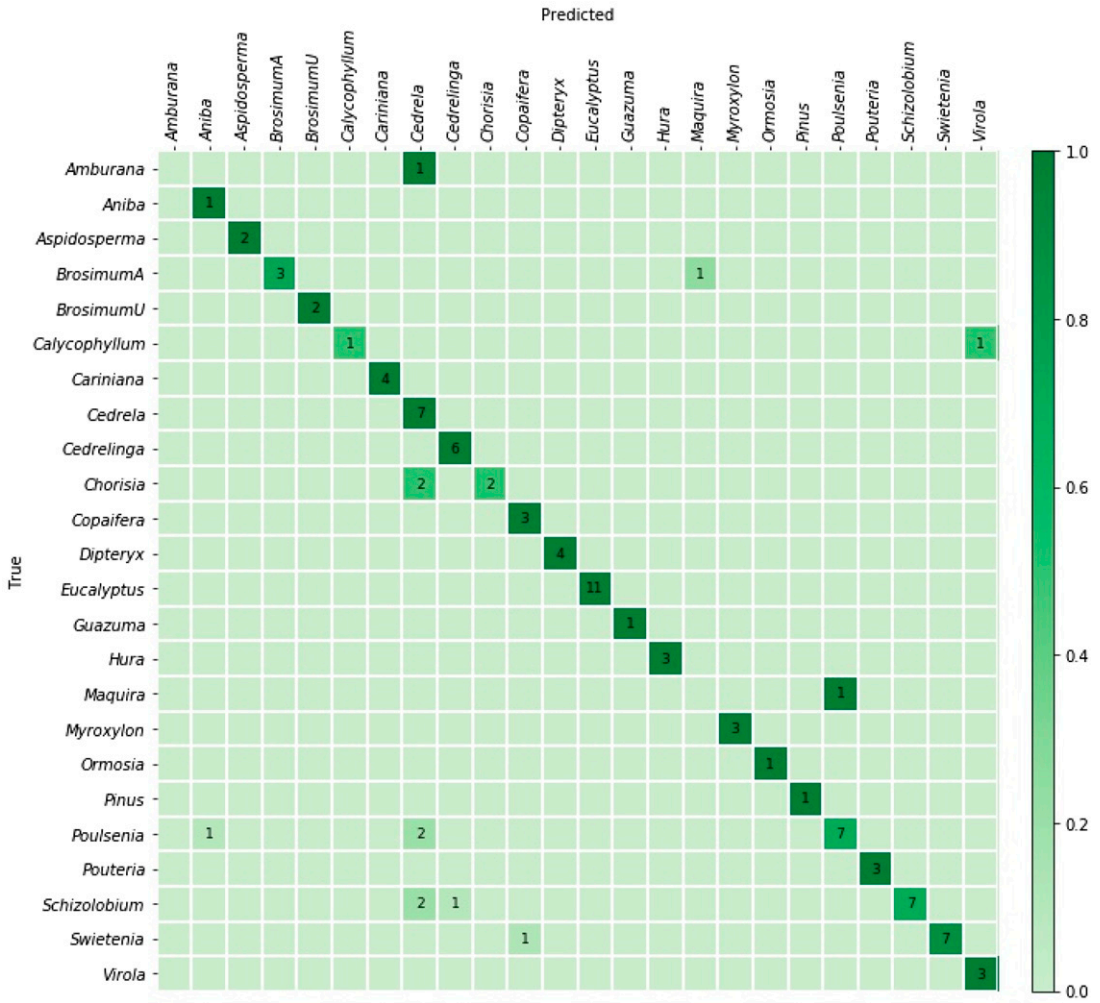Figure A11.   Confusion matrix for ResNet 50, 80 sanding grit.

Figure A12.   Confusion matrix for ResNet 50, knife cuts.

PROFESSIONAL PAGES

SUMMARY OF AWARDS PRESENTED AT 2023 SWST CONVENTION, JUNE 25-30, 2023, CROWNE PLAZA RESORT IN ASHEVILLE, NORTH CAROLINA, USA

GEORGE MARRA EXCELLENCE IN WRITING

The George Marra Award is given in memory of George Marra by the Marra Family in recognition of George's devotion to excellence in writing. Every article in each issue of the most recent volume of *Wood and Fiber Science* is read and judged by a committee. The committee for 2023 included: Chair of Committee; Duncan Mayes, Lignutech Oy (Ltd), Finland; Laurence Schimleck, OR State University, USA; Joe Loferski, VA Tech, USA.

First Place

Olsson A, Pot G, Viguier J, Hu M, Oscarsson J (2022) Performance of timber board models for prediction of local bending stiffness and strength—with application on douglas fir sawn timber. Wood Fiber Sci 54(4):226-245.

Second Place

Lipovac D, Wie S, Nyrud AQ, Burnard MD (2022) Perception and evaluation of (modified) wood by older adults from Slovenia and Norway. Wood Fiber Sci 54(1):45-59.

Third Place

Tracye M, Murphy L, Schimleck, Landers A (2022) Evaluating log stiffness using acoustic velocity for manufacturing structural oriented strand board. Wood Fiber Sci 54(2):9-110.

STUDENT POSTER COMPETITION

The purpose of the Student Poster Competition is to encourage student membership and participation in the Society of Wood Science and Technology (SWST), encourage student attendance at the SWST International Conference, recognize excellence in student research, and improve the visibility of student research efforts. A committee of four on a 100-point scale, using the following criteria, evaluated the abstracts and poster presentations:

Submitted Abstract

1. Soundness of research hypothesis (10 points)
2. Scientific writing ability (10 points)
3. Organization (10 points)

Poster Presentation

4. Scientific merit (newness, breadth of interest, and potential impact of the research) (15 points)
5. Experimental design and thoroughness of investigation (15 points)
6. Validity of conclusions (15 points)
7. Organization and visual quality of presentation (15 points)
8. Response to questions of judges (10 points)

This year's panel of student poster judges were: Chair: Henry Quesada, Purdue University, USA; Eva Haviarova, Purdue University, USA; Gloria Oporto, West Virginia University, USA; Brian Bond, Virginia Tech, USA.

Student Poster Competition Participants

Oluwafunbi Adeleye, Oregon State University, United States, "*Long-Term Response of Wood-Based Composites in Variable Climate Conditions*"

Courage Alorbu, University of Idaho, United States, "*Leachability and Biological Decay Resistance of Zinc Oxide Eugenol Organic Cement Treated Wood*"

Nelson Barrios, North Carolina State University, United States, "*Unveiling the Nanocellulose-Water Interactions Through Computational Simulations*"

Christina Bjarvin, University of Washington, United States, "*Reuse, Recycle, Incinerate, or Landfill? LCA-Based Environmental Implications of End-of-Life Scenarios for Mass Timber Buildings*"

Chih Cheng Chen, Purdue University, United States, "*The Bending Moment Capacity of the Lap and Dowel Joints Fabricated from Salvaged CLT Panels*"

Lieke Droog, University of Washington, United States, "*Global Warming Mitigating Role of Forests in Washington State, by Land Ownership Type*"

Avani Flanagan, Eastern Illinois University, United States, "*Assessing the Potential Use of a CBD Extraction Byproduct as a Wood Finishing Product*"

Yu Fu, University of North Texas, United States, "*Life Cycle Assessment of Laboratory Scale Biological Hemp Retting Process*"

Lei Han, Inno Renew CoE & University of Primorska, Slovenia, "*A Review on Adhesive and Metal-Free Assembly Techniques for Prefabricated Multi-Layer Engineered Wood Products*"

Sungjun Hwang, University of Maine, United States, "*Utilization of CNC Nanoparticles Prepared Via Ultrasonic Spray Dryer as Reinforcement for PVA-Composite Films*"

Daisuke Kanagaki, Chiba University, Japan, "*Experimental Study of Reinforcement by Self-Tapping Screws on Glulam Beams*"

Lena Maria Leiter, University of Natural Resources and Life Sciences, Vienna, Austria, "*Introducing WOOD*VERSITY*"

Dan Meyer, North Carolina University, United States, "*End-Grain Flooring from Underutilized Raw Materials: Solution to Extend and Enhance the Hardwood Resource*"

Griffin Miller, North Carolina University, United States, "*Functionalization of Cellulose for Biocomposite Compatibility: Toughening of P3HB/PLA Composites*"

Jue Mo, Purdue University, United States, "*Effect of Surface Thermal Treatment on Colors of Three Hardwood Species: Application of Artificial Neural Network*"

Liam O'Brien, University of Maine, United States, "*Hygrothermal Simulation of a Wood-Fiber Insulated Panel (WIP) Wall Assembly in Selected Climate Zones*"

Ighoyivwi Onakpoma, Oregon State University, United States, "*Wood Property Variation Within Douglas Fir Trees Grown at Different Spacing*"

Christoph Preimesberger, Wood K Plus—Kompetenzzentrum Holz GmbH, Austria, "*Auto-ignition Behavior of Wood – Impact of Size and Temperature*"

Lea Primožič, Inno Renew CoE & University of Primorska, Slovenia, "*Outreaching and Informing Society About Sustainable Construction Through Social Media*"

Andreas Tockner, University of Natural Resources and Life Sciences, Vienna, Austria, "*Individual Tree Analysis via Person-Carried Laser Scanning (PLS) in Forest Stands*"

Ting-ho Tsai, Purdue University, United States, "*Developing Potential Value-Added Product of Small-Diameter Timber in Indiana*"

Fernando Urdaneta, North Carolina University, United States, "*Hemp Hurds Alkaline Peroxide Mechanical Pulp for Hygiene Tissue Applications*"

Cody Wainscott, Oregon State University, United States, "*In-Depth Characterization of*

Bondlines in Cross-Laminated Timber Made with Preservative-Treated Lumber"

Xueqi Wang, Auburn University, United States, "*Spray-Dried Cellulose Nanocrystal Reinforced Homopolymer Polypropylene Composites*"

Lukmanul Hakim Zaini, University of Natural Resources and Life Sciences, Vienna, Austria, "*Ultra-Lightweight Foamed Insulation Panels Made of Oil Palm Trunk Fibres*"

Ke Zhan, Auburn University, United States, "*Mechanical Morphological Properties, and Crystallization Kinetics of Polypropylene/High Density Polyethylene/Microcrystalline Cellulose Composite*"

Student Poster Competition Winners

First Place: Lukmanul Hakim Zaini, University of Natural Resources and Life Sciences, Vienna, Austria, "*Ultra-Lightweight Foamed Insulation Panels Made of Oil Palm Trunk Fibres*"

Second Place: Andreas Tockner, University of Natural Resources and Life Science, Vienna, Austria, "*Individual Tree Analysis via Person-Carried Laser Scanning (PLS) in Forest Stands*"

Third Place: Cody Wainscott, Oregon State University, USA, "*In-Depth Characterization of Bondlines in Cross-Laminated Timber Made With Preservative-Treated Lumber*"

STUDENT ORAL PRESENTATIONS

In 2021, SWST began awards for student oral presentations to encourage participation and attendance at the SWST International Convention. This year's judges were: Chair: Jeff Morrell, University of the Sunshine Coast, Australia; and Sue Anagnost, State University of New York College of Environmental Science and Forestry (SUNY ESF), USA.

For 2023, the winners are:

First Place: Andreas Tockner, University of Natural Resources and Life Sciences, Vienna, Austria, "*Individual Tree Analysis via Person-Carried Laser Scanning (PLS) in Forest Stands*"
Second Place: Fernando Urdaneta, North Carolina State University, United States, "*Hemp Hurds Alkaline Peroxide Mechanical Pulp for Hygiene Tissue Applications*"
Third Place: Minami Suzuki, Chiba University, Japan, "*Study on Load-Bearing Capacity and Failure Modes of Tensile-Bolted Joints in Timber Structures*"

Distinguished Service Award

The SWST Distinguished Service Award is given in recognition of distinguished service to the profession as a whole and for extraordinary contributions to wood science and technology. Such service may have been made in any educational, technological, scientific, or professional area directly related to the profession of Wood Science and Technology in furtherance of the objectives of the Society as outlined in its Constitution and Bylaws. Guidelines for the award can be found at http://www.swst.org/wp/awards/award-distinguished-service-profession-wood-science-technology/. The 2023 winner is Susan Anagnost, a professor at the State University of New York College of Environmental Science and Forestry (SUNY ESF).

Susan Anagnost's comments on the award are as follows:

I am honored to receive the 2023 SWST Distinguished Service Award recognizing distinguished service to the profession of wood science and technology. My career in wood science began and continues at SUNY Environmental Science and Forestry in Syracuse, NY. With an undergraduate degree from Gettysburg College, I entered graduate school at ESF to study wood anatomy and expanded into wood decay and mycology with a heavy emphasis on using microscopy techniques to identify and evaluate wood anatomical features and wood decay conditions. After receiving both master's and doctoral degrees I spent several years as a PostDoctoral Associate in the Department of

Environmental Biology studying wood decay and mycology. After this I was a Research Associate for about 8 yr, and was appointed Assistant Professor in 2001, then Associate Professor in 2003, and Full Professor in 2013. I served as Department Chair of the Construction Management and Wood Products Engineering Department from 2006-2015, and as Director of the NC Brown Center for Ultrastructure Studies since 2012. I'm currently Professor Emeritus and was rehired part-time as Director of the Tropical Timber Information Center with the immediate tasks of digitizing the HP Brown Memorial Wood Collection, and identifying wood samples for engineers, architects, and wood products industries. As part of the Wood Products Engineering program at SUNY-ESF.

I taught courses in Decay of Wood Products, Microtechnique, Wood Anatomy and Identification, as well as Light Microscopy, Scanning Electron Microscopy and Transmission Electron Microscopy. Early in my career, my research involved decay detection and evaluation in utility poles and other wood products, developing methods for inspection of utility poles for decay, describing the anatomical features of soft rot, brown rot, and white rot, and identifying the fungi that caused decay. The study of soft rot cavities led to developing a method to measure microfibril angle using soft rot cavities. Later, the decay detection methods of collecting and identifying fungi were applied to an EPA project characterizing indoor air quality in homes in Syracuse. Because of this project, I was appointed to the New York State Governor's Task Force on Mold from November 2007 to April 2012. For many years I have used microscopy methods to perform quality assessment of wood products, paper-based products, coatings, and other materials for manufacturers and engineers. I have identified wood and fibers for industry, engineers, and architects. In 2001 I was honored to receive the George Marra Award for Excellence in Research and Writing. As for service to the profession, my involvement with SWST began with the Membership Committee, first as a member, then as Vice Chair, and Chair. I was elected to the SWST Executive Board 2006-2008, then elected Vice President for the 4-yr term 2008-2011 and served as President from 2010-2011. In 2017 I was awarded the rank of SWST Fellow. Most recently, I was on the Editorial Board for Wood and

Fiber Science from 2017-2022. Looking back, I appreciate how SWST provides members with the means to advance in the profession, and I encourage those in the early stage of their career to publish in Wood and Fiber Science, to get involved as a committee member, and participate in the annual meetings. My involvement in SWST was a highlight of my career. Having the opportunity to be on the executive board during the period of expansion of our membership worldwide was exciting and I believe has enhanced the role of SWST in promoting the profession. Many thanks to Vicki Herian, all Past Presidents, board members, and W&FS Editor.

Fellow Award

The Fellow Award recognizes significant contributions to the wood science and technology profession and service to the Society by SWST members. Guidelines and past recipients can be found at http://www.swst.org/wp/awards/swst-fellow-award/.

The **Fellow Award** was presented to Professor **Sudipta Dasmohapatra** from Georgetown University, USA in recognition of her service on numerous SWST committees as well as her roles on the Executive Committee and finally as President. We appreciate her service to the Society.

Distinguished Educator Award

The SWST Distinguished Educator Award is intended to recognize individual faculty and instructors at a university for sustained excellence in teaching or Extension/Outreach programming. Teaching Recognition: The distinguished educator award recognizes sustained excellence in teaching that incites intellectual curiosity in students, inspires colleagues, and makes students aware of significant relationships between academia and the world. This award was not given out in 2023.

Reviewer of the Year Award

In 2019, the SWST Executive Board instituted a Reviewer of the Year Award for Wood and Fiber Science. An honorarium of $300 was awarded to the Reviewer of the Year. This year's award goes

to Xiping Wang from the USDA Forest Products Laboratory, USA.

The following criteria were used to judge the Reviewer of the Year Award, which was announced at the annual SWST Meeting:

1. The number of papers reviewed in the previous year.
2. The quality of the review as judged by the editors.

3. Nomination by an author.

All reviewers are ranked according to these criteria and the highest number of points is deemed the Reviewer of the Year.

Past Editor of Wood and Fiber Science was recognized with an Award—Susan LeVan-Green retired from dedicated service as being editor of *Wood and Fiber Science* from 2017 to 2022.

EDITORIAL

I am honored to write this final letter as I retire from being your Executive Director of the *Society of Wood Science and Technology*. It has been a wonderful ride these past 46 years.

Two years ago, I was chosen to be one of the "SWST Woman Ambassadors Creating the Future of Wood Science." However, I don't have the same background as the rest of the Women Ambassadors. I don't have a BS, MS, or PhD. When I graduated high school, even though I was 3rd in my class, I was counseled that my best career option would be as a secretary because I had good organizational skills, math skills, and secretarial ability. I didn't have the confidence in myself at that time to do something different. So that's what I did, first for an insurance company in Madison, WI, then at a US Army medical pharmacy in Fort Jackson, SC, next at a nuclear missile base as the colonel's secretary in Neu Ulm Germany, and finally back to Madison at the Forest Products Laboratory (FPL) where I retired in 2011. I began as a secretary but was fortunate enough to have a supervisor with good insight to establish an upward mobility position as a statistical assistant. I was able to get training and education in this field and earned a 2-yr associate degree in science from our local technical college and university to reach the research statistician level.

In 1976, William Lehmann was the Society's Executive Secretary (this had always been a scientist or engineer from FPL since the Society began in 1958). He was also my supervisor at FPL. He asked me to help him with his Society position and said I would love it and be challenged by it. Thus, began my journey with SWST. I was the Assistant to William Lehman, followed by William Simpson, and finally J. T. Quirk. In 1984, Dr. Quirk said I was doing all the work anyway so I should just become the Executive Secretary. It was a challenge to get the SWST Board of Directors to agree to this because, since 1958 when the organization was formed, the Executive Secretary had ALWAYS been a MALE research scientist at FPL. However, it did happen and I have been the Executive Director since.

I remember the first meeting I attended. It was held in the Brown Palace Hotel in Denver, CO, in June 1977. I was in awe, as I saw the opulence of the hotel, the crystal chandeliers, the beautiful furnishings. It was the most extravagant hotel I had been in, and I was there to WORK and meet this amazing group of professional wood science people who were world-renowned and experts in their fields. I was overwhelmed as a very young 25-yr-old, unexperienced, timid, and naïve woman.

But time goes by quickly and now I stand before you, not as that 25-yr-old, but as a much older, more experienced, confident, and determined woman. And you, professional world-renowned scientists, are still here and I am enlightened and educated at each meeting and with each interaction I have with any of you.

I was especially appreciative to be present at the 2023 International Convention in June in Asheville, NC, with 19 past presidents who came to share this last event with me, to offer their support and friendship, and to let me know they appreciated my time with them. I also had correspondence and phone calls with several other past presidents who couldn't make it to the meeting but wanted to be sure they could pass on their good wishes.

Each past president didn't just give 1 yr of their time to the Society, but 4 years on the Board, in addition to numerous committee assignments. I was able to spend this time with them, helping them travel through the many rules and procedures that make up a professional Society. It was a challenge at times, but always rewarding and fulfilling.

Working for SWST enabled me to grow as a person and gave me the gift of self-confidence. During the time I've been Executive Director, I have run the day-to-day operations of the Society, answering emails, taking phone calls, taking care

of financials, writing reports, developing and maintaining the organization's website, working with many board members and committee members, and organizing board meetings, as well as meetings of the Society as a whole.

With my background at FPL as a Statistician, I was involved in many different fields of research, so I knew a little about each of them and this helped with my handling of inquiries about a myriad of wood-related issues. The best, and sometimes most challenging part, has been organizing international meetings. I've learned a great deal about organizing conferences and everything associated with conference planning particularly holding meetings in several countries around the world. I have enjoyed thoroughly the considerable travel associated with these meetings as well as the opportunity to meet and work with so many different people over the years and in many countries.

I believe that people in the wood field are wonderful. They care about other people and truly about our earth and want to make a difference in the world. I have been so lucky to have met and worked with a multitude of talented and dedicated people over the years on the Executive Boards and Committees.

What you choose to do is important and can change the world. I would like to challenge you to continue to support your professional society, SWST, and become involved. You can do this by writing papers and publishing in our two journals, *BioProducts Business* and *Wood and Fiber Science*. They are known around the world as high-level research journals. You can also attend conventions that are held once a year where you can present your research and learn from others about research that is going on either in your field or in something totally different that you might find interesting. It's a time to network and meet these great people. You can also volunteer on committees, run for office for SWST, and help shape the future. Just remember—YOU CAN MAKE A DIFFERENCE.

It was difficult for me to say goodbye and turn over the Executive Director's position, but I look forward to new challenges and opportunities in other paths. I ask that you offer your new Executive Director, Angela Haney, the same respect and assistance that you have given me over the years.

I will never say "Goodbye," but instead "Au Revoir" (until we meet again). I send out my love and best wishes to all of you! Thank you for all you have done for me.

Sincerely,

VICTORIA HERIAN
vicki@swst.org